Simulation of Laser Additive Manufacturing and its Applications

DISSERTATION

Presented in Partial Fulfillment of the Requirements for the Degree Doctor of Philosophy
in the Graduate School of The Ohio State University

By

Yousub Lee

Graduate Program in Welding Engineering

The Ohio State University

2015

Dissertation Committee:

Professor Dave F. Farson, Advisor

Professor Wei Zhang, Advisor

Professor Antonio J. Ramirez

Abstract

Laser and metal powder based additive manufacturing (AM), a key category of advanced Direct Digital Manufacturing (DDM), produces metallic components directly from a digital representation of the part such as a CAD file. It is well suited for the production of high-value, customizable components with complex geometry and the repair of damaged components.

Currently, the main challenges for laser and metal powder based AM include the formation of defects (e.g., porosity), low surface finish quality, and spatially non-uniform properties of material. Such challenges stem largely from the limited knowledge of complex physical processes in AM especially the molten pool physics such as melting, molten metal flow, heat conduction, vaporization of alloying elements, and solidification. Direct experimental measurement of melt pool phenomena is highly difficult since the process is localized (on the order of 0.1 mm to 1 mm melt pool size) and transient (on the order of 1 m/s scanning speed). Furthermore, current optical and infrared cameras are limited to observe the melt pool surface. As a result, fluid flows in the melt pool, melt pool shape and formation of sub-surface defects are difficult to be visualized by experiment. On the other hand, numerical simulation, based on rigorous solution of mass,

momentum and energy transport equations, can provide important quantitative knowledge of complex transport phenomena taking place in AM.

The overarching goal of this dissertation research is to develop an analytical foundation for fundamental understanding of heat transfer, molten metal flow and free surface evolution. Two key types of laser AM processes are studied: a) powder injection, commonly used for repairing of turbine blades, and b) powder bed, commonly used for manufacturing of new parts with complex geometry.

In the powder injection simulation, fluid convection, temperature gradient (G), solidification rate (R) and melt pool shape are calculated using a heat transfer and fluid flow model, which solves the mass, momentum and energy transport equations using the volume of fluid (VOF) method. These results provide quantitative understanding of underlying mechanisms of solidification morphology, solidification scale and deposit side bulging. In particular, it is shown that convective mixing alters solidification conditions (G and R), cooling trend and resultant size of primary dendrite arm spacing. Melt pool convexity in multiple layer LAM is associated not only with the convex shape of prior deposit but also with Marangoni flow. Lastly, it is shown that the lateral width of bulge is possibly controlled by the type of surface tension gradient.

It is noted that laser beam spot size in the powder injection AM is about 2 mm and it melts hundreds of powder particles. Hence, the injection of individual particles is approximated by a lumped mass flux into the molten pool. On the other hand, for laser powder bed AM, the laser beam spot size is about 100 μm and thus it only melts a few

tens of particles. Therefore, resolution of individual powder particles is essential for the accurate simulation of laser powder bed AM.

To obtain the powder packing information in the powder bed, dynamic discrete element simulation (DEM) is used. It considers particle-particle interactions during packing to provide the quantitative structural powder bed properties such as particle arrangement, size and packing density, which is then an inputted as initial geometry for heat transfer and fluid flow simulation. This coupled 3D transient transport model provides a high spatial resolution while requiring less demanding computation. The results show that negatively skewed particle size distribution, faster scanning speed, low power and low packing density worsen the surface finish quality and promote the formation of balling defects.

Taken together, both powder injection and powder bed models have resulted in an improved quantitative understanding of heat transfer, molten metal flow and free surface evolution. Furthermore, the analytical foundation that is developed in this dissertation provides the temperature history in AM, a prerequisite for predicting the solid-state phase transformation kinetics, residual stresses and distortion using other models. Moreover, it can be integrated with experimental monitoring and sensing tools to provide the capability of controlling melt pool shape, solidification microstructure, defect formation and surface finish.

Dedicated to my parents and wife

Acknowledgments

I would like to greatly appreciate my advisor, Prof. Dave Farson for his guidance, valuable advice and support throughout my PhD studies at The Ohio State University. As a professor, Dr. Farson is one of the distinctive researchers in the welding engineering and laser materials processing. He is actively serving technical societies as President, Board Member and other offices for Laser Institute of America. As my advisor, he has pleasantly helped me all the time with big patience to correct my scientific mistakes.

I must thank to my co-advisor, Prof. Wei Zhang for his smart advices, encouragement and support for the last year of my PhD study. Before he came to OSU as a professor, he was a distinctive researcher at Oak Ridge National Laboratory (ORNL) and Edison Welding Institute (EWI). He is now a core faculty for Simulation Innovation and Modeling Center (SIMCenter). Being his student, I have learned critical thinking and writing making me an independent researcher. Moreover, I realize that he is always ready to help his students to achieve academic and career goals.

Also, I truly thank Prof. Suresh Babu at University of Tennessee, Knoxville for his enthusiastic comments and help during my graduate school. I would like to thank Prof. Antonio Ramirez being a committee member and his critical comments on my dissertation.

I would like to acknowledge Rolls Royce, CIMJSEA center (Now, Ma^{2}JIC) and Office of Naval Research for the financial support. I appreciate Dr. J.S. Bader and M. Nordin (Rolls Royce), Prof. John Lippold (CIMJSEA) and Dr. Richard W. Fonda (ORN). Thanks to all my colleagues and professors in WE and MSE for all helps.

Last but not least, thanks to my parents and younger sister for their unbelievable support and love. Special thanks to my wife, Jinmo. I will always remember your endless patience and love.

Vita

1979..Born-Daegu, South Korea

2007..B.S. Materials Science and Metallurgical Engineering, Kyungpook National University

2009..M.S. Materials Science and Engineering, Seoul National University

2011 to present ....Graduate Research Associate, Welding Engineering, The Ohio State University

Publications

1. **Lee YS**, Nordin M, Babu SS, Farson DF (2014) Influence of fluid convection on weld pool formation in laser cladding. Welding Journal 93(8):292S-300S.

2. **Lee Y**, Nordin M, Babu SS, Farson DF (2014) Effect of Fluid Convection on Dendrite Arm Spacing in Laser Deposition. Metallurgical and Materials Transactions B 45(4): 1520-1529.

3. **Lee YS** and Zhang W Mesoscopic (2015) Simulation of Heat Transfer and Fluid Flow in Laser Powder Bed Fusion Additive Manufacturing. In Proceeding of Solid Freeform Fabrication Symposium, Austin, Texas

Fields of Study

Major Field: Welding Engineering

Table of Contents

List of Tables

List of Figures

Chapter 1: Introduction

Laser and metal powder based additive manufacturing (AM) is an innovative technology since it offers almost limitless freedom of design over constraints of conventional subtractive manufacturing processes [1]. Moreover, AM provides minimal or non-post machining feature so that reduces overall cost in exclusive parts in aerospace or biomedical industries [2]. Despite the benefit in design and cost, metal based AM is in a relatively initial stage of development due to a limited understanding of complex physical processes such as laser-material interactions, heat transfer and molten metal flow, phase transformations and thermal stresses and distortion; all these factors influence the final build quality and material properties [2, 3]. However, quantitative experimental measurement is highly difficult due to the localized and transient nature of AM process. Therefore, 3D heat transfer and fluid flow simulation and powder packing simulation are conducted to provide fundamental understanding of AM processes in this dissertation.

In general, metallic additive manufacturing system can be divided into three main categories by the terms of heat source and material input types: a) powder injection, b) powder bed c) wire feed system [3]. However, the wire feed system uses wire as a material input and thus it is out of the scope for this dissertation. Therefore, only powder injection and powder bed systems will be dealt in this dissertation. The schematic of the two types of laser AM is illustrated in Figure 1.1 below.

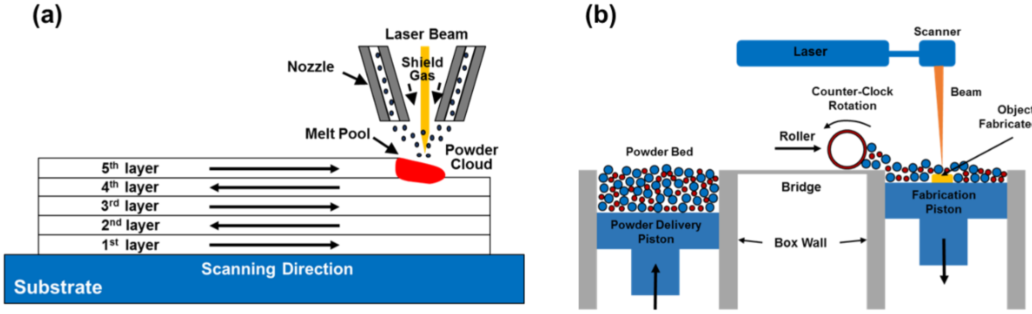

Figure 1.1 Schematic of two types of laser additive manufacturing (LAM) (a) powder injection system (b) powder bed system

For the powder injection system in Figure 1.1(a), the metal particles are delivered through multiple powder feed nozzles placed annularly around the laser beam, into the laser generated melt pool. The laser beam melts both the powder particles and previously deposited layer to form a melt pool. The flight of the particles creates powder cloud between the feed nozzle and deposit layer. The laser beam interacts with particles in the cloud and the laser power is attenuated by absorption, reflection and radiation due to the laser-powder interaction.

For the powder bed system in Figure 1.1(b), the powder particles are carried by counter-rotating roller (or rake) from the powder reservoir in delivery area and creates powder bed in fabrication area. During the process, a laser beam scans over a selected region of the pre-deposited powder bed and melts powder particles, which eventually coalesce into the molten pool. Consequently, a thin molten track is developed and form a thin layer of the final part. After completion of the layer build, the fabrication platform is lowered its height by one layer thickness following by delivering additional powder particles from the powder reservoir and spreading by the roller. These processes are repeated until the designed geometry of part is made.

The benefits of powder injection system is in its ability to create relatively large build in size and to repair worn or damaged parts [3]. For instance, Ni based superalloy used in turbine engine is high in price. Thus, repair instead of replacing has been strongly required from aerospace industry. Additional potential advantage is to increase a degree of freedom on working direction in which the powder nozzle can be tilted up to 180 degree [4]. Also, this system allows the variety selection of metals [5] and a creation of graded structures through deposition of highly mixed metals [6]. By comparison to the system above, powder bed system can produce high precision part in relatively better dimensional control [3]. Thus, more complex geometry parts can be generated via this system. As seen above, each AM system has its own characteristic features and thus a right selection of the process is required for various purpose of parts.

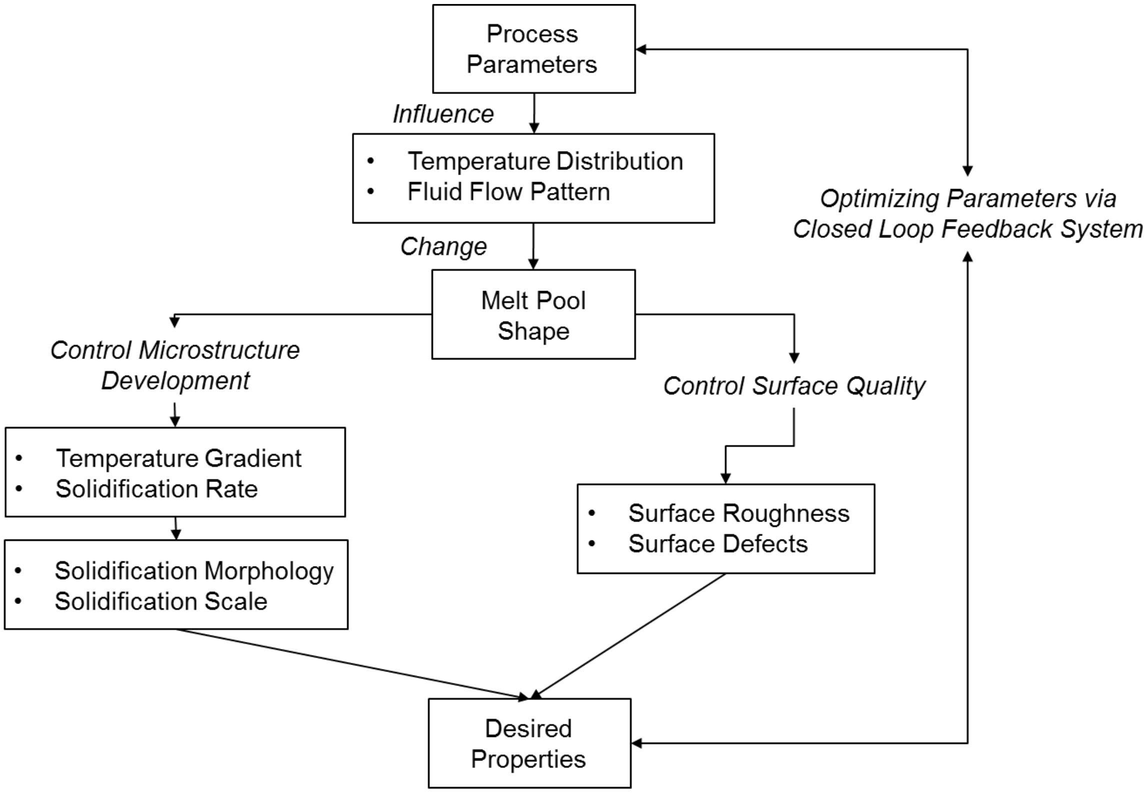

Figure 1.2 Research objectives of this dissertation

Overarching goal of this dissertation is to develop a methodological basis for closed loop feedback system that can control melt pool shape, solidification microstructure, defect formation and surface quality in real time. It should be accomplished based on a deep understanding of relationship between the process parameters, melt pool shape and resultant microstructure and surface quality.

Research objectives are summarized in schematic plot in Figure 1.2. The process parameters influence temperature distribution and fluid flow pattern in the melt pool and consequently melt pool shape changes. Thus, accurate prediction of melt pool shape is essentially required. Since temperature gradient (G) and solidification rate (R) are dependent on melt pool shape and the solidification morphology and scale can be determined by combination of G and R, the study of relationship between process parameters, fluid characteristics and solidification microstructure is further required. Also, surface finish quality such as roughness and balling defects is associated with melt pool characteristics. Therefore, the study of molten pool physics is essential to minimize surface roughness and defects. By completing the research works, one will acquire quantitative understanding of the relationship between heat transfers, fluid convection, melt pool shape, structural powder bed property, surface roughness and defects formation. The detailed objectives and results are summarized in each following chapters.

In chapter 2, 3D transient transport simulation was used to study the underlying fundamentals of the AM process with powder injection. The physical phenomena addressed include: laser-powder-substrate interaction, melt pool formation, fluid convection and solidification in IN718 laser single layer, single track deposit. The results showed that impingement of opposing fluid flows caused by transition of surface tension gradient from positive to negative promotes deeper penetration of the weld pool. The temperature gradient G and solidification rate R were used to predict the solidification morphology of columnar dendrite.

In chapter 3, the effect of fluid convection on primary dendrite arm spacing (PDAS) was investigated with the obtained G and R values at the weld pool solidification boundary. These were obtained from the 3D numerical simulation of the single layer laser deposition process. The obtained G and R values were used to investigate the relationships between PDAS and solidification conditions (G and R) using theoretical models of Kurz-Fisher and Trivedi. The simulation results showed that the convective mixing in the weld pool alters solidification conditions so as to retarded cooling. It also noted that the PDAS values predicted by Trivedi model are closer to the measured values.

In chapter 4, the 3D numerical simulation of transport phenomena was extended to multiple-layer, single track laser additive manufacturing (LAM). It predicts the peak temperature, fluid flow velocity distribution, remelting and transient variation of the weld pool fluid boundary shape and solidified build geometry during deposition of successive LAM layers. The analysis showed that the hemispherical melt pool free surface in LAM causes the mechanisms that determine melt pool fusion boundary shapes to be different from melt pools formed on a flat surface. It also studied correlations between dimensionless process/material parameters (Pe, *Pr* and Ma), melt fluid flow patterns and melt pool fusion boundary shape. The results showed that the Marangoni-driven fluid penetration into the solid substrate at the outward edges becomes deeper and consequently the more pronounced convex shape is promoted at the pool bottom.

In chapter 5, the effect of melt pool fluid flow patterns on the surface finish and dimensional accuracy was investigated in multiple-layer LAM. Three distinct melt pool fluid flow patterns driven by three different types of thermocapillary gradients (positive, negative and mixed) were used. The results showed that a similar mushroom-shape bulge was produced at the lateral edge of the start of deposits made with material having positive and negative gradients in spite of significantly different fluid flow patterns that form the bulge. Also, the simulation results showed that non-uniformity and surface finish of the deposit sidewall can be optimized by manipulation of the thermocapillary gradient. The results showed that the bulge at the start of the build was reduced by melt pool having mixed thermocapillary gradient. The lateral width of the bulge was approximately 56% less than that of the bulge width of a deposit having the negative gradient.

In chapter 6, the advanced discrete element method (DEM) is used for laser-powder bed fusion (L-PBF) additive manufacturing to provide the underlying fundamentals of the structural packing properties for real particles, which is important information for 3D heat transfer and fluid flow simulation since the packing structure is the starting point of the geometry setting. The results showed that the powder varies little in equal size and uniform Gaussian distributions. However, asymmetric distribution with negatively skewed, positively skewed and Gaussian like distribution contribute to increase the packing density. The role of fine particles is quantitatively investigated with the ratio of D_{90}/D_{10}. The investigation reveals that the ratio of D_{90}/D_{10} can be a good indicator to predict the packing density variation.

Last but not least, in chapter 7, 3D transient heat transfer and fluid flow simulation based on the DEM simulation is performed to study the effect of powder size distribution, laser power and scanning speed on the bead geometry and formation of balling defects during L-PBF additive manufacturing process. The results showed that the balling defects were worsened at high scanning speed, lower laser powder and lower packing density. It also showed that the defects could be minimized by manipulation of powder packing structure.

References

1. Zhou JH, Zhang YW, Chen JK (2009) Numerical simulation of random packing of spherical particles for powder-based additive manufacturing. Journal of Manufacturing Science and Engineering: ASME 131(3):031004.

2. Harris ID, Director A (2011) Development and implementation of metals additive manufacturing. In DOT International, New Orleans.

3. Frazier WE (2014) Metal additive manufacturing: A review. Journal of Materials Engineering and Performance 23(6):1917-1928.

4. Weisheit A, Gasser A, Backes G, Jambor T, Pirch N, Wissenbach K (2013) Direct laser cladding , current status and future scope of application. In: Majumdar JD, Manna I (eds) Laser-assisted fabrication of materials, vol 161. Springer series in materials science. Springer Berlin Heidelberg, pp 221-240

5. Wong KV, Hernandez A (2012) A review of additive manufacturing. ISRN Mechanical Engineering 2012:208760.

6. Mazumder J, Schifferer A, Choi J (1999) Direct materials deposition: Designed macro and microstructure. Materials Research Innovations 3(3):118-131.

Chapter 2: Influence of Fluid Convection on Weld Pool Formation in Laser Cladding

2.1 Introduction

Laser cladding has been widely used to add protective coatings to metallic surfaces to resist corrosion or wear and to rebuild worn surfaces of structural parts [1]. These materials can be deposited as powder or wire which is fed directly into the laser-generated melt pool [2]. In laser cladding with powder, the particles are usually injected into an inert carrier gas which flows through multiple powder feed nozzles spaced annularly around the laser beam as sketched in Figure 2.1. The laser beam energy heats and melts some of the particles during flight and others melt when they strike the melt pool surface. The powder particles impinging on the melt pool form the clad deposition layer after solidification. The development of laser cladding processes for various applications is hindered the lack of generally-applicable accurate models. Development of such models is impeded by the complexities associated with simultaneous injection of powered metal into melt pool formed by a focused laser beam. The powder cloud interacts with the laser beam and decreases the laser power density incident on the substrate and a molten pool formed on the substrate. The decrease in laser power due to transmission of the laser beam through the powder cloud is not entirely lost. Some of the lost energy heats powder particles and a portion of this thermal energy is returned to the molten pool by particles that are incident on it. These powder particles also add mass and momentum to the melt pool. These additions affect the fluid temperature distribution and flow patterns and the final shape of the deposited clad layer.

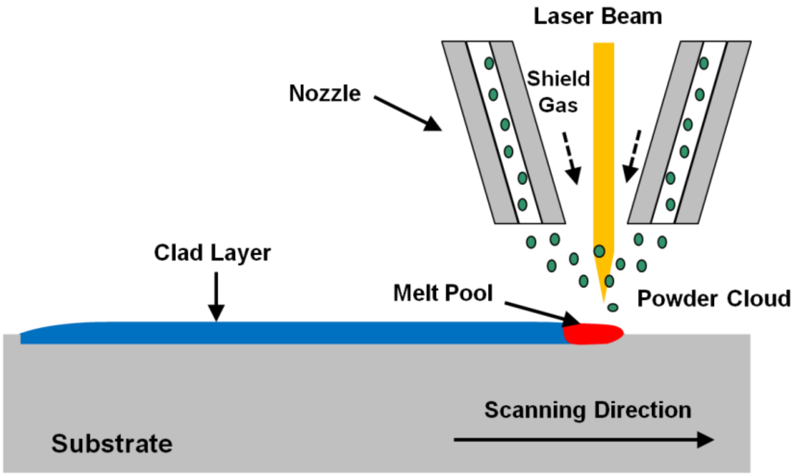

Figure 2.1 Schematic of laser cladding process using coaxial powder feed nozzle

Numerical simulations of the laser cladding process have been developed to add to the understanding of the underlying physical phenomena. Hoadley and Rappaz [3] developed a finite element model for laser cladding based on 2D heat conduction coupled with a number of analytical solutions of mass and momentum balances representing deposition of molten clad metal. Picasso and Rappaz [4] presented two approaches to model laser cladding process in 2D and 3D. The shape of the molted pool was computed at given laser power in 2D and the laser-powder-material interactions were taken into account in the 3D model. Toyserkani, Khajepour and Corbin [5] developed a transient finite element model for laser cladding with powder injection in three dimensions. Their model evaluated the correlation of beam velocity and powder feed rate to the clad layer geometry. In this model, the effect of heat flow due to fluid convection was incorporated by modifying the thermal conductivity of the clad layer. Choi, Han and Hua [6] described a numerical model that included most of the phenomena occurring during the cladding process. A Volume of Fluid simulation method (VOF) was employed to predict melt pool free surface evolution. They assumed feeding of metal droplets instead of powder particles and constant material properties were used for both liquid and solid metal to simplify the model. The effect of impurities on liquid surface tension was also neglected. Wen and Shin [7] presented a new comprehensive 3D model for the coaxial laser deposition, considering physical phenomena such as laser-powder interaction, fluid motion, mass addition and solidification. However, they did not account for the effect of surface active elements on weld pool convection and shape.

Marangoni convection patterns induced by surface active elements are known to have profound effects on weld pool shape and many previous investigations have been reported with regard to these effects. Sahoo, Debroy and McNallan [8] studied the effect of temperature and composition on surface tension of Ni-S system. Lee, Quested and McLean [9] reported temperature-dependent values for the surface tension and its gradient with electron beam melting of two distinct compositions of IN718 (20ppm S, 8 ppm O and 6ppm S, <10ppm O). Su and Mills [10] developed the calculation model for surface tension in IN718 with various sulfur and oxygen concentrations at ppm level.

Zhao, Kwakernaak, Pan, Richardson, Saldi, Kenjeres and Kleijn [11] reported studies of the effect of oxygen and temperature on surface tension of stainless steels in laser spot welding. However, the effect of surface active elements and associated convection patterns on the formation of laser melt pools has not been considered in prior laser cladding simulations where mass addition to the melt pool is considered.

The objective of paper is to describe the formulation of a transient three dimensional numerical model of the laser cladding process, to compare model predictions of laser clad deposit geometry to experimental measurements and to study the predicted weld pool convection flow patterns. The following sections discuss fundamental physical mechanisms and mathematical models used to represent the laser cladding process, the VOF numerical simulation technique, simulation predictions of single pass, single layer clad deposit geometry and comparisons to experimental measurements and conclusion and issues for further study.

2.2 Experimental Conditions

Single clad deposit were produced in autogenous Ni-superalloy IN718 laser cladding. 350 to 550W fiber laser power with uniform intensity (flat-top) was used to build the clad deposit on 5.08cm (height) ×5.08cm (length) ×0.226cm (thickness) substrate in argon atmosphere. The beam spot diameter and beam travel speed was 1.0mm and 1.016cm/s, respectively. Nominal composition of IN718 powder is shown in Table 2.1. Metal powder screened with 100-325 mesh was used to build the clad deposit.

Samples for metallographic cross sections were mounted, polished and then etched with standard metallographic method. No preheating or post-weld temperature control was used in the experiments. The clad deposit width, height and penetration are directly measured from optical images using image processing software (ImageJ, NIH) and used to validate the simulation results.

Table 2.1 Nominal composition of IN718 Powder in weight percent

Element	**C**	**Mn**	**Si**	**P**	**S**	**Cr**	**Ni**	**Mo**	**Nb**	**Ta**	**Ti**	**Al**
Quantity	.034	.008	.09	.006	<.0005	18.03	54.62	2.93	5.14	<0.002	.85	.59
Element	**Co**	**B**	**Cu**	**Pb**	**Bi**	**Se**	**Fe**					
Quantity	.11	.003	0.11	.00003	<.00001	<.00001	Bal					

2.3 Clad deposit modeling

Conservation of mass, energy and momentum form the basis for expressions used to model the laser clad melt pool and substrate. Also, it is important to account for the addition of energy by the focused laser beam and the addition of mass, energy and momentum by added metal powder for an accurate process model. The VOF method is adopted to simulate the fluid flow in the weld pool and to predict the evolution of weld pool shape, size and temperate as well as the temperature distribution in the substrate. In this work, the VOF laser cladding process simulation was implemented by integrating subroutines to represent laser heating and clad powder addition into available transport simulation software (Flow-3D, Flow Science Corp.).

2.3.1 Governing equations

Three dimensional mass conservation for VOF simulation of incompressible fluid flow is expressed by the equation

$$\frac{\partial \rho}{\partial t} + \nabla \cdot (\vec{v}\rho) = \dot{m}_S \tag{1}$$

where ρ is density of fluid in a numerical simulation mesh cell, t is time, $\vec{v}$ is liquid metal velocity and $\dot{m}_s$ is volumetric mass source rate. This conservation of mass relation can be rewritten in terms of a scalar value F which explicitly refers to the mesh used to discretize the simulation domain. F denotes volume fraction of fluid in a mesh cell defined in the numerical simulation. By definition, the value of $F = 0$ indicates that the corresponding simulation cell lies entirely within a void region and thus contains no fluid while $F = 1$ indicates the cell is entirely occupied by fluid. Hence, any cell having F values between 0 and 1 lies on the surface between fluid and void regions. The volume fraction of fluid and volume fraction source rate can be defined in terms of the density of fluid occupying a given cell as Equations (2, 3)

$$\rho = \rho_0 F \tag{2}$$

$$\dot{m}_S = \rho_0 \dot{F} \tag{3}$$

where it is re-iterated that ρ refers to density of fluid in a cell (ratio of mass of fluid in the cell and cell volume), ρ_0 is density of the fluid and F is volume fraction of fluid in the cell. A relation for conservation of F can be derived from Equations (1), (2) and (3), as [12]

$$\frac{\partial F}{\partial t} + \nabla \cdot (\vec{v}F) = \dot{F} \tag{4}$$

By simultaneously solving the time-varying volume fraction conservation law along with the momentum and energy conservation relations presented below, the time-varying location and shape of the fluid-void boundary can be predicted.

For conservation of momentum, the fluid is assumed to be Newtonian with laminar flow [13] The resulting conservation equation is

$$\frac{D\vec{v}}{Dt} = -\frac{1}{\rho}\nabla P + \mu\nabla^2\vec{v} + \vec{g}[1 - \beta(T - T_m)] + \frac{\dot{\vec{p}}_s}{\rho} \tag{5}$$

where P is hydrodynamic pressure, μ is viscosity, g is gravitational acceleration, T_m is melting temperature, β is thermal expansion constant, and $\vec{p}_s$ is a source term representing the momentum addition rate corresponding to the captured filler material droplets. Melt pool convection induced by buoyancy force due to thermal expansion of the melt is typically negligible in comparison to flow induced by surface tension gradient and was not included in this simulation.

In the simulations associated with free-surface fluid dynamics, the heat input, in this case from the laser beam, is imposed as part of a surface heat flux boundary condition. The heat is convected and conducted through clad the deposit melt pool and substrate. Conservation of thermal energy used in the simulation is given as

$$\frac{\partial h}{\partial t} + (\overrightarrow{v} \cdot \nabla)h = \frac{1}{\rho}(\nabla \cdot \lambda \nabla T) + \frac{\dot{h_s}}{\rho} \tag{6}$$

where h is enthalpy, λ is thermal conductivity and $\dot{h_s}$ is a source term representing enthalpy addition rate associated with captured filler material droplets. The expression above only considers thermal energy conservation in the weld pool. This is reasonable since weld pools are relatively small and fluid flow speeds are moderate so the kinetic and potential energy of the fluid is much smaller than the thermal energy. The latent heat due to solid to liquid phase change is included in the enthalpy-temperature relationship.

2.3.2 Boundary conditions and physical properties for the simulation

The boundary conditions applied to the lateral edges of the substrate (illustrated in Figure 2.2) were assumed as all solid walls to depict a rigid substrate with convection heat loss coefficient 10^5 erg/cm^2/C. The top and bottom surface boundary conditions were defined as continuous to model semi-infinite domain in the surfaces. Laminar flow and incompressible liquid were assumed for fluid flow in the weld pool. The simulation was modeled in three dimensional Cartesian system for description of the transport phenomena. The computation domain has dimensions of 0.8 cm in length (x-direction), 0.226 cm in width (y-direction) and 0.4 cm in height (z-direction) for transient flow shown in Figure 2.2. The z-direction has 0.3 cm of substrate and 0.1 cm void region above the substrate. The domain was meshed with cubic cells with 100 μm mesh size. To model laser heating and powder mass, energy and momentum inputs, a moving source of laser energy and mass flux is incorporated into the computation domain just above the top surface of substrate (labeled "Coaxial Nozzle" in Figure 2.2(b)). The initial temperature of the powder particles was assumed to be liquidus temperature. Thus, liquid particles having 50 μm in diameter leave the nozzle exit and are injected into the liquid pool. Mesh size and computation domain size independence of model results was verified. The ambient temperature assumed for material and surroundings was 300 K. The material used for both cladding powder and substrate was Ni-based superalloy, IN718. Thermophysical properties and the various welding parameters applied to this simulation were presented in Table 2.2 [14-16]. Fiber laser having flat-top distribution is used for this simulation. The laser beam power, beam spot size, powder particle size and beam travel speed were the values given directly from cladding process.

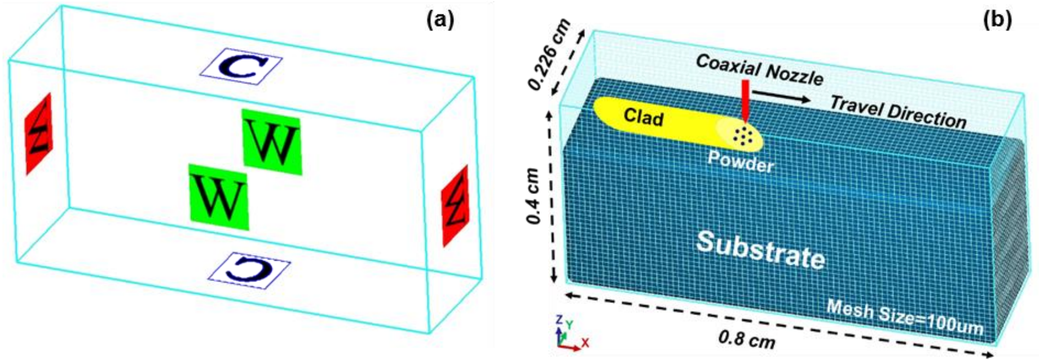

Figure 2.2 Boundary conditions for the edges of substrate and powder nozzle and (a) and description of computation domain (b)

Table 2.2 Thermophysical properties of IN718 and process parameters used in numerical model

Property	Symbol	Value	Ref.
Specific Heat of Liquid	C_L	7.25e+06 (cm^2/s^2/K)	14
Specific Heat of Solid	C_S	5.77e+06 (cm^2/s^2/K)	14
Conductivity of Liquid	λ_L	2.928e+06 (g-cm/s^3/K)	14
Conductivity of Solid	λ_S	2.792e+06 (g-cm/s^3/K)	14
Latent Heat	H	2.27e+09 (cm^2/s^2)	15
Power of Laser Beam	P	350, 450, 550 (W)	-
Beam Spot Size	B_S	1.0 (mm)	-
Powder Feed Rate	-	1.2 (g/min)	-
Powder Particle Size	-	50 (µm)	-
Liquidus	T_L	1623 (K)	16
Solidus	T_S	1423 (K)	16
Travel speed of Laser Beam	V	1.016 (cm/s)	-
Viscosity	η	0.196*exp(5848/T) (mPa)	14
Density of Liquid	D_L	7.3 (g/cm^3)	14
Density of Solid	D_S	8.19 (g/cm^3)	14

2.4 Laser Cladding Process Mechanisms and Models

Laser cladding is a fusion welding process that uses a focused, moderate power-density laser beam heat source and metal powder feed to melt and build-up layers of filler material onto a substrate. Modeling of energy conservation in laser cladding needs to account for losses that occur as the laser beam heats the substrate and the powder particles during their flight from the nozzle exit to the substrate as well as the efficiency of capture of laser powder into the deposited clad layer [17]. It is important to note that, although laser beam-powder interaction attenuates the laser beam power that is incident on the substrate, not all of the attenuated power is lost since some of it preheats the powder. Most of this portion of this laser power is returned to the cladding process when the heated particles are incorporated into the final clad deposit. Modeling of the laser cladding process should thus take into account absorptance of laser energy by the substrate and by powder particles, substrate and powder melting, transport phenomena in the melt pool, efficiency of capture of powder particles in the clad deposit, and solidification of melt to form a clad the deposit. Each of these topics is discussed in more detail below.

2.4.1 Absorptance of laser beam energy

Absorptance of laser energy by the clad material is a key laser cladding process parameter that varies with material composition and temperature. It has been found in previous studies that a reasonable estimate of laser energy absorptance is provided by the Hagen-Rubens [18] relationship. There, absorptance *A(T)* of the near infrared laser energy is calculated from the temperature-varying electrical resistivity of the substrate material $\rho_e(T)$ by the relation

$$A(T) = [8\varepsilon_0 \omega \rho_e(T)]^{1/2} \tag{7}$$

where ω is the angular frequency of the laser radiation (1.75 X 10^{15} rad/s for fiber laser radiation with wavelength λ = 1.07 X 10^{-6} m) and ε_0 is the permittivity of free space (8.85 X 10^{-12} F/m). The equation can be rewritten in terms of electrical resistivity as

$$A_{fl}(T) = 354.45\,[\rho_e(T)]^{1/2} \tag{8}$$

Expressions for temperature-varying resistivity [15] for solid and liquid IN718 are

$$\rho_e(T) = -0.960 + 0.005T - 3.919\times10^{-6}T^2 + 9.713\times10^{-10}T^3 \qquad \text{for solid phase} \tag{9}$$

$$\rho_e(T) = 1.251 + 1.364\times10^{-4}T \qquad \text{for liquid phase} \tag{10}$$

The calculated optical absorptance at the solidus temperature is 35.6% which corresponds well to a reported measurement of IN718 absorptance of 36% at T_s [19].

2.4.2 Energy balance

In this section, the relations used to calculate the distribution and losses of laser beam power in the laser cladding process are discussed.

2.4.2.1. Power balance

The efficiency of use of laser beam power to form a molten clad deposit on a substrate is decreased by power losses due to reflection, radiation, conduction and convection from both the clad powder and substrate. With reference to the substrate, the power balance can be expressed as [17]

$$Q_a = Q_l - Q_{rs} - Q_p - Q_{rp} - Q_{Radi.} - Q_{Conv.} \tag{11}$$

where Q_a is power absorbed by the substrate, Q_l is total power in the laser beam, Q_{rs} is incident laser power reflected by the substrate, Q_p is power absorbed by the fraction of the powder stream that is not included in the clad deposit, Q_{rp} is power reflected from the powder stream, $Q_{Radi.}$ is power lost from the substrate by radiation, and $Q_{Conv.}$ is power lost from the substrate by convection. A visual representation of Equation (11) is shown in Figure 2.3. It illustrates how the total laser power is redistributed by powder absorption and the various losses.

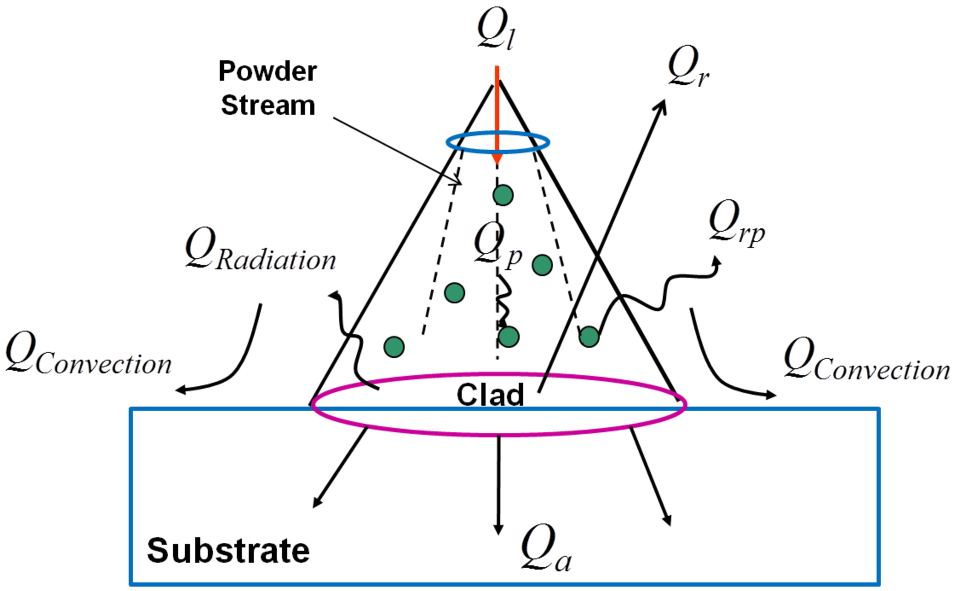

Figure 2.3 Energy balance during laser cladding process

Experiment measurements of the power losses noted above have been reported by Gedda [17] as 9% for $Q_{rp} + Q_p$, 1% for $Q_{Radi.} + Q_{Conv.}$ and 52% for Q_{rs}. From the values, the fraction of laser power absorbed by the substrate is calculated from Equation (11) as Q_a = 38%. Notice that the reflection from substrate and powder stream are the largest losses from the cladding process. Laser power absorption by an ionized plasma is neglected because the near infrared laser wavelength ($\lambda = 1.07$ μm) and moderate focused power density ($7x10^4$ W/cm^2) yield negligible absorption [20]. Figure 2.4 gives schematic flow of energy losses.

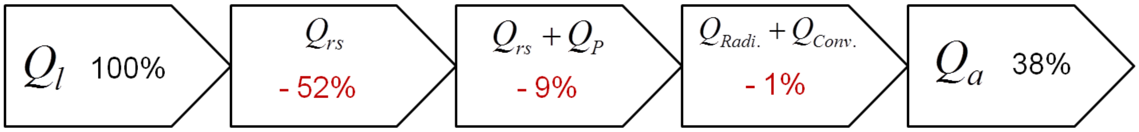

Figure 2.4 Distribution of laser energy in the laser cladding process

Total absorbed energy by the substrate, Q_a can be rewritten as

$$Q_a = Q_c + Q_F \tag{12}$$

where Q_c is the fraction of the total laser power utilized in melting the clad deposit and Q_F is the fraction of total laser power used in heating the substrate. Q_c can be calculated by

$$Q_c = Av\rho(C_p \Delta T + \Delta H) \tag{13}$$

where A is area of weld bead, v is laser beam travel speed, ρ is density of the melted material, C_p is specific heat of the melted material, ΔT is temperature difference between liquidus and room temperature and ΔH is latent heat of the clad melt. From the calculation, it is shown that percentages of total laser power used for melting clad deposit and heating of the substrate are $Q_c = 8.4\%$ and $Q_F = 29.6\%$ respectively.

2.4.2.2. Powder catchment efficiency (η)

The powder catchment efficiency can be estimated by the fraction of powder particles that impinge on the molten area of the substrate. For single-pass, single-layer laser cladding, it may be assumed that any particles which strike the melt pool will become part of the clad layer. In this approximation, all particles which do not impinge on the pool can be considered as lost. This is reasonable because powder particles which are not melted during their flight through the laser beam are likely to be reflected from the solid substrate and those that are melted may adhere to the substrate but can still be considered as lost because they do not contribute to formation of the single-pass clad layer. With this assumption and an additional requirement that the powder jet impingement area is larger than the melt pool, powder catchment efficiency can be defined as ratio between the molten pool area and the substrate area impinged by the power jet [21].

$$\eta = \frac{S_{jet}^{liq}}{S_{jet}} \tag{14}$$

Please note that assumptions the molten area can vary with laser power change and jet area is larger than the molten pool area in this computation which are depicted in Figure 2.5. Jet area is constant for different laser powers while the molten pool area increases proportionally as a function of the laser power.

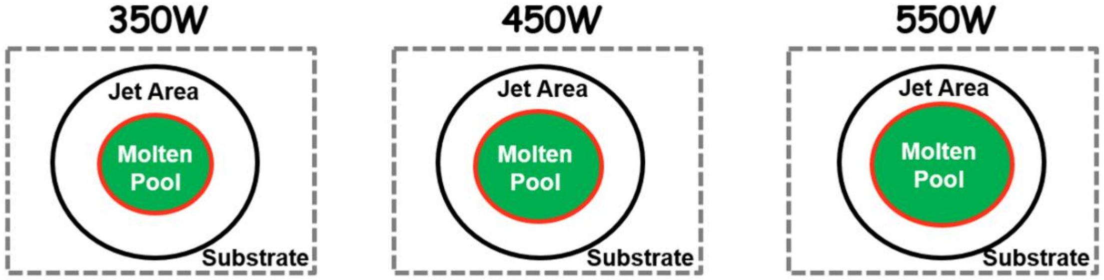

Figure 2.5 Assumption for powder catchment efficiency

2.4.3 Melt pool fluid surface tension

The variation of surface temperature across the laser melt pool surface caused fluid surface tension gradients and induced surface fluid flow from low to high surface tension regions. Such Marangoni flows have been found to have significant effects on weld pool circulation patterns and weld pool shape [22]. The amount of surface active element sulfur in the alloy strongly affects the sign and magnitude of surface tension gradients and associated Marangoni flow. It has been reported that the behavior of sulfur in IN718 can be assumed to be the same as that in Fe-Ni-Cr alloys [9]. Thus, in this study, the behavior of sulfur is accounted for by an equation applicable to a Fe-Ni-Cr-S alloy [21]. Also, the effect of Cr-S interaction is considered in an activity term since Cr changes the activity of S whereas Ni has negligible effects on the activity of S. The values of surface tension gradient used in the simulation were calculated using Equation (15) and material properties [14,23-25].

$$\gamma = \gamma_m^o - A(T - T^0) - RT\Gamma_s \ln[1 + a_i k \exp^{-(\frac{\Delta H^o}{RT})}] \tag{15}$$

Here γ^0_m =1842 dyne/cm is the surface tension of the pure metal at reference melting temperature T^0, A=0.11 is a coefficient for the variation of surface tension at temperature T above the liquidus, R= 8.314 J/mol-K is the gas constant, $\Gamma_s = 2.27\times10^{-9}$ g-mol/cm^2 is surface excess at saturation, k= 3.18×10^{-3} is entropy segregation constant and ΔH^0= -1.661× 10^{-5} J/mol is enthalpy of segregation. a_i is the activity of species i in solution. For the alloy used in the present study, transition temperature of surface tension gradient is predicted at 1801K, marked as T_i in Figure 2.6.

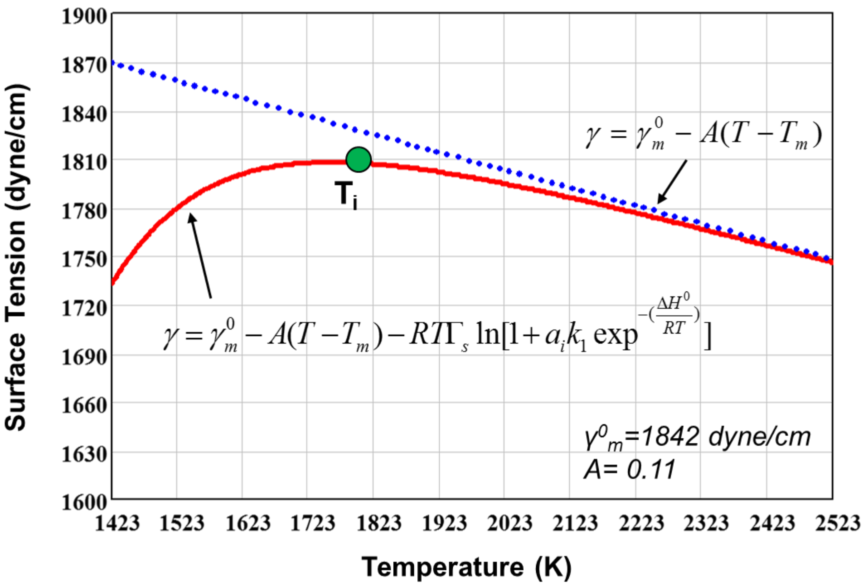

Figure 2.6 The temperature and surface active element dependent values of surface tension

2.4.4 Melt solidification

In metal alloys, it is known that solidification morphology is significantly affected by the combination of temperature gradient (G) in the liquid at the solidification boundary and solidification rate (R) as presented in Figure 2.7 [26].

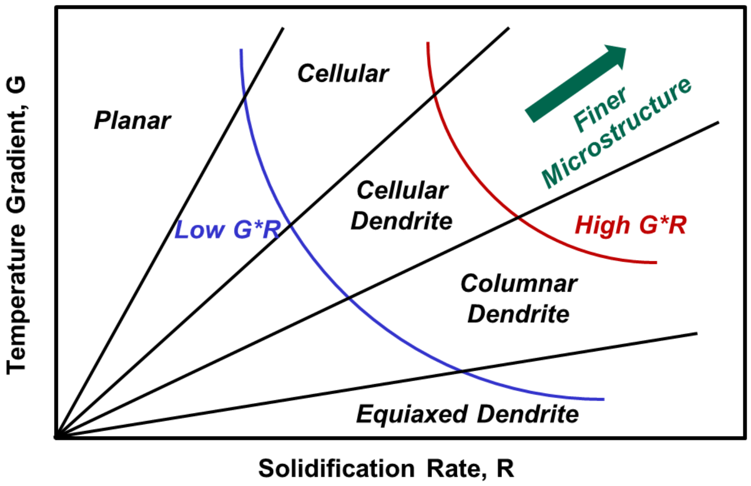

Figure 2.7 Effect of G and R on solidification morphology

A planar growth mode occurs when G is very high or/and R is extremely low value. As R increases, the solidification morphology can shift to cellular, columnar and then equiaxed dendritic. Most metal alloys solidify in cellular or columnar dendritic mode. The cellular and columnar growth modes are produced when the growth of crystal structures occurs without formation of any secondary dendrite arms. If additional dendrite arms form, the solidification mode shifts to dendritic. Equiaxed dendritic morphology is possible only when G is very low.

As the cooling rate, which is the product of G and R, increases, finer microstructures are produced. Note that high cooling rate results in much closer spacing between cellular or dendrite arms. Eventually, the finer microstructure leads to increased mechanical properties. In general, it is known that cooling rate in laser cladding varies with the processing parameters [2] and is faster (10^2 -10^6 K/s) than that of conventional casting. Therefore, the influence of processing parameters on G and R and the solidification morphologies that occur will be assessed in this study.

2.5 Results and discussion

2.5.1 Powder catchment efficiency

The metal powder catchment efficiency [27] and resulting mass flow rate of powder into the melt pool used in the simulation were calculated from experimental results and results given in the literature. As shown in Table 2.3, the catchment efficiency was 45% and the mass flow rate was 1.2 g/min for a laser 550W. The mass flow rates at 350W and 450W were proportionally adjusted from the 550W value based on the laser power ratio. Lower laser power creates smaller molten area on the substrate, S^{liq}_{jet} according to Equation (14). By scaling, the molten pool area at 350W is 63.6% of the area at 550W. From the assumptions, the efficiencies for 350W and 450W are calculated to be 28.62% and 36.81%, respectively.

Table 2.3 Calculation of catchment efficiency

Power	**Mass Flow Rate Setting (g/sec)**	**Efficiency (%)**	**Mass Rate into Molten Pool (g/sec)**
350W	**0.020**	**28.62%**	**0.00573**
450W		**36.81%**	**0.00736**
550W		**45.00%**	**0.00900**

2.5.2 Melt pool size: experiment vs. simulation

The width, height and penetration depth of the deposit are compared to the simulation results by X-Y (a) and Y-Z (b) views in Figures 2.8(a) and (b). A dotted line indicating the simulation liquid-solid weld pool boundary is overlaid onto each corresponding experimental image. These results show that simulated weld pool shapes and dimensions are comparable to the experiments. Quantitative comparisons of simulated and experimental clad width, height and penetration depth are shown in Figure 2.9. The weld pool dimensional are plotted for laser powers of 350W, 450W and 550W. The experimental results are comparable to the simulation predictions. Note that increased laser power leads to increased weld width and penetration depth while the clad height is relatively constant. The clad height is relatively constant because the powder flux within the jet area is constant and the jet area is larger than the weld pool surface area in all simulation cases (c.f. Figure 2.5). Thus, the larger melt pool surface area results in increased powder catchment efficiency and more mass addition to the molten pool (c.f. Table 2.3) but not increased clad height.

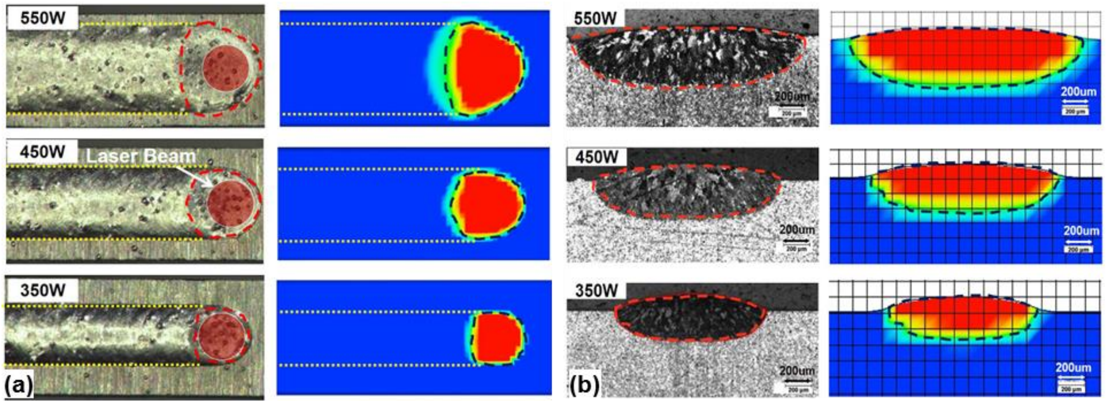

Figure 2.8 Top-down (a) and cross section (b) views at the same magnification for comparison of simulated and experimental single pass laser clad melt pool and deposits at various powers. Dashed lines in simulation images show the position of liquidus isotherm while dashed lines in experimental images show the liquidus isotherm from the corresponding simulation

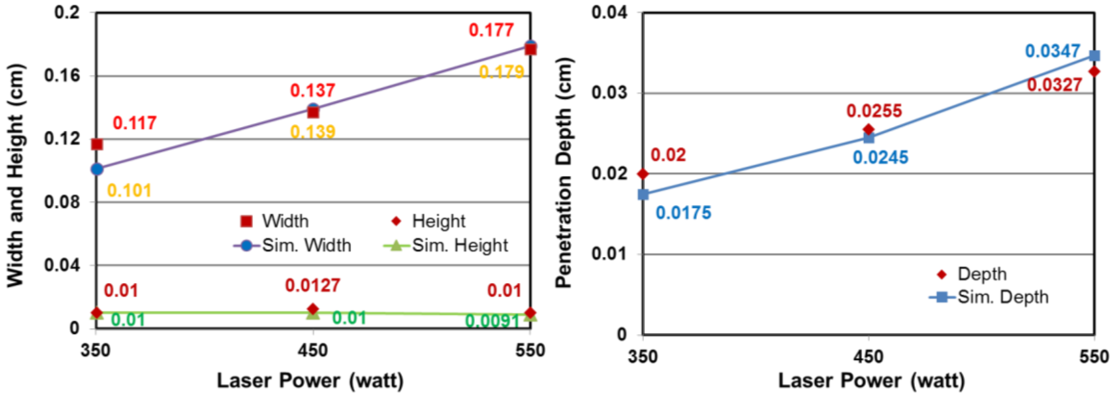

Figure 2.9 Comparison of simulated and experimental weld pool dimensions

2.5.3 Fluid flow patterns in melt pool

As discussed in section 2.4.3, a fluid circulation known as Marangoni flow occurs the weld pool surface. Resulting convective flow in the melt produces weld pool temperature gradients. Figure 2.10 shows the temperature profile and corresponding temperature gradient, G along the clad centerline t = 0.43 sec. The quasi-steady state solidification rate on the weld centerline at the back of the weld pool is constant and equal to the laser travel speed, 1.016cm/s. The calculated values of $G = 3.0*10^3$ K/cm and R = 1.016 cm/s are comparable to values found in literature [28] for the observed columnar dendritic solidification mode. Although other conditions in the above cited reference vary somewhat from those applicable for laser cladding, it is reasonable to expect similar solidification morphology. The simulated weld pool shape is shown in a grey inset to explain the relationships between temperature profiles, temperature gradient, fluid flow pattern and weld pool shape. The orange line indicates the weld pool length, which ranges from 0.380 cm to 0.537 cm at the simulation time 0.43 sec. Surface temperature on the weld centerline increases from liquidus at the back of the pool to about 1900 K and the remains constant over a region that also corresponds to the deepest weld pool penetration. Further towards the front of the pool, the surface is heated by laser beam heat input, the temperature increases further. The variation of weld pool centerline surface temperature gradient is calculated as the first derivative of surface temperature. The temperature gradient equals zero near the center of the laser focus spot (around 0.5 cm) and becomes negative at the front edge of the pool. Note that the deep-penetration region of the weld pool has flat centerline surface temperature profile and relatively small temperature gradient. It can be reasoned that the flat profile can be attributed to convective fluid flow patterns in the regions toward the back of the weld pool.

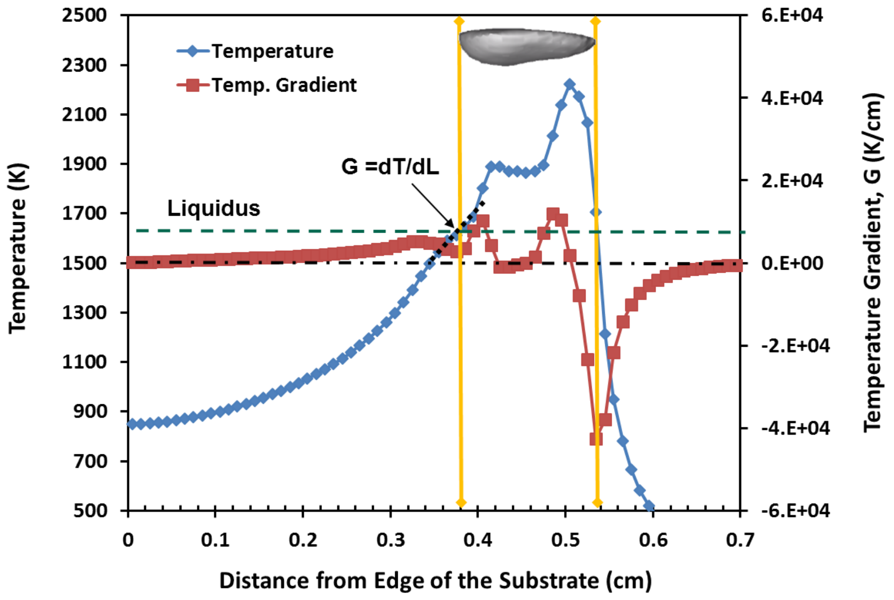

Figure 2.10 Quasi-steady state temperature profile and temperature gradient (G) along the weld pool centerline at time t=0.43s

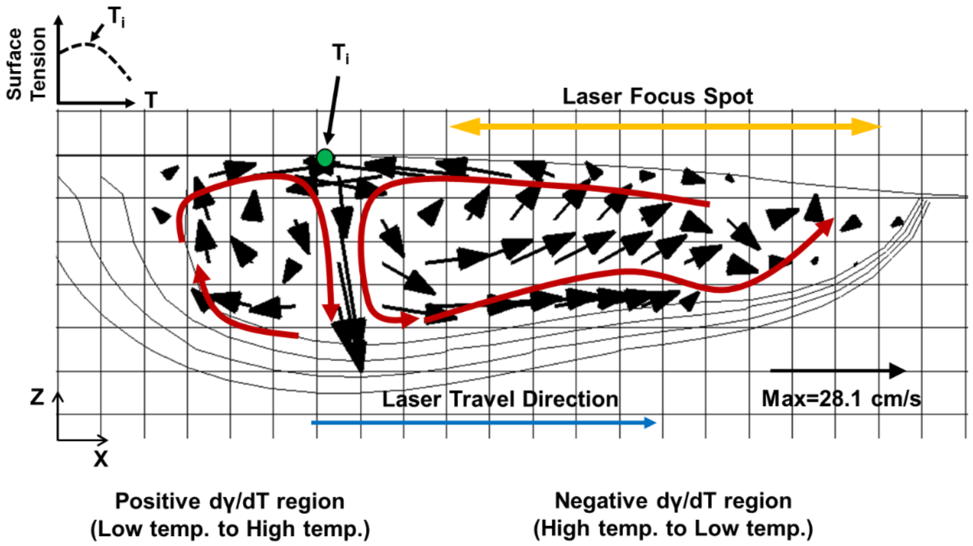

Figure 2.11 Longitudinal-section view showing fluid flow and mixing in the laser clad melt pool, the location of laser focus spot. The green dot indicates the location of the weld pool surface with temperature T_i where surface tension gradient transitions from positive to negative.

Figure 2.11 displays the flow pattern in the weld pool. Surface areas with positive and negative surface tension gradient are both found on this weld pool. The transition temperature T_i that divides the two regions is calculated from Equation (15) and displayed in the plot in Figure 2.6. Its location on the pool surface is represented with green dot in Figure 2.11. Surface tension gradients generate surface flow from areas with low surface tension to areas with high surface tension. Thus, surface flow tends to carry higher temperature fluid from the area heated by the laser beam towards the trailing edge. However, at a same time, flows originating at the cooler back edge of the pool tend to deliver lower temperature fluid towards the front. The two opposing surface flows end up colliding and mixing in a region intermediate between the laser focus spot and the trailing pool edge where the liquid surface temperature is equal to the transition temperature T_i (represented by the green dot in Figure 2.11). As a result of the mixing of opposing hotter and cooler flows from the front and rear portions of the melt pool, temperature is relatively uniform in that region and gradient is correspondingly small (c.f. Figure 2.10). Also the downward flow (produced by colliding surface flows) is strongest and the resulting weld pool penetration is deepest near this point. Although experimental validation of this weld pool penetration contour has not been completed, the fact that simulation predictions of clad penetration, width and height are close to experimental values provides indirect evidence that the weld pool contour is reasonable. We also note that a similar pool profile has been predicted in autogenous gas tungsten arc welding [29].

The weld pool surface tension and fluid flow patterns are shown in 2D and 3D plots in Figure 2.12. It is seen that two opposing flows meet at the line showing the position of the transition temperature T_i (b) and generate downward mixing flow along this line (c). In Figure 2.13, the variation of fluid flow patterns are assessed in consecutive 2D cross-sections spaced evenly along the X-axis.

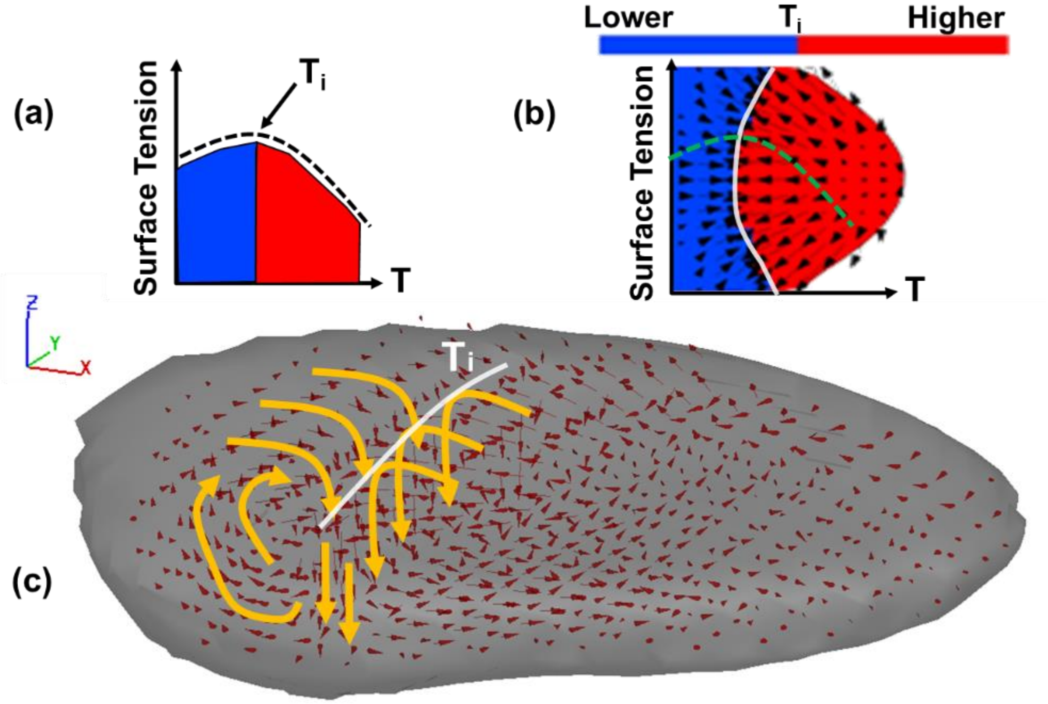

Figure 2.12 Three dimensional depiction of weld pool convection flows (c) with inset figures showing temperature-dependent surface tension (a) and surface temperature (b). In (a), surface tension gradient switches from positive to negative at T_i. In (b), T_i separates the positive (blue) and negative (red) surface tension regions. The two opposing surface flows impinge along the line where surface temperature equals T_i.

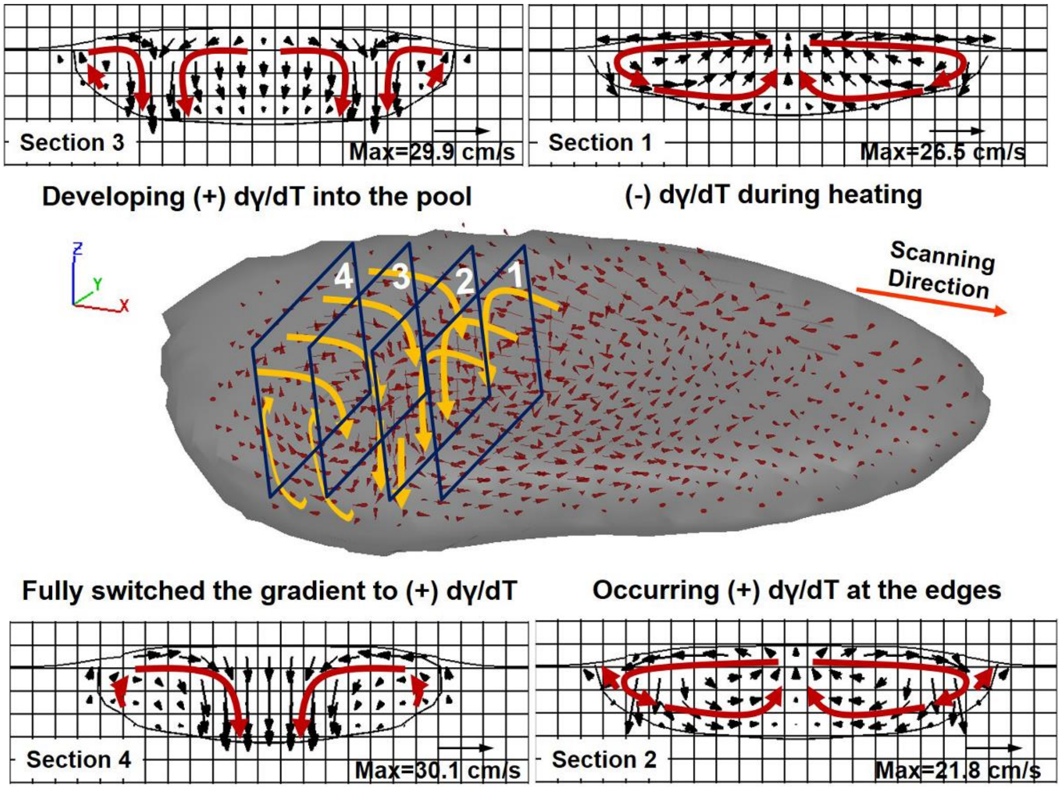

Figure 2.13 3D and 2D plots showing fluid flow and mixing in laser clad melt pool

Dominant outward-directed Y-axis Marangoni flows are observed on the weld surface with maximum velocity 26.5 cm/s in section 1. This pattern of the flow indicates that only negative surface tension gradient resulting in completely outward flow is present at this region. In section 2, the main Marangoni flow is still outward direction at the center of the weld pool due to negative surface tension gradient and relatively high temperature at that region. Note that inward fluid flows which are opposite to the flow at the center in direction are observed near the outermost edges of the pool. This flow pattern indicates switching of surface tension gradient from negative to positive. The fluid velocity is reduced to 21.8cm/s due to the opposing flow. In section 3, prominent inward and outward surface flows with comparable velocities exist. Downward flow is found at the intermediate region between the weld edge and center where the surface flows collide. As the distance from laser beam increases, weld pool temperature decreases and eventually it reaches the temperature switching surface tension gradient. Hence, the region showing the dominant positive gradient keeps widening but the expansion stops at the gradient transition region. The maximum flow velocity is found at the region where the two opposite flows meet. In section 4, the gradient is fully switched to positive. Thus, only inward and downward flows are seen.

2.6 Summary, conclusions and future work

A transport simulation of the laser cladding process was used to understand the effect of convection flow on the cladding melt pool formation and solidification conditions in IN718 deposits. Predicted clad width, height and penetration depth at different laser powers were found to be comparable to experimental measurements. Due to heat flow in the melt pool induced by Marangoni convection, the most deeply penetrated region was formed towards the back of the weld pool, behind the laser focus spot but ahead of the rear solidification boundary. The increased penetration was formed in this region by impingement of opposing surface flows caused by positive and negative X-axis surface tension gradients along the weld centerline. The flow pattern also caused the weld pool to have a relatively flat rear boundary and contributed to a relatively uniform temperature distribution in the melt pool in the region where opposing surface flows impinged. Also, temperature gradient was calculated along the weld pool center line and, in combination with the centerline solidification rate at the back edge of the weld pool was used to predict columnar dendritic solidification. The correspondence with the observed weld pool solidification mode was noted. Future simulation and experimental efforts are planned to extend the work to multiple layer clads and to experimentally validate the weld pool convection patterns and penetration profiles predicted by the simulations.

2.7 Acknowledgement

The authors would like to thank Rolls-Royce Corporation for the funding support and providing laser cladding samples in this work. They also appreciate NSF-I/UCRC: Center for Integrative Materials Joining Science for Energy Applications. The authors express their thanks to J.S.Bader for helpful suggestions and interest in this project.

2.8 References

1. Zhong M, Liu W (2010) Laser surface cladding: The state of the art and challenges. Journal of Mechanical Engineering Science 224(C5):1041-1060.

2. A.Weisheit, Gasser A, Backes G, Jambor T, Pirch N, Wissenbach K (2013) Laser-assisted fabrication of materials - direct laser cladding , current status and future scope of application, vol 161. Springer New York

3. Hoadley AFA, Rappaz M (1992) A thermal model of laser cladding by powder injection. Metallurgical Transactions B 23(5):631-642.

4. Picasso M, Rappaz M (1994) Laser-powder-material interactions in the laser cladding process Journal De Physique IV 4(C4):27-33.

5. Toyserkani E, Khajepour A, Corbin S (2004) 3-d finite element modeling of laser cladding by powder injection: Effects of laser pulse shaping on the process. Optics and lasers in engineering 41(6):849-867.

6. Choi J, Han L, Hua Y (2005) Modeling and experiments of laser cladding with droplet injection. Journal of Heat Transfer 127(9):978-986.

7. Wen S, Shin YC (2010) Modeling of transport phenomena during the coaxial laser direct deposition process. Journal of Applied Physics 108(4):044908

8. Sahoo P, Debroy T, Mcnallan MJ (1988) Surface tension of binary metal-surface active solute systems under conditions relevant to welding metallurgy. Metallurgical Transactions B 19B(3):483-491.

9. Lee PD, Quested PN, McLean M (1998) Modelling of marangoni effects in electron beam melting. Philosophical Transactions of the Royal Society of London 356(1739):1027-1043.

10. Su Y, Mills KC (2005) A model to calculate surface tension of commercial alloys. Journal of Materials Science 40(9-10):2185-2190.

11. Zhao CX, Kwakernaak C, Pan Y, Richardson IM, Saldi Z, Kenjeres S, Kleijn CR (2010) The effect of oxygen on transitional marangoni flow in laser spot welding. Acta Materialia 58(19):6345-6357.

12. Cho MH, Lim YC, Farson DF (2006) Simulation of weld pool dynamics in the stationary pulsed gas metal arc welding process and final weld shape. Welding Journal 85(12):271-s to 283-s.

13. Cho JH, Farson DF, Milewski JO, Hollis KJ (2009) Weld pool flows during initial stages of keyhole formation in laser welding. Journal of Physics D: Applied Physics 42(17):175502.

14. Mills KC (2002) Recommended values of thermophysical properties for selected commercial alloys. Woodhead, Cambridge, England

15. Pottlacher G, Hosaeus H, Kaschnitz E, Seifter A (2002) Thermophysical properties of solid and liquid inconel 718 alloy. Scandinavian Journal of Metallurgy 31(3):161-168.

16. Lewandowski MS, Overfelt RA (1999) High temperature deformation behavior of solid and semi-solid alloy 718. Acta Materialia 47(18):4695-4710.

17. Gedda H, Powell J, Wahlstrom G, Li WB, Engstrom H, Magnusson C (2002) Energy redistribution during co_2 laser cladding. Journal of Laser Applications 14(2):78-82.

18. Xie J, Kart A, Rothenflue JA, Latham WP (1997) Temperature-dependent absorptivity and cutting capability of CO_2 , Nd:YAG and chemical oxygen-iodine lasers. Journal of Laser Applications 9 (2):77-85.

19. Shelton JA, Shin YC (2010) Comparative evaluation of laser-assisted micro-milling for aisi 316, aisi 422, Ti-6Al-4V and inconel 718 in a side-cutting configuration. Journal of Micromechanics and Microengineering 20(7):075012.

20. Kim KR, Farson DF (2001) Co2 laser-plume interaction in materials processing. Journal of Applied Physics 89(1):681-688.

21. Picasso M, Marsden CF, Wagniere JD, Frenk A, Rappaz M (1994) A simple but realistic model for laser cladding. Metallurgical and Materials Transactions B 25B(2):281-291.

22. Kou S (2012) Fluid flow and solidification in welding: Three decades of fundamental research at the university of wisconsin. Welding Journal 91(11):287S-302S.

23. Zacharia T, David SA, Vitek JM, Debroy T (1989) Weld pool development during gta and laser beam welding of type 304 stainless steel--part I: Theoretical analysis. Welding Journal 68(12):499-s to 509-s.

24. Mcnallan MJ, Debroy T (1991) Effect of temperature and composition on surface tension in fe-ni-cr alloys containing sulfur. Metallurgical Transactions B 22B(4):557-560.

25. Anderson TD, DuPont JN, DebRoy T (2010) Origin of stray grain formation in single-crystal superalloy weld pools from heat transfer and fluid flow modeling. Acta Materialia 58(4):1441-1454.

26. Kou S (2003) Welding metallurgy. 2nd edn. John Wiley & Sons, New Jersey

27. Weisheit A, Backes G, Stromeyer R, Gasser A, Wissenbach K, Poprawe R Powder injection: The key to reconditioning and generating components using laser cladding. In Proceedings of International Congress on Advanced Materials and Processes, Materials Week 2001, Munich, Germany. pp pp. 1-7

28. Lim YC, Yu X, Cho JH, Sosa J, Farson DF, Babu SS, McCracken S, Flesner B (2010) Effect of magnetic stirring on grain structure refinement--part i: Autogenous nickel alloy welds. Science and Technology of Welding and Joining 15(7):583-589.

29. Zhao YZ, Lei YP, Shi YW (2005) Effects of surface-active elements sulfur on flow patterns of welding pool. Journal of Materials Science & Technology 21(03):408-414.

Chapter 3: Effect of Fluid Convection on Dendrite Arm Spacing in Laser Deposition

3.1 Introduction

Methods for increasing the overall efficiency of aircraft engines and gas turbines can reduce operating cost and environmental impact (e.g. emission of CO_2) and has long been an issue among manufactures of these systems. Higher operating temperature is effective to increases the efficiency of turbines but components are exposed to higher temperatures and their properties may be significantly degraded. For example, in high-efficiency gas turbine engines [1], the gas stream passing through combustor has a temperature as high as 1500 °C. Turbine blades are exposed to high temperatures, a corrosive gas atmosphere and high operating stresses. Wear is particularly severe at the tips of the blades since high operating efficiency requires small clearance between rotating turbine blade tips and the outer stator casing. This small clearance contributes to tip wear by mechanisms of erosion, corrosion, oxidation, deformation and adhesive transfer, singly or in combination [2]. Since tip wear limits the life of blade life, repairing worn turbine blade tips is of great economic interest [3].

Laser cladding technology has been popularly utilized to apply worn protection layer on metallic surfaces or to repair damaged surfaces of structural parts [4]. In laser cladding with blown powder, the powdered metal clad materials are delivered through multiple powder feed nozzles placed annularly around the laser beam, into a laser-generated melt pool as a form of powder particles that are carried by an inert gas [5]. The schematic description is shown in Figure 2.1 [6]. Some powder particles are heated by the laser beam during flight and others are melted once they alight on the liquid melt pool surface. Only powder particles landing in melt pool contribute to formation of the clad deposit layer after solidification. The other particles alighting outside of melt pool will ricochet off and be lost. The development of laser cladding process is required for generally-applicable accurate model. However, the complexity associated with interaction between powder particles, laser beam and substrate makes simulation difficult. Total absorbed laser power density is modified by interaction between laser beam and powder cloud. Moreover, powder input accompanies with corresponding amount of mass and momentum into the melt pool. Thus, temperature distribution and fluid flow patterns in the weld pool will be changed and subsequently resultant shape of the clad deposit.

Ni superalloy is the metal most widely used for hot section component in the engine because it is very resistant to corrosion and maintains reasonably high strength at elevated temperature. In aircraft engine and gas turbine engine systems, single crystalline structures have been popularly used due to better creep resistance and fatigue behavior. However, the production cost of single crystal is not only significantly expensive due to complexity of process parameter control but also Ni superalloy itself is high in price [7]. Thus, repair of the damaged parts instead of replacing have been strongly required from industry fields. In this research, laser cladding process is used to repair the damaged part. However, property degradation and micro-cracks are observed in the Ni superalloy clad deposit. Therefore, a better understanding for the parameter-microstructure relationship of the clad deposit is required to solve the problems.

3.1.1 Fluid Dynamics and its effect on weld pool shape

The variation of surface tension that is present on the laser melt pool causes the molten metal to flow from low surface tension to higher surface tension region. The variation in the surface tension is mostly derived from two sources. Surface tension is a temperature dependent value so that temperature gradient across the weld pool results in surface tension gradient on the melt pool surface. In addition, for the alloys, the compositional gradient on the weld pool surface leads to surface tension gradients, and changes fluid flow patterns.

Such Marangoni flows have been found by Heiple *et al.* [8,9] and its significance on weld pool circulation patterns and weld pool shape was confirmed by other researchers [10,11]. It is well known that the fluid always moves from low to higher surface tension region [12,13]. In negative surface tension gradient for pure metal (a), the surface tension induces radially outward flow from high (center, C) to lower temperature region (edge, E) where the weld pool becomes shallow and wide whereas in positive gradient region (b), the flow moves radially inwards from low (edge, E) to higher temperature region (center, C) where the weld pool becomes deep and narrow. It is pointed out that positive to negative transition at a certain temperature can occur and produce complex fluid flow (c). T_i is the transition temperature of surface tension.

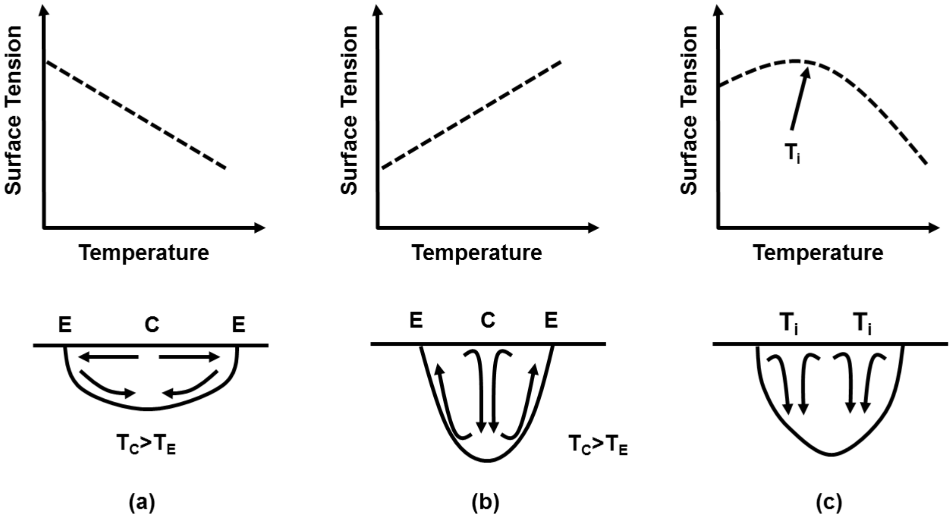

Figure 3.1 Different fluid flow pattern produced by different surface tension gradient

As seen previously, the compositional gradient in alloy alters Marangoni flow patterns that change the shape of weld pool. Thus, many studies have been conducted with regard to the compositional effects. The influence of composition and temperature on surface tension in the Ni-S system has been previously investigated [14]. The effect of sulfur and oxygen on surface tension and its gradient was reported for electron beam melting of IN718 [15]. The developed calculation model was suggested to know the effect of sulfur and oxygen at ppm level [16]. Detailed study of the influence of oxygen and temperature gradient on surface tension was recently reported with stainless steels in A-TIG welding and in laser spot welding [17,18]. However, the composition effect on fluid pattern and associated laser melt pool shape has not been studied in prior laser cladding simulations.

3.1.2 Correlation of the weld pool shape with solidification microstructure

During transformation from liquid to solid, the solidification behavior controls the distribution of solute, and the size and morphology of grains [19]. The critical parameters determining the solidification microstructure are the temperature gradient G, solidification rate R, undercooling ΔT, and alloy constitution. Depending on these conditions, the microscopic shape of the solid-liquid interface varies from planar to cellular dendritic, to columnar dendritic, and to equiaxed dendritic. Pure metals have a planar solid-liquid interface and solidify as a single crystal. However, in alloys, the factors affecting solidification morphology are more complicated because redistribution of alloy elements leads to concentration gradients adjacent the solid-liquid interface. When the actual temperature of liquid ahead of the solidification interface is lower than the equilibrium liquidus temperature corresponding to the composition variation, constitutional supercooling occurs and the planar interface is unstable. The criteria for the stability of the planar solid-liquid interface can be expressed as [20]

$$\frac{G_L}{R} > \frac{\Delta T_S}{D_L}, \qquad (1)$$

where G_L is the temperature gradient in liquid region, R is the solidification rate, ΔT_s is the solidus and liquidus temperature difference and D_L is the diffusion coefficient in liquid region. Therefore, the constitutional supercooling determines the solidification mode at the rear solidification boundary of a traveling weld pool.

The size and morphology of the solidified microstructure can be revealed by using the combined form of temperature gradient G and solidification growth rate R which is shown in Figure 3.2 [20]. The ratio of G/R indicates solidification morphology whereas the product of G and R represents the scale of the solidification microstructure.

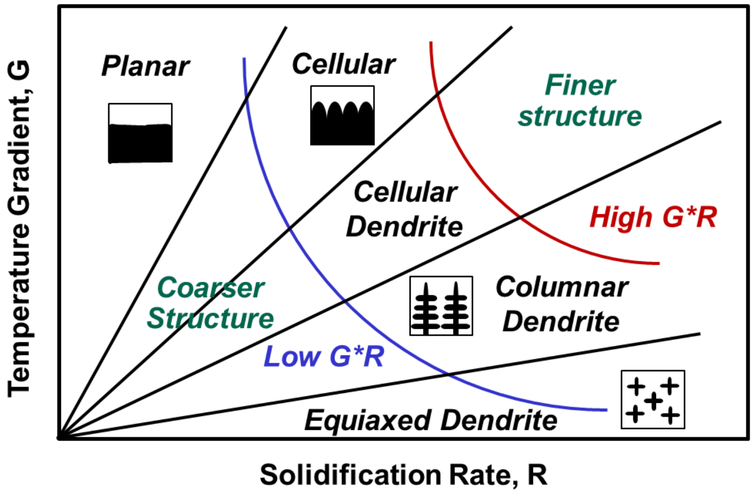

Figure 3.2 The effect of G and R on the solidification morphology and size

A planar growth occurs when G is very high or/and R is extremely low value. As R increases, the solidification morphology can shift to cellular, columnar and then equiaxed dendritic. Most metal alloys are solidified in cellular or columnar dendritic mode. The cellular and columnar growth mode are produced when the growth of crystal structures occurs without formation of any secondary dendrite arms. If additional dendrite arms form, the structures are shifted to dendritic mode. Equiaxed morphology is possible only when G is very low.

As the cooling rate of the liquid in front of the solidification boundary (which is the product of G and R) increases, a finer dendritic solidification microstructure results. Eventually, the finer microstructure leads to increased mechanical property of metals. In general, it's known that cooling rate in laser cladding typically varies in the range from 10^2 -10^6 K/s, than that of conventional casting and it is a function of the processing parameters [4].

As seen above, in addition to the temperature gradient G, the solidification rate R plays a very important role in determining solidification size and morphology. However, measuring precise G and R values is very difficult because they vary considerably from point to point along the weld pool boundary. Furthermore, measuring G_L is very complicated due to fluid convection in the weld pool. Therefore, numerical simulation including heat transfer and fluid convection is a good alternative to experimental measurement of G and R [21].

Analytical models for the prediction of solidification morphology and size have been presented in prior publications. Columnar to equiaxed transition (CET) was predicted by a theoretical expression that included solidification variables G and R [22]. Additional studies have been carried out to understand the degradation of mechanical properties caused by equiaxed grains in laser and electron beam welds on Ni-based single crystal superalloys [23,24]. Relationships for the prediction of secondary dendrite arm spacing (SDAS) from G and R values have been presented for hybrid laser-arc welding [25]. Results showed that the size of the microstructure varied by location in the weld pool.

The main purpose of this study is to use a numerical simulation to obtain thermal conditions G, R and solidification cooling rate ,and then to use these values in theoretical models for prediction of the primary dendrite arm spacing. Dependence of microstructure in size on solidification variables is investigated by comparison of the predicted primary dendrite arm spacing using G and R as an input to experimental measurements.

3.2 Flow and Solidification Model

3.2.1 Weld pool shape and solidification conditions

In order to obtain high quality cladding conditions experimentally, a large number of experiments are needed because numerous variables such as laser power, speed, powder feed rate and catchment efficiency must be optimized [26]. Moreover, direct measurement of weld pool flow and temperature distribution is even more difficult since the pool is very hot and small, and heating and cooling rates are very fast. An accurate numerical simulation can provide the weld pool conditions without the difficulties associated with measurements. In this work, a 3D weld pool simulation was implemented and used to predict weld pool shape, temperature gradient G and solidification rate R for single layer, single track deposits. Heat transfer, fluid flow, mass addition, and laser-powder-substrate interaction were included in the simulation. Ni-based superalloy, IN718 was used for clad powder and substrate properties in the simulation.

During the laser cladding process, laser-heated powder is continuously added and the mass, momentum and energy additions change the weld pool shape and clad geometry. Thus, three important governing equations of mass, energy and momentum conservation should be solved for reasonable modeling of laser cladding. To investigate fluid behavior in the weld pool and free surface change, the volume of fluid (VOF) method is utilized in this study. The conservation equations are solved by commercial software (Flow-3D, Flow Science Corp.).

$$\frac{\partial \rho}{\partial t} + \nabla \cdot (\vec{v}\,\rho) = \dot{m}_s \qquad \textit{Conservation of mass,} \qquad (2)$$

$$\frac{\partial h}{\partial t} + \overrightarrow{(v} \cdot \nabla)h = \frac{1}{\rho}(\nabla \cdot \sigma \nabla T) + \frac{\dot{h}_s}{\rho} \qquad \textit{Conservation of energy,} \qquad (3)$$

$$\frac{D\vec{v}}{Dt} = -\frac{1}{\rho}\nabla P + \mu \nabla^2 \vec{v} + \vec{g}[1 - \beta(T - T_m)] + \frac{\dot{\vec{p}}_s}{\rho} \qquad \textit{Conservation of momentum.} \qquad (4)$$

Time-varying shape and location of fluid-void boundary can be obtained by simultaneously solving the conservation equations. The fluid is assumed to be incompressible and Newtonian with laminar flow. ρ is fluid density, t is time, $\vec{v}$ is molten metal velocity, $\dot{m}_s$ is source term representing the mass addition rate of filler metal droplets that are captured in the molten pool, h is enthalpy, σ is thermal conductivity $\dot{h}_s$ is a source term representing enthalpy addition rate associated with captured filler material droplets, P is hydrodynamic pressure, μ is viscosity, g is gravitational acceleration in z direction, β is constant of thermal expansion, T_m is melting temperature, and $\vec{p}_s$ is a source term representing the momentum addition rate corresponding to the captured filler material droplets.

$$\frac{\partial F}{\partial t} + \nabla \cdot (\vec{v}F) = \dot{F}_s \qquad \textit{Conservation of fluid volume fraction,} \qquad (5)$$

where F is volume fraction of fluid in a cell. Thus, the value of F only exists from F=0 (=void region) to F=1 (=entirely occupied region by fluid). $\dot{F}$ denotes the change in F associated with density of fluid and mass source rate.

For reasonably accurate description of the laser cladding process, several calibrations are made in this study. More details of the calibrations and approaches for the simulation were presented in a separate paper [6] so a brief summary is presented here. An approximation of laser energy absorptance was given by Hagen-Rubens relationship [27]. Absorptance is calculated from temperature-varying resistivity of the substrate and clad material (assumed to have the same composition)

$$A(T) = [8\varepsilon_0 \omega \rho_e]^{1/2} \qquad \text{Hagen-Rubens relationship,} \qquad (6)$$

where A is absorptance, ε_0 is permittivity of free space, ω is the angular frequency of laser radiation (1.75 X 10^{15} rad/s for fiber laser radiation with wavelength $\lambda = 1.07$ X 10^{-6} m), and ρ_e is electrical resistivity of substrate.

For laser cladding, it may be assumed that any particles which do not strike the molten pool can be considered to be lost. This is reasonable because powder particles which impinge on solid substrate are likely to be reflected and thus not contribute to formation of the clad deposit. Therefore, the powder catchment efficiency ϕ can be defined as a ratio between the area of molten pool S_m and area of substrate which is impinged by the powder jet, S_{jet} [26]

$$\varphi = S_m / S_{Jet}. \qquad (7)$$

3.2.2 Temperature gradient and solidification rate

Temperature gradient vector **G** is normal to solid-liquid interface of the weld pool and has components G_x, G_y and G_z. These components are obtained directly from the simulated 3D weld pool by differentiating temperature profile at the liquid interfaces. The laser beam travelling direction is parallel to the X-axis and substrate surface normal is along the Z-axis. Once the components G_x, G_y and G_z are obtained, the temperature gradient normal to the solidification front **G** can be calculated with the expression

$$|\boldsymbol{G}| = G = \sqrt{G_x^2 + G_y^2 + G_z^2}. \tag{8}$$

It is known that the solidification rate on the liquid side of the solid-liquid boundary strongly influences the scale of the weld microstructure [28]. For steady state conditions, the magnitude of the solidification rate (R) at any point on the solid-liquid interface is geometrically related to the laser scanning speed (R_b) and angle between the solidification boundary and the welding travel direction at the point of interest [29]. The solidification rate R can be calculated by

$$|\boldsymbol{R}| = R = |\boldsymbol{R}_b|\, cos\, \theta. \tag{9}$$

In equation (9), Ө is the angle between solid-liquid interface normal and beam travel direction. In a Cartesian coordinate system, cosθ can be expressed by $G_x/\sqrt{G_x^2 + G_y^2 + G_z^2}$ [30]. R is obtained at three different heights on the simulated weld pool solidification boundary spaced at 100 µm (see Figures 3.4 and 3.5). Note that R is zero (minimum) at the bottom and the outermost edge of the weld pool because the boundary normal is at an angle Ө = 90 degrees to the beam travel direction. R becomes same as R_b (maximum) at the trailing edge of the upper surface of the weld pool because its angle Ө is zero degrees to the travel direction.

3.2.3 Solidification Microstructure Models

Several theoretical models have been proposed to describe the dependency of size of microstructure on solidification conditions. The present work considered models proposed by Kurz-Fisher [31] and Trivedi [32], in which primary dendrite arm spacing (PDAS) of the dendritic solidification microstructure at various locations along the weld pool solidification boundary is predicted from the corresponding magnitudes of steady-state solidification temperature gradient G and solidification rate R. The Kurz-Fisher and Trivedi models are presented in equations (10) and (11), respectively [33,34]

$$\lambda_{PDAS} = 4.3\Delta T_n^{0.5}\left(\frac{D_L\Gamma}{\Delta T_0 k}\right)^{0.25} G^{-0.5}R^{-0.25} \qquad \textit{Kurz-Fisher,} \qquad (10)$$

$$\lambda_{PDAS} = 2.83(L\Delta T_0 k D_L \Gamma)^{0.25} G^{-0.5} R^{-0.25} \qquad \textit{Trivedi.} \qquad (11)$$

Here ΔT_n is the non-equilibrium solidification range for IN718, L is the constant of harmonic perturbation, D_L is the diffusion coefficient in liquid, Γ is Gibbs-Thomson coefficient, ΔT_0 is the equilibrium solidification temperature range, and k is the partition coefficient. The physical properties used in theoretical model are listed in Table 3.1.

Table 3.1 Physical properties of nickel based superalloy used in theoretical prediction

Property	Symbol	Value (units)	Ref.
Non-equilibrium solidification range	ΔT_n	200 (K)	35
Constant of harmonic perturbation	L	28	31
Diffusion coefficient in liquid	D_L	$3.0*10^{-9}$ (m^2/s)	36
Gibbs-Thomson coefficient	Γ	$1.0*10^{-7}$ (K·m)	36
Equilibrium solidification range	ΔT_0	105 (K)	37
Partition coefficient	k	0.48	36

3.3 Experimental

A single path, single layer clad track was formed by depositing IN718 powder on an IN718 substrate. The substrate thickness was 0.226 cm, the laser power used to build the clad layer was 550W, laser spot size was 1mm, the powder feed rate was 1.2 g/min and the travel speed was 1.016 cm/s. The deposit was cross-sectioned, metallographically prepared and photographed. PDAS was directly measured from an optical image taken from the center of the deposit using image processing software (ImageJ, NIH).

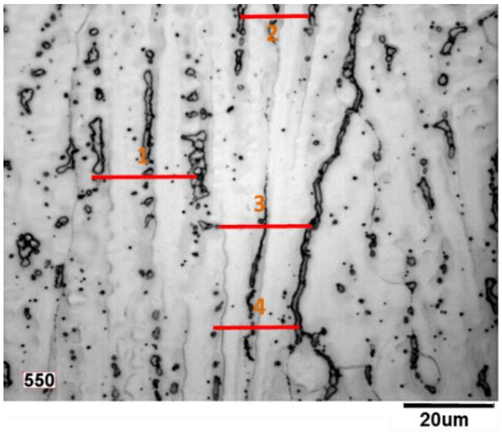

Region	DAS (um)
1	11.5
2	8.1
3	10.7
4	9.2
Mean	9.9

Figure 3.3 Measured primary dendrite arm spacing from a single layer clad deposit

PDAS was measured from an image of a cross section of a single track, single layer clad deposit as shown in Figure 3.3. The deposit width was 1.77 mm and deposit height was 100 µm. The predicted PDAS within the measurement area varied from 8.1 to 11.5 µm with a mean value of about 10 µm.

3.4 Numerical Model Results and Solidification Microstructure Prediction

In Figure 3.4, the weld pool solidification rate R predicted by the numerical model is plotted in X-Y-Z plane with a simulated weld pool shaded gray. The 3D weld pool is analyzed at the three different height sections A, B and C separated by 100 µm. The magnitude of solidification rate is illustrated by colored points (note that dark red is the maximum and dark blue is minimum value). The maximum solidification rate R is found on the weld centerline (Y=0) whereas the minimum value is at the outermost lateral weld edge (Y=max. weld width). It is also observed that the solidification rate near the weld pool top surface is higher than near the weld pool bottom. Note that the solidification rate at the weld center seems to be nearly constant even though the height changes from level A to B. However, the solidification rate decreases significantly from height B to C. In other words, the solidification rate maintains the travel speed of the beam at heights A and B whereas it decreases at height C. This can be explained by the fact that the angle θ is relatively small at both heights A and B at the weld center. The angle only varies by 9 degree from 17^{o} to 8^{o} between height A and B while it varies by 43 degree from 8^{o} to 51^{o} between height B and C. Notice that there is no significant change of θ seen at the weld edge. This is because θ is nearly 90^{o} for this area of the boundary. These observations reinforce the fact that variation of solidification rate at locations on the solidification boundary is significantly affected by the shape of weld pool.

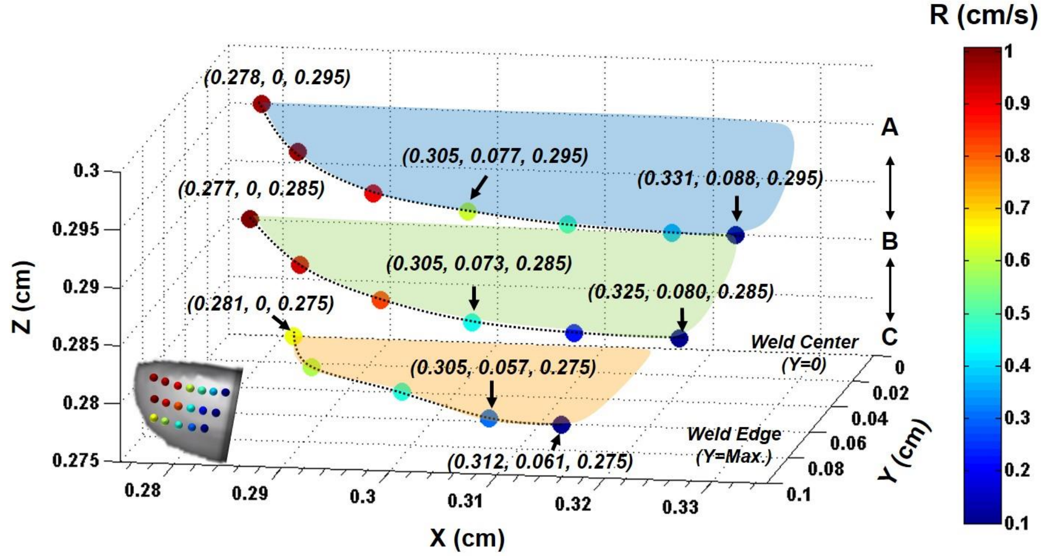

Figure 3.4 Solidification rate R calculated on the weld pool solidification boundary. The small inset graphic on the lower left shows the location of the points on a 3-D graphic of the solidification boundary at the rear edge of the weld pool (due to half-symmetry, only ½ of the solidification boundary is shown).

The magnitude of the temperature gradient G at locations along the three dimensional weld pool boundary are depicted in Figure 3.5. The temperature gradient increases when traversing from the weld center to the outermost pool edge at z heights near the bottom of the weld pool whereas it decreases as the top surface and weld center are approached. The magnitudes of G are minimum (3.15x10^3 K/cm) at the center of the top surface of the weld pool and maximum (1.38x10^4 K/cm) at weld pool edge at the intermediate depth. It is seen that the magnitudes of temperature gradient G and solidification rate R vary inversely along the solidification boundary.

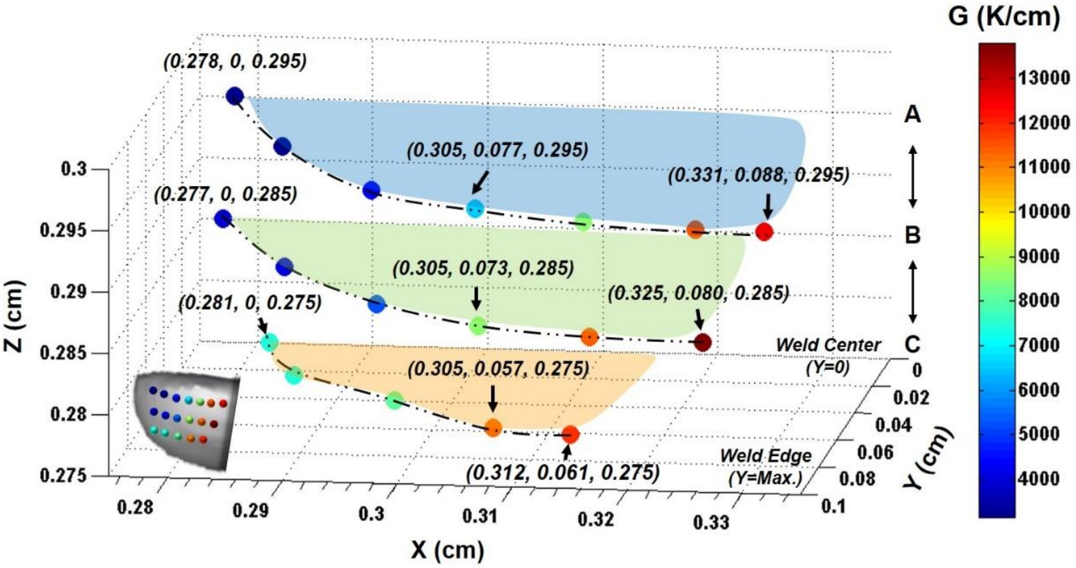

Figure 3.5 Temperature gradient G calculated on the weld pool boundary

The cooling rate on the liquid side of the solidification boundary dT/dt = |G|·|R| is calculated to examine the effect of this value on the predicted size of solidification structure. The maximum cooling rate (dT/dt = 4.7x10^3 K/s) is seen at the weld center of height C whereas the minimum value (=1.25×10^3 K/s) is found at the outermost edge of height A. In general, the cooling rate is lower near the weld pool surface than near the bottom of the weld pool because Marangoni flow causes strong convective heat transfer to the outer edge of the weld pool in the vicinity of the surface [38] and this decreases cooling rate. In other words, maximum cooling rate should be found at the deepest region of the weld pool where the influence of fluid convection is less. Generally, cooling rate increases from the weld center to weld edge while it decreases from the weld bottom to weld surface. In Figure 3.6, this distinct pattern is observed from the calculated result. The magnitude of solidification boundary cooling rate increases with increasing depth and width, which is consistent with the general pattern. However, it is seen that the pattern is opposite in mixing zone. The values of cooling rate do not only decrease from upper to lower height but also from the weld center toward weld edge of the pool. It is assumed that strong convective flow generated near the weld edge of the weld pool alters temperature distribution as well as the cooling trend.

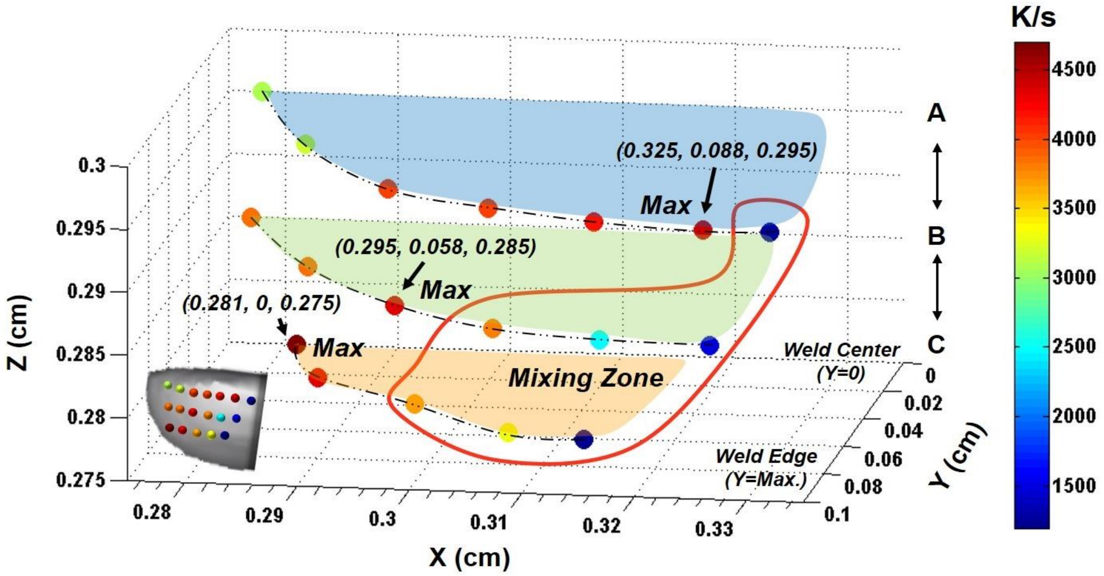

Figure 3.6 Cooling rate predicted by the product G R on the weld pool boundary. The cooling rate at height A increases as one traverses along the solidification boundary from the weld centerline toward the point of maximum weld, but then reaches maximum and suddenly decreases in a narrow region near the maximum pool width. At a deeper depth B, the cooling rate increases from when traversing along the solidification boundary from weld centerline but reaches a maximum and begins to decrease at point closer to the trailing edge than at depth A. At deepest depth C, the maximum cooling rate is at the weld centerline and cooling rate only decreases when traversing along the solidification boundary toward the maximum pool width.

To support the above analysis, the weld pool fluid flow pattern is presented in Figure 3.7. In prior publications discussed in the Introduction section, it is shown that surface tension gradient, which induces Marangoni convection, has a significant influence on fluid circulation pattern in the weld pool. Also, it is reported that a transition temperature in the surface tension depends on the concentration of sulfur, oxygen and other surface active elements in IN718 [15]. The transition temperature is calculated by numerical equation below [39]

$$\gamma = \gamma_o - K_s(T - T_r) - R_g T S_e \, ln\left[1 + a_m E exp^{-\left(\frac{\Delta H^O}{RT}\right)}\right]. \qquad (12)$$

Here γ_o is the surface tension in pure metal at reference temperature T_r, K_s is a surface tension coefficient, R_g is gas constant, S_e is surface excess at saturation, a_m is activity of species m in solution, E is entropy segregation constant and ΔH^0 is segregation in enthalpy. For the alloy used in the present study, equation (12), predicts that the transition occurs at 1801K, marked as T_i in the inset graphic in Figure 3.7. Surface tension gradient causes a strong backward surface flow from the center laser focus and a lower-velocity forward surface flow from the back pool edge. Downward fluid flow initiates in a region on the weld pool surface region having temperature T_i (indicated by a dashed blue line graphic) where the opposing surface fluid flows impinge and are directed downward. The downward fluid flow initiates at the top surface of the weld pool between X-axis locations 0.31 cm and 0.32 cm. It leads to strong downward flow and convective heat transfer in the mixing zone. As a result, the boundary cooling rate in the mixing zone becomes slower than outside of the zone. Also, the X-axis location of the maximum cooling rate shifts toward the rear of the weld pool as the depth increases from A to C.

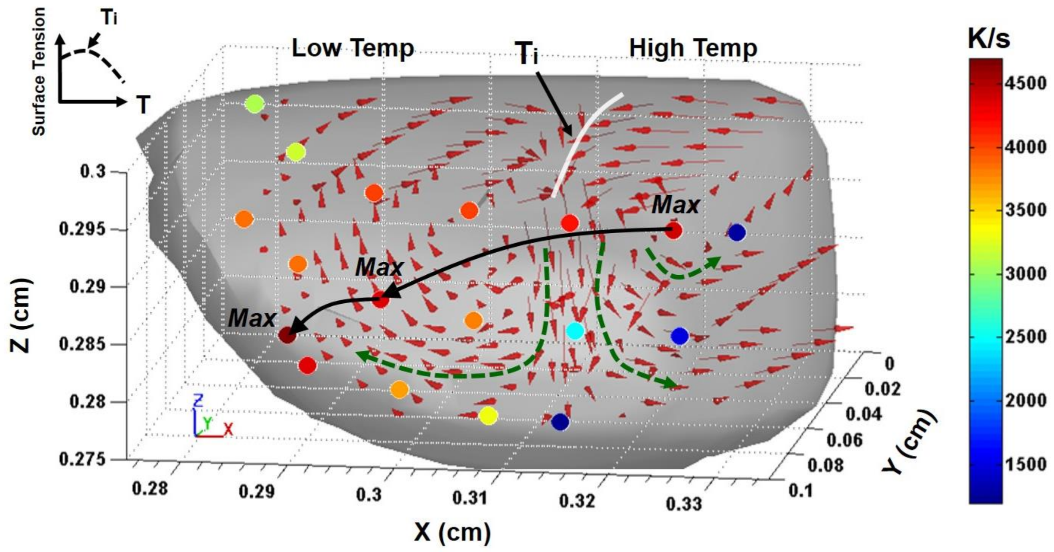

Figure 3.7 Solidification boundary cooling rate, location of maximum cooling rate and fluid flow pattern at heights A, B and C. Marangoni convection causes somewhat lower maximum boundary cooling rate near the point of widest pool width on the top surface of the weld pool (depth A). The maximum cooling is larger at depth C and its location shifts rearward towards the trailing weld pool edge. Red arrows: fluid flow direction in the weld pool liquid; Green dashed arrows: focus on fluid flow direction adjacent to solidification boundary that causes reversal in cooling rate, in the mixing zone; Black solid arrows: indicates a backward shift in maximum cooling rate to solidification boundary locations closer to the bottom and center of the weld pool.

The PDAS distribution predicted by Kurz-Fisher and Trivedi models with G and R values obtained from the single track, single layer clad cladding simulation are shown in Figure 3.8. The values from the Kurz-Fisher model are represented by the blue dotted line and values from the Trivedi model are plotted with the red solid line. Different heights correspond to green (height A), violet (height B) and red (height C) points. PDAS is predicted to increase near the outer weld edge which corresponds well to the trend of predicted cooling rate shown in Figure 3.6. Starting from the rear center of the weld pool and progressing forward along the weld pool boundary toward the weld edge, the cooling rate first increased and then decreased when entering the boundary region influenced by weld pool convection mixing zone. The cooling rate was lowest at the outermost edge of the weld pool. By comparing Figures 3.6 and 3.8, it can be seen that the predicted PDAS increases as the cooling rate decreases in the mixing zone. Thus, it can be concluded that the convective mixing in the weld pool alters solidification conditions (G and R) so as to retard cooling. Correspondingly, PDAS also increases near the weld edges. It is also noted that the PDAS values predicted by the Trivedi model are closer to the mean value of 9.9 µm (measured within a small region near the center of the clad deposit) shown in Figure 3.3.

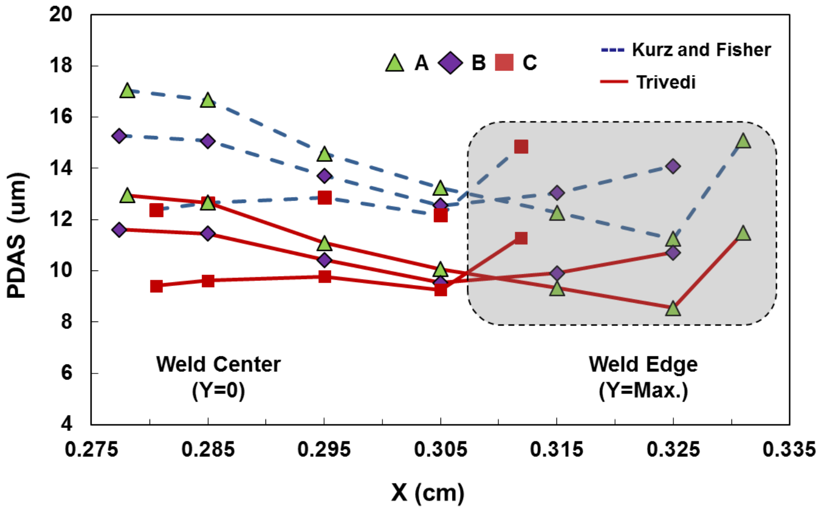

Figure 3.8 PDAS along weld pool solidification boundary predicted using Kurz-Fisher and Trivedi models at three Z-axis heights A, B and C, respectively. Weld center is at the middle of the back edge of the weld pool at Y=0 and X=0.275 and weld edge denotes the location of maximum weld width. The grey shaded area corresponds to solidification boundary located influenced by the weld pool convection mixing zone.

3.5. Summary and Conclusions

The numerical and theoretical calculations presented here provided insight into the effects of weld pool convection and shape on predicted solidification microstructure size in single layer, single track laser deposits. The melt pool solidification boundary temperature gradient G and solidification rate R normal to the pool solidification boundary were obtained from a transport simulation of IN718 clad deposits considering the effect of heat transfer, fluid flow, mass addition, and laser-powder-substrate interaction. Results showed that R near to the weld centerline was approximately equal to the beam travel speed at locations near the top weld pool surface. However, a relatively sharp decrease in R was observed near the bottom of the weld pool due to a larger angle between the boundary normal and the weld travel vector. Similarly, near the outermost lateral edge weld pool (at its widest extent), the weld pool boundary normal vector was nearly normal to the travel vector at all depths so no significant change in solidification rate with depth was observed. The simulation results also predicted an inverse relationship between G and R at all locations on the solidification boundary. These simulation predictions of G and R were used in relationships reported in previous research literature to predict the primary dendrite arm spacing of the solidified clad deposit microstructure. The relationship of simulated weld pool convection patterns to predicted solidification boundary shape, cooling rate distribution and primary dendrite arm spacing was also examined. The simulated weld pool fluid flow pattern showed surface flow of cool melt forward from the rear of the pool, surface flow of hot melt backward from the front of the weld pool (under the laser heat source) and mixing of the two opposing flows in an intermediate region between. This mixing produced a solidification boundary cooling rate that decreased from top to bottom and from the rear center to the outermost lateral edge of the weld pool, inverse to the variation of predicted dendrite arm spacing. Future research will study multiple layer and multiple track clad deposits for more general insight into laser clad solidification microstructures.

3.6 Acknowledgements

The authors would like to thank Rolls-Royce Corporation for the funding support and providing laser cladding samples in this work. They also appreciate NSF-I/UCRC: Center for Integrative Materials Joining Science for Energy Applications. The authors express their thanks to J.S.Bader for helpful suggestions and interest in this project.

3.7 Nomenclature

ρ	fluid density (g/cm^3)
t	time (s)
$\vec{v}$	molten metal velocity (cm/s)
$\dot{m}_s$	mass source rate (g/s)
H	enthalpy (g cm^2/ s^2)
$\dot{h}_s$	enthalpy source rate (g/s^3)
σ	thermal conductivity (g-cm/s^3/K)
P	hydrodynamic pressure (g/cm/s^2)

μ	viscosity (g/cm/s)
g	gravitational acceleration (m/s^2)
β	constant of thermal expansion (K^{-1})
T_m	melting temperature (K)
$\vec{p}_s$	momentum source rate (g/cm^2 s^2)
F	volume fraction of fluid in a cell (0 to 1)
$\dot{F}$	change in F
A	absorptance
ε_0	permittivity of free space (F/m)
ω	angular frequency of laser radiation (rad/s)
ρ_e	electrical resistivity (Ω·cm)
ϕ	powder catchment efficiency, ratio of S_m and S_{jet}
S_m	area of molten pool (cm^2)
S_{jet}	area of substrate struck by powder jet (cm^2)
γ_o	surface tension in pure metal (g/s^2)
T_r	reference temperature (K)
K_s	surface tension temperature coefficient (g/s^2 K)
R_g	gas constant (g cm^2/s^2 mol K)
S_e	surface excess at saturation (g·mol/cm^2)
a_m	activity of species m in solution
E	entropy segregation constant
ΔH^0	segregation in enthalpy (kJ/kg·mol)
T_i	surface tension transition temperature (K)
T	temperature (K)
ΔT	undercooling (K)
ΔT_S	solidus and liquidus temperature difference (K)
ΔT_n	non-equilibrium solidification range (K)
ΔT_0	equilibrium solidification range (K)
G	three dimensional temperature gradient normal to solid-liquid interface (K/cm)

G_L	temperature gradient in liquid region (K/cm)
G_x	x-component of G
G_y	y-component of G
G_z	z-component of G
R	solidification rate at solid-liquid interface (cm/s)
R_b	laser beam travel speed (cm/s)
Θ	angle between solid-liquid interface normal and beam travel direction (deg)
L	constant of harmonic perturbation
D_L	diffusion coefficient in liquid region (m^2/s)
Γ	Gibbs-Thomson coefficient (K·m)
K	partition coefficient

3.8 References

1. Gregory OJ, Amani M, Tougas IM, Drehman AJ (2012) Stability and microstructure of indium tin oxynitride thin films. Journal of the American Ceramic Society 95(2):705-710.

2. Borel MO, Nicoll AR, Schlapfer HW, Schmid RK (1989) The wear mechanisms occurring in abradable seals of gas turbines. Surface and Coatings Technology 39–40(0):117-126.

3. Anderson TD, DuPont JN, DebRoy T (2010) Stray grain formation in welds of single-crystal ni-base superalloy cmsx-4. Metallurgical and Materials Transactions A 41(1):181-193.

4. Zhong M, Liu W (2010) Laser surface cladding: The state of the art and challenges. Journal of Mechanical Engineering Science 224(C5):1041-1060.

5. Majumdar JD, Manna I (2013) Laser-assisted fabrication of materials, vol 161. Direct laser cladding , current status and future scope of application. Springer, New York

6. Lee YS, Nordin M, Babu SS, Farson DF (2014) Influence of fluid convection on weld pool formation in laser cladding. Welding Journal 93(8):292S-300S.

7. DuPont J, Babu S, Liu S (2013) Welding of materials for energy applications. Metallurgical and Materials Transactions A 44(7):3385-3410.

8. Heiple CR, Roper JR (1982) Mechanism for minor element effect on gta fusion zone geometry. Welding Journal 61(4):S97-S102.

9. Heiple CR, Roper JR, Stagner RT, Aden RJ (1983) Surface-active element effects on the shape of gta, laser, and electron-beam welds. Welding Journal 62(3):S72-S77.

10. Chan C, Mazumder J, Chen MM (1983) A two-dimensional transient model for convection in laser melted pool. Journal of Metals 35(12):49.

11. Kou S, Wang YH (1986) Three-dimensional convection in laser melted pools. Metallurgical and Materials Transactions A 17(12):2265-2270.

12. Kou S (2012) Fluid flow and solidification in welding: Three decades of fundamental research at the university of wisconsin. Welding Journal 91(11):287S-302S.

13. Mills KC, Keene BJ, Brooks RF, Shirali A (1998) Marangoni effects in welding. Philosophical Transactions of the Royal Society, A:911-926.

14. Sahoo P, Debroy T, Mcnallan MJ (1988) Surface tension of binary metal-surface active solute systems under conditions relevant to welding metallurgy. Metallurgical and Materials Transactions B 19B(3):483-491.

15. Lee PD, Quested PN, McLean M (1998) Modelling of marangoni effects in electron beam melting. Philosophical transactions of the Royal Society 356(1739):1027-1043.

16. Su Y, Mills KC (2005) A model to calculate surface tension of commercial alloys. Journal of Materials Science 40(9-10):2185-2190.

17. Zhao Y, Shi Y, Lei Y (2006) The study of surface-active element oxygen on flow patterns and penetration in a-tig welding. Metallurgical and Materials Transactions B 37(3):485-493.

18. Zhao CX, Kwakernaak C, Pan Y, Richardson IM, Saldi Z, Kenjeres S, Kleijn CR (2010) The effect of oxygen on transitional marangoni flow in laser spot welding. Acta Materialia 58(19):6345-6357.

19. David SA, Babu SS, Vitek JM (2003) Welding: Solidification and microstructure. JOM 55(6):14-20.

20. Kou S (2003) Welding metallurgy. 2nd edn. John Wiley & Sons, New Jersey

21. DebRoy T, David SA (1995) Physical processes in fusion welding. Reviews of Modern Physics 67(1):85-112.

22. Hunt JD (1984) Steady state columnar and equiaxed growth of dendrites and eutectic. Materials Science and Engineering 65(1):75-83.

23. Anderson TD, DuPont JN, DebRoy T (2010) Origin of stray grain formation in single-crystal superalloy weld pools from heat transfer and fluid flow modeling. Acta Materialia 58(4):1441-1454.

24. Gaumann M, Bezencon C, Canalis P, Kurz W (2001) Single-crystal laser deposition of superalloys: Processing-microstructure maps. Acta Materialia 49(6):1051-1062.

25. Gao Z, Ojo OA (2012) Modeling analysis of hybrid laser-arc welding of single-crystal nickel-base superalloys. Acta Materialia 60(6–7):3153-3167.

26. Picasso M, Marsden CF, Wagniere JD, Frenk A, Rappaz M (1994) A simple but realistic model for laser cladding. Metallurgical and Materials Transactions B 25(2):281-291.

27. J. Xie, A. Kart, Rothenflue JA, Latham WP (1997) Temperature-dependent absorptivity and cutting capability of CO_2 , Nd:YAG and chemical oxygen iodine lasers. Journal of Laser Applications 9:77-85.

28. David S, Vitek J (1989) Correlation between solidification parameters and weld microstructures. International Materials Reviews 34(1):213-245.

29. Rappaz M, David SA, Vitek JM, Boatner LA (1989) Development of microstructures in Fe-15Ni-15Cr single crystal electron beam welds. Metallurgical and Materials Transactions A 20(6):1125-1138.

30. Vitek JM (2005) The effect of welding conditions on stray grain formation in single crystal welds - theoretical analysis. Acta Materialia 53(1):53-67.

31. Kurz W, Fisher DJ (1981) Dendrite growth at the limit of stability: Tip radius and spacing. Acta Metallurgica 29(1):11-20.

32. Trivedi R (1984) Interdendritic spacing: Part ii. A comparison of theory and experiment. Metallurgical and Materials Transactions A 15(6):977-982.

33. Spinellia JE, Rochab OFL, Garciaa A (2006) The influence of melt convection on dendritic spacing of downward unsteady-state directionally solidified sn-pb alloys. Materials Research Bulletin 9(1):51-57.

34. Gao S, Liu L, Xu Y, Yang C, Zhang J, Fu H (2012) Influences of processing parameters on microstructure during investment casting of nickel-base single crystal superalloy DD3. China Foundry 9(2):159-164.

35. Lewandowski MS, Overfelt RA (1999) High temperature deformation behavior of solid and semi-solid alloy 718. Acta Materialia 47(18):4695-4710.

36. Wang W, Lee PD, McLean M (2003) A model of solidification microstructures in nickel-based superalloys: Predicting primary dendrite spacing selection. Acta Materialia 51(10):2971-2987.

37. Overfelt RA, Taylor RE (1996) Thermophysical property measurements for casting process simulation. Thermal Conduct 23:538-552.

38. Kovacevic R (2012) Welding processes. InTech, Rijeka, Croatia

39. Zacharia T, David SA, Vitek JM, Debroy T (1989) Weld pool development during gta and laser beam welding of type 304 stainless steel, part I. Welding Journal 68:S499-S509.

Chapter 4: Simulation of Transport Phenomena and Melt Pool Shape for Multiple Layer Additive Manufacturing

4.1 Introduction

Laser additive manufacturing (LAM) is a rapidly emerging fabrication process with significant potential to reduce manufacturing cost, energy consumption and environmental impact [1]. However, the commercial acceptance of LAM process still facing a technical challenge caused by the limited understanding of physical phenomena in the melt pool [2]. Real time observation of the physical phenomena is very difficult since LAM melt pools are inherently transient and involve complex laser-powder-substrate physical interactions. Moreover, the real-time measurements of thermal and fluid variables can typically be made only on the surface of the melt pool. In contrast, a numerical simulation of mass, momentum and energy transfer in LAM melt pools can provide three-dimensional (3-D) distributions of temperature, flow velocities, melt pool shape, and solidification temperature gradient (G) and solidification rate (R).

Many numerical simulations of laser welding and other conventional fusion welding processes have been described [3-5] but unfortunately, many of the previous numerical simulations that focus on fusion welding do not consider the unique characteristics of the LAM process [6]. As layer-by-layer deposition progresses, previously deposited layers undergo multiple thermal cycles resulting in repeated heating, remelting and cooling. Moreover, the laser beam is imposed on the free surface of the previous layer, which may not be initially flat as is commonly assumed in laser welding simulation. The melt convection occurs in a melt pool with a convex surface due to particle addition and surface tension forces. The laser-powder-substrate interaction is an additional factor that must be accommodated in LAM simulations. Owing to the differences between LAM and other fusion processes, there is still a need for more effort to develop transport simulations of LAM melt pools to provide better understanding of the melt pool temperature and flow distributions and the pool shape. Furthermore, prediction of melt pool free surface and 3-D shape of the solidified deposit are also required for better accuracy of multi-layer LAM simulation. However, only limited studies have been reported in the transient heat transfer and fluid flow simulation of multiple layer LAM [7]. Previous models have used pre-defined deposit geometry to avoid the complexity of free-surface transport simulation that is necessary to calculate it directly. For instance, flat-top melt pool surface has been assumed in some prior investigations [6,8] or a pre-defined rectangular geometry was converted to curved shape via a fitting algorithm [9]. Thus, more accurate melt pool shape prediction (especially, melt pool top surface) is needed because laser beam and powder particles are applied on the top free surface, Moreover, remelting behavior could vary with the shape of the top surface.

Several 2-D and 3-D numerical simulations have been reported to study temperature distribution, fluid flow, powder injection and free surface evolution during

LAM process. The previous studies are mostly limited to one [10] or two layers [11] or to 2-D simulations [12,13] for more than three layers. Recent reports of 3-D simulations for multiple layer LAM study melt temperature profile and fluid velocity field. Solidification parameters (G and R) were used to estimate dendrite cell spacing and hardness in three layer deposits [6,14]. In these simulations, the top surface of each layer is assumed as flat. An improved mass addition model based on enthalpy balance has been reported for 2-D multiple layer LAM simulation based on finite element method (FEM) [7]. It calculates temperature profile and uses it to estimate melt pool track width and height.

Previous literature mentioned above predicted deposit geometry, melt pool peak temperature and fluid flow and solidification parameters G and R using comprehensive three-dimensional (3-D) transport simulations. Yet, in all of this research, the effect of convective flow on the shape of melt pool fusion boundary and the solidified deposit were not investigated for LAM. It is known that solidification parameters G and R are correlated to solidification morphology (via the ratio G/R) and microstructure size (via the product GR). These solidification parameters both vary considerably with position on the melt pool solidification boundary [15]. The melt pool fusion boundary shape is typically concave but in some cases, flat and convex “wavy” shapes have been reported for laser and arc welding [10,16-18]. Therefore, there are advantages to the use of a 3-D transport simulation to predict conditions on the fusion boundary in LAM.

This research uses a 3-D transport simulation to predict the size, shape and temperature and fluid flow distributions of melt pools formed during single-track multiple layer LAM of thin nickel alloy walls. These parameters are combined into dimensionless numbers and their correlation to variations in melt pool boundary shape for different layers of the LAM structure is studied. Hence, it seeks new insights into the LAM process based on correlations between melt pool conditions and boundary shapes.

4.2 Physical model

4.2.1 Fundamental equations

During the laser additive manufacturing, laser-heated powder is continuously added to a melt pool. The associated additions of mass, energy and momentum to the melt pool increase its size and alter its temperature and fluid flow distributions. Solutions to equations that describe conservation of mass, energy and momentum in the melt pool and the constitutive equation that describe the material response to process inputs are obtained by explicit numerical integration. Supplementing the 3 basic conservation laws with a 4th volume of fluid (VOF) equation describing conservation of fluid volume in the simulation grid allows calculation of the transient 3-D location of the void-fluid interface shape and hence the shape of the fluid free surface. The commercial software Flow3D (Flow Science, Inc.) is used to solve the equations. The fundamental fluid volume conservation equations, constitutive equations and more details of the modeling of process heat and mass inputs are given in a recent paper by the authors [19].

4.2.2 Boundary conditions

The computational domain has dimensions of 2.8 cm, 1.5 cm and 0.9 cm in the X, Y and Z directions, respectively. The Z direction has 0.5 cm of substrate and 0.4 cm of void region. The domain mesh is divided into two blocks to reduce computational load. The lower block from Z = 0 cm to 0.4 cm has 26,600 cells with edge length 400 μm and the upper block from Z = 0.4 cm to 0.9 cm has 262,500 cubic cells with edge length 200 μm. These cell sizes are selected to optimize mesh size independence of simulation results. For the bottom surface of the substrate, continuous heat flow boundary conditions are defined to model a semi-infinite domain. The other lateral edges are assumed as solid walls to describe a solid substrate. A convection coefficient of 25 W m^{-2} is applied to the top and side surfaces to model convection heat loss by helium shielding gas.

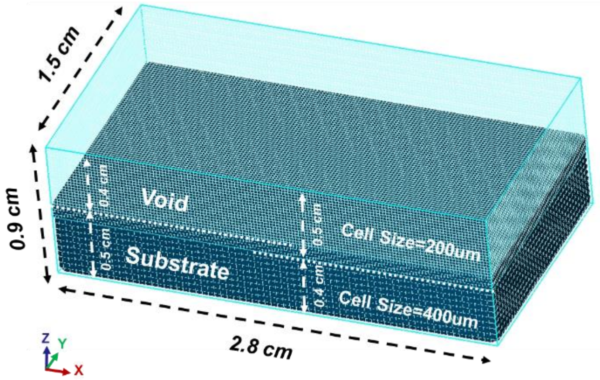

Figure 4.1 Initial setting of computational domain

At the beginning of the simulation, only solid, room temperature substrate exists with void in the upper region of the computation domain. A deposit layer is formed on the flat substrate by moving heat and mass flux sources applied just above the top surface of the substrate. The 700 W laser heat source with flat-top distribution is applied using a custom FORTRAN code. The powder particles entering the melt pool surface are assumed to be at liquidus temperature (1609 K) and the increased enthalpy is included in the heat input calculations as described below. Constant values of specific heat and conductivity but different values for liquid and solid are assumed in present model. Temperature dependent density, thermal conductivity and viscosity and other constant thermophysical properties of IN718 materials and process parameters are listed in Table 4.1.

Table 4.1 Thermophysical properties of IN718 powder and substrate and process parameters used in this simulation

Property	Value (units)	Reference
Laser Scanning Speed	1.083 cm s^{-1}	[20]
Power of Laser Beam	700 W	[20]
Beam Spot Size	1.95 mm	[20]
Powder Feed Rate	7 g min^{-1}	[20]
Idle time between passes	Continuous	[20]
Liquidus	1609 K	[20]
Solidus	1533 K	[20]
Latent Heat	2.27e+09 cm^2 s^{-2}	[21]
Viscosity	0.196*exp(5848/T) mPa	[22]
Density of Liquid	[7400-0.88 (T-1609)]/1000 g cm^{-3}	[22]
Density of Solid	[8190 - 0.392 (T-298)]/1000 g cm^{-3}	[22]
Surface Tension	1842 dyne cm^{-1}	[22]
Surface Tension Gradient	-0.11 dyne cm^{-1}K^{-1}	[22]
Specific Heat of Liquid	7.25e+06 cm^2 s^{-2}K^{-1}	[22]
Specific Heat of Solid	5.77e+06 cm^2 s^{-2}K^{-1}	[22]
Conductivity of Liquid	2.928e+06 gcm s^{-3}K^{-1}	[22]
Conductivity of Solid	2.792e+06 gcm s^{-3}K^{-1}	[22]

Experiments and simulations described in previous literature have investigated the sensitivity of melt pool geometry and peak temperature to variations in laser power, feed rate and laser scanning speed [11-14]. However, there has been little investigation of the sensitivity of these melt pool characteristics to uncertainties in the values of physical properties associated with fluid flow. In particular, the variation of surface tension with temperature is the main force that induces LAM melt pool fluid flow, but surface tension gradient is easily varied by small changes in the concentration of surface active elements such as sulfur in the powder or oxygen in the deposition chamber gas atmosphere. This sensitivity is investigated by comparing simulated height and width of 5th layer deposits produced using three different assumptions of melt pool surface tension gradient. The negative and positive gradients are -0.11 and +0.11 dyne $cm^{-1}K^{-1}$, respectively. The mixed gradient has transition from positive to negative at a temperature of 1801K due to surface active elements (ex. sulfur or oxygen). More details of the mixed gradient calculation are presented in a prior paper [19].

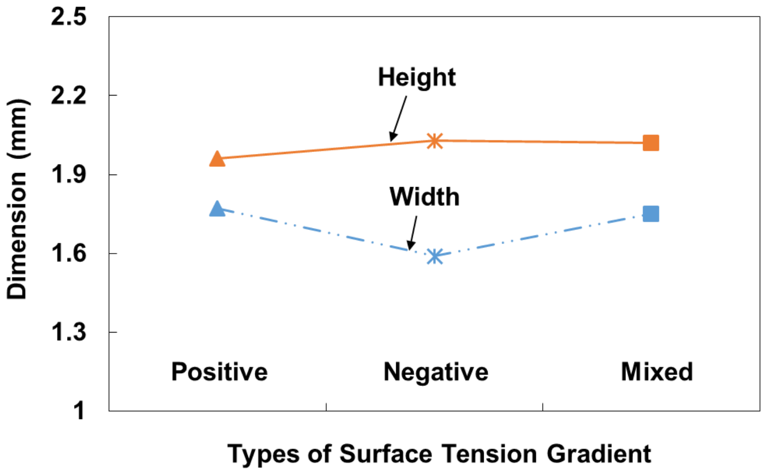

Figure 4.2 Variation of width and height of the 5 layer deposit with change of surface tension gradient from positive to negative to mixed

Figure 4.2 shows that the variation of surface tension gradient assumption causes some changes in predicted deposit geometry. The deposit height increases and width decreases when assumed gradient changes from positive to negative. These results suggest that control of deposit geometry by manipulating surface tension gradient may be feasible. Confirmation of this will require further research.

4.2.3 Process heat and mass transfer efficiencies

The laser beam power incident on the substrate is attenuated by absorption, radiation, convection and reflection as it passes through the powder particle cloud. However, laser power absorbed by the particles is returned to the melt pool by particles that are captured in it. Also, laser power is lost by direct reflection from the melt pool and substrate surface. Therefore, the laser power attenuation and absorption by the powder cloud and melt pool absorptance should be carefully considered for accurate modeling of the LAM experiments.

The temperature increase ΔT of a powder particle during flight through a laser beam depends on interaction time of the particle and the laser beam, particle size, carrier gas velocity, laser power and material properties of particles. Eq. 1 expresses the energy increase of a particle as [6]

$$\Delta T = \frac{\eta_I \eta_s \frac{P}{\pi r_b^2} 2\pi r_p^2 \tau}{\frac{4}{3}\pi r_p^3 C_p \rho_p} \tag{1}$$

where r_p is the powder particle radius, C_p and ρ_p are the specific heat and particle density, ΔT is the temperature rise during flight of the particle, η_I is an interference factor considering the shadowing of particle by other particles in the jet, η_s is absorptance of the particle, P is the laser beam power, r_b is beam spot radius and τ is particle interaction time with laser beam. The values of the variables are given in Tables 4.1 and 4.2. The calculated temperature rise is $\Delta T = 1336K$. Thus, the initial temperature of powder particles entering the melt pool is 1634 K. This slightly above the IN718 liquidus temperature of 1609 K.

Table 4.2 Parameters used for heat balance calculation

Property	**Value (units)**
Particle velocity	2.5 m s^{-1}
Interaction distance	2 mm
Interaction time, τ	0.8 ms
Interference factor, η_I	1
Average particle diameter, r_p	35 μm
Absorptance of solid particle, η_s	0.4

The portion of laser power that is contained in a jet of heated powder particles η_p can be expressed as [14]

$$\eta_p = \frac{C_p \dot{m} \Delta T}{P} \tag{2}$$

where $\dot{m}$ is powder feed rate and other variables are defined in Table 4.1. The calculation reveals that approximately 13% of incident beam power is absorbed by the particles and used to melt them. For LAM, the experimental literature [23] reveals that powder feed rate, powder composition and particle size has no effect on laser energy transfer efficiency, which is the ratio of energy absorbed by the workpiece and energy created by incident laser beam. Therefore, the Nd:YAG laser absorptance for IN718 substrate is predicted by the Hagen-Rubens [24] relationship: absorptance of 35% at the solidus temperature (1533 K) and 43% at the liquidus temperature (1609 K). This value is comparable to a reported measurement of IN718 absorptance 36% at solidus temperature [25]. In this simulation, the melt pool absorptance is set as 40%.

It may be assumed for LAM that only particles which impinge on molten area of melt pool can contribute to formation of the deposit layer. In prior LAM research reports, the overlap ratio of melt pool area and powder jet area is defined as catchment efficiency η_c. In two prior simulations, the melt pool is assumed to be approximately circular so the melt pool area can be calculated from melt pool width [7,19]. In another prior multilayer LAM simulation investigation similar to the present work, catchment efficiency has been assumed constant for all layers [12]. In the present simulation case of single-track multi-layer LAM, the assumption of a constant value of catchment efficiency is a taken as reasonable first approximation that will not change the overall trends of the correlations of flow and convection heat transfer and melt pool boundary shape. Also, although the melt pool area (and hence catchment efficiency) does increase somewhat as more layers are added and deposit height increases, the melt pool width is nearly constant due to the restricted width of the thin wall.

By conservation of mass between the powder jet mass flow rate and measurements of the dimensions of a single-layer LAM deposit, the catchment efficiency can be calculated as [26]

$$\eta_c = \frac{\rho_p \beta V_l h w}{\dot{m}} \tag{3}$$

where V_l is laser scanning speed, β is shape factor, h is deposit height and w is deposit width. β is approximately 2/3 since the deposit layer does not fully occupy the full rectangular box volume. In this simulation, an initial value of catchment efficiency estimated from experimental measurement of height and width of a single-layer LAM deposit made with the same process parameters as used for the simulation. Based on measurements, the catchment efficiency is 0.47.

4.3 Results and discussion

The 3-D illustrations displayed in Figure 4.3 depict the numerically-computed deposit geometry and melt pool for 5 successive layers in three dimensions. The beam travels from left to right for odd numbered deposit layers and it returns immediately in the opposite direction for the even-numbered layers. The red colored region represents temperatures above the liquidus temperature of IN718.

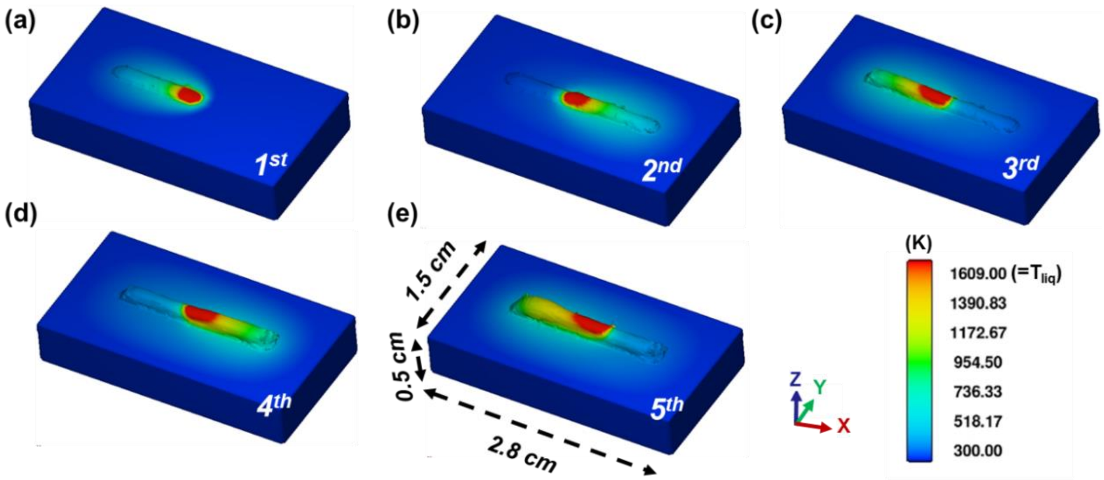

Figure 4.3 Simulation results showing melt pool at the midpoint of five deposition layers: (a) first layer, (b) second layer, (c) third layer, (d) fourth layer, and (e) fifth layer

Figure 4.4 shows the calculated time variation of temperature with at the mid-length, mid-center surface point on each of five successive deposit layers. The first peak occurs when the laser beam passes over the mid-length, mid-center point on the surface of the first layer. As the second layer is added, the first layer is heated again. Hence, there is second peak in the first thermal cycle and a higher first peak in the second thermal cycle. This process is repeated during deposition of subsequent layers, so there are total of 5 peaks in the first thermal cycle, 4 peaks in the second thermal cycle and so on. Generally, conduction heat transfer from the top surface of the deposit down to the substrate surface decreases with increased number of deposit layers (i.e. increased deposit height). Conduction is decreased at larger heights because the narrow deposit width reduces area for conduction and because the average temperature of the deposit increases, decreasing the temperature gradient for conduction. The predicted peak temperatures increase with each additional layer (peak temperatures are 2016 K, 2036 K, 2048 K, 2058 K and 2071 K in the first, second, third, fourth and fifth layers, respectively) due to this average deposit temperature increase.

Mid-length cross sectional profiles of the deposit after deposition of each of the five layers are superimposed in Figure 4.5a to illustrate the evolution of the build profile. This graphic clearly shows that the top of each layer has a circular profile, the radius of which decreases with increasing layer number. These results suggest that the surface shape of the previous deposit layer has a significant effect on the surface contour of the next deposition layer. This effect is discussed further below. Figure 4.5b shows the superimposed fusion boundaries of the melt pools produced during deposition of each layer. This graphic shows that the depth of remelting of each layer caused by deposition of the succeeding layer increases with deposit height. This occurs because the z-axis temperature gradient at the top surface of the deposit becomes smaller with each additional deposit layer (c.f. Figure 4.4), reducing conduction heat transfer through the deposit during deposition of upper layers. In addition, as more layers are added on the single track deposit, the heat transfer mode becomes highly two-dimensional of X and Z direction from three dimensional of X, Y and Z [27,28].

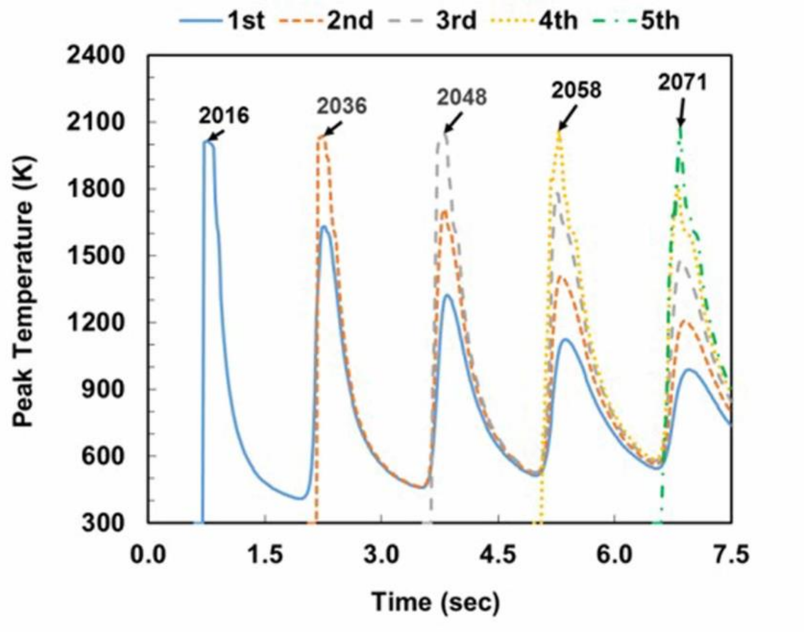

Figure 4.4 Thermal cycles at a mid-length, mid-width point on the deposit surface for five layers

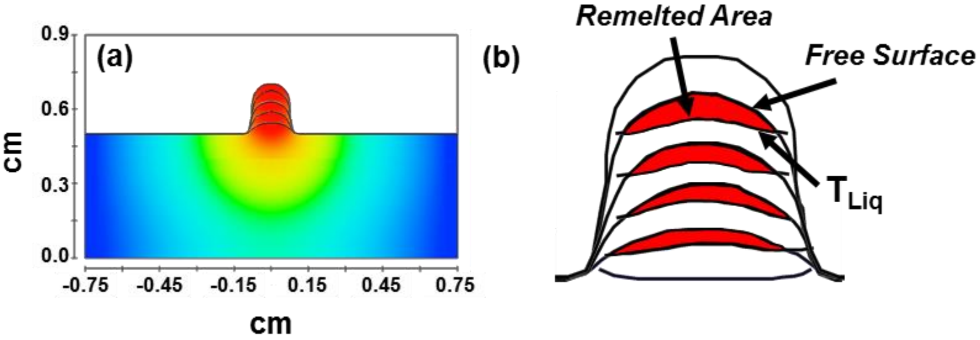

Figure 4.5 Build profile and evolution shown by overlapped profiles from the mid-length of a five-layer deposit: (a) cross section and (b) profile, fusion boundary and remelting of successive layers

For validation of the simulation results, height, width and peak temperature at the mid-length, mid-width point of each deposit layer are compared to experimental values from literature [20]. In the cited article, the deposit height and width at the fifth and tenth layers are graphed for several inter-layer idle times (continuous, 5 s, 20 s and 3600 s). As shown in Figure 4.6a, the predicted height and width of the five-layer deposit in the present work agree reasonably well with these experimental values. The prediction errors are 11.9% and 11.6% of the experimental height and width, respectively. Figure 4.6b compares predicted peak melt pool temperature to experimental peak melt pool temperature. In the cited reference, the temperature was measured with a two color pyrometer (Impac IGAR 12-LO MB22) using thermal radiation emitted from the melt pool surface in adjacent wavelengths of 1.28 μm and 1.65 μm at the mid-length mid-width point of each layer. The pyrometer optics included a filter to block 1.06 μm radiation to prevent measurement errors due to Nd: YAG laser beam reflections. The maximum prediction error is less than 2.5% of the measured temperatures. For comparison, accuracy and reliability of simulations similar to the present one are also available in literature. Deposit width prediction errors found by Pinkerton and Li [29] were 12% and 17% for 316L and H13, respectively. The deposit height prediction error reported by Alimardani were 9.29% for 304L stainless steel and 23% AISI 4340 steel [9] in height. Recently, prediction errors of 12% in height and 20% in width for a double layer deposit were reported by Liu and Qi [11].

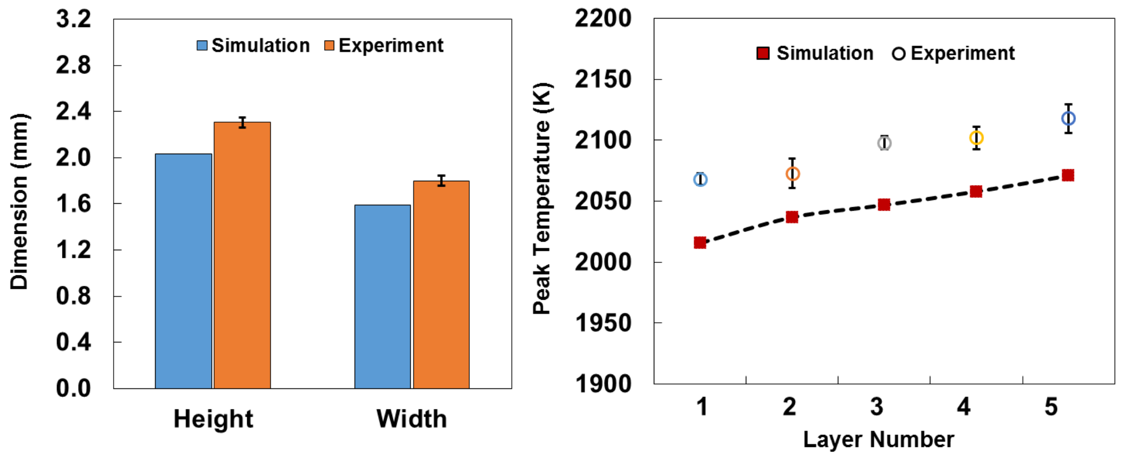

Figure 4.6 Comparison of simulation predictions and experimental measurements [20] at mid-length of a five-layer deposit: (a) height and width, (b) peak temperature for each layer

Figure 4.7 compares the shape of the bottom of the melt pool for each layer of a simulated five-layer deposit. Transverse cross-sections are taken at the mid-center of the deposit for each layer. The melt pools are defined by the liquidus isotherm and free surface fluid boundary. For the first layer deposition, the melt pool fusion boundary is flat. However, as the first three layers are added, the fusion boundary continually becomes more convex. In other words, the melt pool becomes deeper near the edges and as more layers are deposited. This melt pool convexity in LAM was shown in previous experimental literature and explained due to increase of temperature gradient in lateral direction causing stronger Marangoni flow [30]. However, it is clear from the simulation results that this convex melt pool bottom shape is also partly due to the fact that the top surface of the prior layer upon which the melt is being deposited is convex. An interesting point noted in the prior study [30] was that more convex molten pool shape improves surface finish quality.

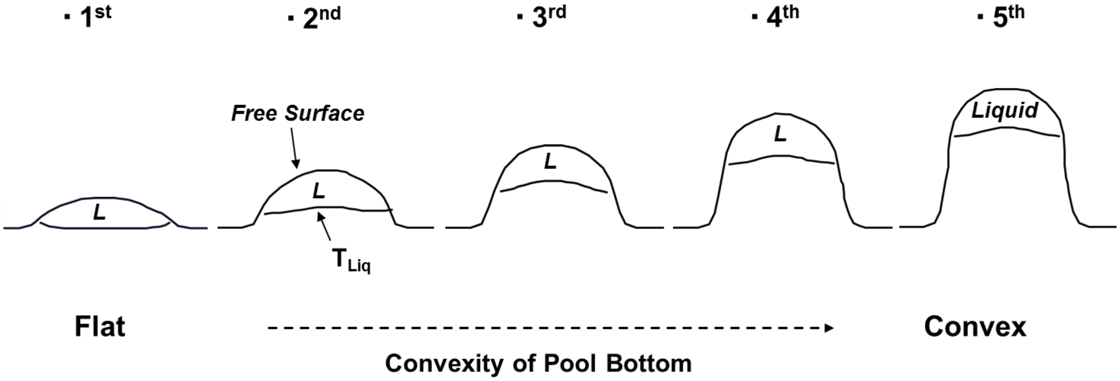

Figure 4.7 Progression of convexity at weld pool bottom through 1st to 5th layer in the transverse cross-sections at the mid-center of the deposit from each layer

The formation mechanism of the convex boundary in LAM seems to be more complex than the explanation in the previous literature [30] since heat and mass are initially deposited on the hemispherical free surface of the prior layer and fluid flows down along the curved surface. Figure 4.8 illustrates melt pool flows for laser welding on a flat surface and LAM. For laser welding of a metal with a negative surface tension gradient, Marangoni flow moves from the center to the edge. In LAM, the Marangoni flow is redirected downward along the curved fluid surface. Thus, in LAM the Marangoni flow is vertically downward when it impinges on and melts the previously deposited layer. In laser welding, the Marangoni flow melts the substrate laterally. Therefore, there are two distinct features of LAM that not only influence the melt pool flow pattern but also the shape of the fusion boundary. It is helpful to analyze these differences with the aid of dimensionless parameters.

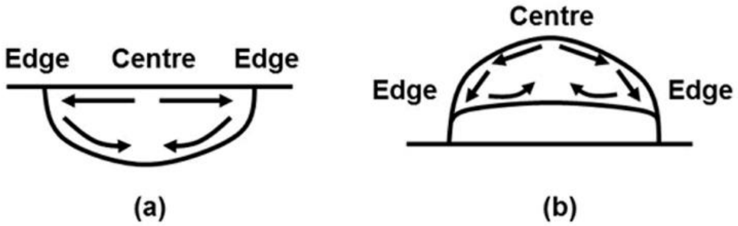

Figure 4.8 Comparison of fluid flow patterns in laser welding (a) and LAM (b)

During LAM, peak temperature continuously increases with layer number [20] and hence melt pool surface temperature gradient in the lateral direction becomes larger. As a consequence, Marangoni effect between the melt pool center and lateral edge becomes stronger. Since the magnitude of Marangoni shear stress gradient increases at higher layers, the layer-to-layer variation of fluid flow and heat transfer begins to significantly alter the shape of the pool fusion boundary at the upper layers.

Heat transfer in the molten pool occurs by coupled conduction and convection. Peclet number (Pe) calculates the ratio of convection heat transfer to conduction heat transfer and can be used to represent the relative influence of the two heat transfer mechanisms in determining melt pool shape.

$$\mathrm{Pe} = \frac{\mathrm{L V_{max} \rho C_p}}{\mathrm{k}}, \tag{4}$$

For this purpose, L is taken as a characteristic dimension of the melt pool (typically width), V_{max} is the maximum velocity of fluid flow in the pool, ρ is the density, C_P is the specific heat and k is the conductivity of the melt. Note that the characteristic width of the melt pool, L is not straight line in LAM (the free surface has a convex shape). Thus, L is measured along the convex free surface for each simulation layer in this study. V_{max} is obtained from the simulated fluid flow pattern at each simulation time step and averaged over the deposit length to obtain a characteristic value for each layer. The calculated values of Pe are 27.5 and 21.5 at first and fifth layer, respectively. The calculated Pe numbers for all layers are much greater than unity indicating the primary heat transfer mechanism in LAM melt pools is convection. Previous literature [16] showed that the shape of the fusion boundary changes from concave to convex when Pe changes from much less than unity in aluminum to much greater than unity in steel and stainless steel. However, Pe number alone is not enough to fully describe the effect of melt pool convection on the pool shape because it does not explicitly contain any process parameters [17].

Prior literature [18] has reported that the fluid flow patterns affecting the shape of the melt pool fusion boundary vary depending on Prandtl number (*Pr*; representing the ratio of momentum diffusion rate to thermal diffusion rate) and Marangoni number (Ma, representing the ratio of surface tension force to viscous force).

$$Pr = \frac{\mu C_p}{k}, \tag{2}$$

$$\mathrm{Ma} = \frac{\mathrm{L}\rho \frac{\mathrm{d}\gamma}{\mathrm{dT}} (\mathrm{T_p} - \mathrm{T_m}) \mathrm{C_p}}{\mu \mathrm{k}}, \tag{3}$$

Here, μ is the viscosity of liquid metal, dϒ/dT is the surface tension temperature coefficient, and T_p and T_m are the peak and melting temperature, respectively. Although Pr influences the pool shape, the temperature variation of Pr in a material is not large enough to determine melt pool shape by itself. In the IN718 material simulated in the present work, $Pr \approx 0.088$ and it only changes by 0.006 due to temperature-variation of viscosity.

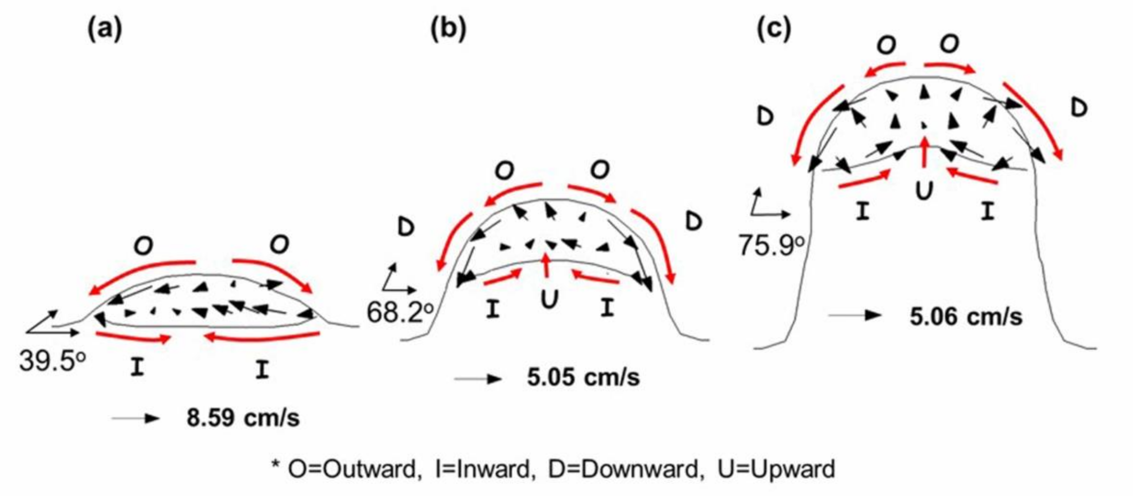

Figure 4.9 Transition of fluid flow pattern and surface flow velocity direction at the mid-length of the deposit. As the deposit height increases, the downward surface flow at the outer edge produces a convex weld pool bottom shape: (a) 1st layer, (b) 3rd layer, and (c) 5th layer

In a typical laser weld, a convex melt pool bottom shape is promoted by high peak surface temperature and associated strong negative lateral temperature gradient leading to strong outward-directed Marangoni force. The high Ma of this surface flow are then correlated to the formation of the convex bottom [16]. However, in LAM increased Ma may not directly relate to increasing melt pool width. Figure 4.9 shows how the fluid flow patterns and the resultant surface velocity change as deposition height increases. For the first layer in Figure 4.9a, the fluid flow pattern is similar to that of conventional welding. Marangoni surface flow is directed outward to the lateral edges in this cross section. Although Ma of the outward flow increases with layer number (1st layer: Ma= 4276; 3rd layer: Ma= 5538), the melt pool widening effect produced by the outward flow on the 3rd layer does not seem to be as strong as that at on the first layer. As more layers are added, Figure 4.9b shows that the pure outward flow is redirected to the downward direction due to the increased angle of the melt pool surface. For the 1st layer, this angle is 39.5° while for the 3rd layer, it is 68.2°. Thus, the flow promotes deeper penetration at the outer edges of the deposit. As a result, the maximum surface velocity decreases from 8.59 cm s^{-1} to 5.05 cm s^{-1} and the convex pool bottom is developed. For fifth layer in Figure 4.9c, the increase of angle to 75.9° and Ma to 6013 promotes inward-directed returning flows at the edges and consequently the more pronounced convex shape with a smaller radius

4.4 Summary and conclusion

A VOF numerical transport simulation was conducted to simulate five-layer LAM deposition. The simulation accurately predicted melt pool peak temperature and deposit geometry. The predicted peak temperatures increase from 2016 K in the first layer to 2071 K in the fifth layer. The predicted overall deposit geometry height is 2.03 cm and the width of individual deposit layers and overall deposit width are 1.59 cm. compared to comparable experimental measurements from literature, the peak temperature prediction error is less than 2.5% and build geometry prediction error is less than 12% in both height and width. From simulation results, calculated values of Pe (27.5 on 1st layer and 21.5 on the 5th layer) were much greater than unity indicating convection is a primary heat transfer mechanism in LAM. The calculated value of Pr changes only by 0.006 over all layers, indicating the variation of melt pool viscosity is not enough to significantly alter melt pool shape between the layers. In contrast, the values of Ma continuously increase with layer number from 4276 on the 1st layer to 6013 on the 5th layer. However, as more layers are added, Marangoni flow near the outer edge of the melt pool is redirected from outward to downward due to the increased surface angle 39.5^{o} on the 1st layer to 75.9^{o} on the 5th. The maximum surface velocity correspondingly decreases from 8.59 cm s^{-1} on the 1st layer to 5.06 cm s^{-1} on the 5th layer. Consequently, the penetration into the solid substrate becomes deeper at the outward edges and the pool bottom becomes more convex. The predicted convex pool bottom shape is comparable to experimental shapes shown in prior LAM literature. Analysis of dimensionless parameters for simulated melt pool shapes and fluid flow patterns showed that the hemispherical melt pool free surface in LAM causes the shaping mechanisms to be different from those for laser weld melt pools formed on flat surfaces.

Future work will be directed at refining the present model to include variation of powder catchment efficiency and laser beam Fresnel reflection with melt pool shape and size. Also, it is anticipated that detailed physical insights provided by integrated process, materials and solid mechanics simulations will eventually allow better prediction of LAM build microstructure and properties and facilitate variation of process parameters used during deposition of 3-D LAM parts to attenuate or accentuate localized microstructure and property variations that can be controlled by melt pool shape and associated solidification structure.

4.5 Acknowledgements

We acknowledge support of this work by Center for Integrative Materials Joining Science for Energy Applications (CIMJSEA, NSF Award GRT00020596). The authors express their thanks to Prof. J.C. Lippold for interest in this project.

4.6 References

1. Frazier WE (2014) Metal additive manufacturing: A review. J Mater Eng Perform 23(6):1917-1928.

2. Raghavan A, Wei HL, Palmer TA, DebRoy T (2013) Heat transfer and fluid flow in additive manufacturing. J Laser Appl 25(5):052006.

3. Cho MH, Farson DF, Lim YC, Choi HW (2007) Hybrid laser/arc welding process for controlling bead profile. Sci Technol Weld Join 12(8):677-688.

4. Hu J, Tsai HL (2008) Modelling of transport phenomena in 3d gmaw of thick metals with v groove. J Phys D-Appl Phys 41(6):065202.

5. Cho J, Farson DF, Hollis KJ, Milewski JO (2015) Numerical analysis of weld pool oscillation in laser welding. J Mech Sci Technol 29(4):1715-1722.

6. Manvatkar V, De A, DebRoy T (2014) Heat transfer and material flow during laser assisted multi-layer additive manufacturing. J Appl Phys 116(12):124905.

7. Kumar A, Paul CP, Padiyar AS, Bhargava P, Mundra G, Kukreja LM (2014) Numerical simulation of laser rapid manufacturing of multi-layer thin wall using an improved mass addition approach. Numer Heat Tranf A-Appl 65(9):885-910.

8. Duitsch U, Schreck S, Rohde M (2003) Experimental and numerical investigations of heat and mass transport in laser-induced modification of ceramic surfaces. Int J Thermophys 24(3):731-740.

9. Alimardani M, Toyserkani E, Huissoon JP (2007) Three-dimensional numerical approach for geometrical prediction of multilayer laser solid freeform fabrication process. J Laser Appl 19(1):14-25.

10. Wen S, Shin YC (2010) Modeling of transport phenomena during the coaxial laser direct deposition process. J Appl Phys 108(4):044908

11. Liu ZY, Qi H (2014) Numerical simulation of transport phenomena for a double-layer laser powder deposition of single-crystal superalloy. Metall Mater Trans A 45A(4):1903-1915.

12. Morville S, Carin M, Peyre P, Gharbi M, Carron D, Le Masson P, Fabbro R (2012) 2d longitudinal modeling of heat transfer and fluid flow during multilayered direct laser metal deposition process. J Laser Appl 24(3):9.
13. Kong F, Kovacevic R (2010) Modeling of heat transfer and fluid flow in the laser multilayered cladding process. Metall Mater Trans B 41(6):1310-1320.

14. Manvatkar V, De A, DebRoy T (2015) Spatial variation of melt pool geometry, peak temperature and solidification parameters during laser assisted additive manufacturing process. Mater Sci Technol 31(8):924-930.

15. Lee Y, Nordin M, Babu SS, Farson DF (2014) Effect of fluid convection on dendrite arm spacing in laser deposition. Metall Mater Trans B 45(4):1520-1529.

16. Limmaneevichitr C, Kou S (2000) Experiments to simulate effect of marangoni convection on weld pool shape. Weld J 79(8):231s-237s.

17. Arora A, Roy GG, DebRoy T (2009) Unusual wavy weld pool boundary from dimensional analysis. Scr Mater 60(2):68-71.

18. Wei PS, Yeh JS, Ting CN, DebRoy T, Chung FK, Lin CL (2009) The effects of prandtl number on wavy weld boundary. Int J Heat Mass Transf 52(15-16):3790-3798.

19. Lee YS, Nordin M, Babu SS, Farson DF (2014) Influence of fluid convection on weld pool formation in laser cladding. Weld J 93(8):292S-300S.

20. Carcel B, Sampedro J, Perez I, Fernandez E, Ramos JA Improved laser metal deposition (lmd) of nickel base superalloys by pyrometry process control. In *Proceedings of 18th International Symposium on Gas Flow & Chemical Lasers & High Power Lasers*, Sofia, Bulgaria. International Society for Optics and Photonics, p 775123

21. Pottlacher G, Hosaeus H, Kaschnitz E, Seifter A (2002) Thermophysical properties of solid and liquid inconel 718 alloy. Scand J Metall 31(3):161-168.

22. Mills KC (2002) Recommended values of thermophysical properties for selected commercial alloys. Woodhead, Cambridge

23. Unocic RR, DuPont JN (2004) Process efficiency measurements in the laser engineered net shaping process. Metall Mater Trans B 35(1):143-152.

24. Xie J, Kar A, Rothenflue JA, Latham WP (1997) Temperature-dependent absorptivity and cutting capability of co2, nd:Yag and chemical oxygen-iodine lasers. J Laser Appl 9(2):77-85.

25. Shelton JA, Shin YC (2010) Comparative evaluation of laser-assisted micro-milling for aisi 316, aisi 422, ti-6al-4v and inconel 718 in a side-cutting configuration. J Micromech Microeng 20(7):12.

26. Picasso M, Marsden CF, Wagniere JD, Frenk A, Rappaz M (1994) A simple but realistic model for laser cladding. Metall Mater Trans B 25(2):281-291.

27. Kelly SM (2004) Thermal and microstructure modeling of metal deposition processes with application to ti-6al-4v. PhD Dissertation, Pennsylvania State University, University Park, PA

28. Vasinonta A, Beuth J, Griffith M Process maps for laser deposition of thin-walled structures. In *Proceedings of Solid Freeform Fabrication*, Austin, Solid Freeform Fabrication Proceedings (Series). University of Texas at Austin, pp 383-391

29. Pinkerton AJ, Li L (2004) Modelling the geometry of a moving laser melt pool and deposition track via energy and mass balances. J Phys D-Appl Phys 37(14):1885-1895.

30. Gharbi M, Peyre P, Gorny C, Carin M, Morville S, Le Masson P, Carron D, Fabbro R (2013) Influence of various process conditions on surface finishes induced by the direct metal deposition laser technique on a ti-6al-4v alloy. J Mater Process Technol 213(5):791-800.

Chapter 5: Surface Tension-Powered Surface Finish Control in Laser Additive Manufacturing Process

5.1 Introduction

Laser additive manufacturing (LAM) is considered to be an important new commercial manufacturing technology and there has been considerable research to understand the process and to prove and refine its capabilities. LAM has huge potential for near net-shape fabrication of highly complex parts but also creation of graded structures by simultaneous deposition of dissimilar metal powders [1,2]. Despite these unique advantages, broad application of LAM has been impeded by issues with cost and production rate and the difficulty of predicting the dimensional tolerances and properties of finished products. Overcoming these issues requires deep understanding of the relationships between process parameters, melt pool fluid flow and geometry, and predicted melt pool shape and build microstructure from a numerical simulation of the LAM process [2,3].

LAM is a layer-by-layer deposition process that uses simultaneous metal powder injection and laser heat input to form a melt pool on top of previously-deposited material. A schematic illustration of blown-powder LAM process is shown in Figure 1.1(a). The powder particles are carried by an inert gas through the annular powder feed nozzle surrounding a concentric focused laser beam. The laser heat input melts the powder particles and the surface of the previously deposited layer to form a melt pool, which is traversed linearly and solidifies to form a deposit layer. Only the powder particles hitting the melt pool contribute to formation of deposit layer. Others ricochet from the substrate solid surface. The flowing powder particles create a powder cloud between the nozzle exit and substrate. The laser beam interacts with and heats the particles in the cloud and the laser power is attenuated by absorption, reflection and radiation due to the laser-powder interactions [4]. Numerical simulation in predicting the individual particle motions and laser-powder interactions is too computationally intensive to be practical. More recently, researchers have performed experiments to measure overall laser absorption, reflection, transmission and thermal radiation due to laser-powder cloud interactions for known deposition process parameters [5].

Prior researchers have developed numerical laser cladding simulations that quantitatively predict specific aspects of heat flow or melt-pool phenomena relevant to laser additive manufacturing [6-11]. However, fluid flow simulations for LAM are still at an initial stage of development [12] since laser-powder-substrate interactions are complex and accurate representation of process parameter interactions is challenging. As a result, a relatively small number of LAM simulations have been reported. Most prior studies utilized finite element method (FEM) [10,13,14], which does not explicitly calculate heat convection by melt pool fluid flow. Prior transport fluid simulations investigated multiple layer builds with a predefined melt pool surface shape [12] and two or three layers [15,16]. Therefore, a more advanced melt-pool transport simulation of the LAM process will help to not only understand the relationship between melt pool shape and process parameters but also to identify process modifications that improve surface finish quality.

Although laser additive manufactured parts typically are used with little or no post-machining, dimensional accuracy of as-deposited parts may still not be sufficient for applications requiring high precision parts. Moreover, post-process machining may not be possible for internal features or complex external geometries. Ideally, optimum surface finish and dimensional accuracy would be obtained if deposition were done with a thin and stable deposit melt pool that is invariant with process parameters and fluid dynamics. However, in reality, melt pool shape changes with various fluid forces (thermocapillary stress and buoyancy force) and external process inputs (momentum force by injected powder particles and shield gas pressure) applied to the melt pool [3,17]. For instance, thermocapillary driven fluid flow, often called Marangoni flow or thermocapillary convection, strongly influences melt pool shape, heat and mass transfer that eventually change temperature gradient, surface finish and dimension accuracy of laser additive manufactured parts.

The spatial variation of thermocapillary due to surface temperature variation of the melt pool always causes molten metal to flow from lower to higher surface tension regions. Yet, since thermocapillary is temperature- and composition-dependent, the thermocapillary gradient can be changed from negative to positive and vice versa [18] by changing these variables. The relationship between thermocapillary gradient, temperature, fluid flow pattern and resulting melt pool shapes is illustrated in Figure 5.1. For an axisymmetric melt pool with a negative thermocapillary gradient, thermocapillary stress radially carries fluid outward from the center shown in Figure 5.1(a). As a result, the melt pool has wide and shallow shape. For the melt pool with a positive thermocapillary gradient illustrated in Figure 5.1(b), the fluid flow becomes reversed from radially outward to radially inward and the melt pool shape is altered to narrow and deep. In the illustration for a mixed thermocapillary gradient in Figure 5.1(c), two opposing fluid flows collide and the shape of the weld pool bottom becomes non-uniform. A mixed gradient is produced in the melt pools containing ppm levels of sulfur. The change thermocapillary temperature gradient from positive to negative is found at the maximum point corresponding to temperature T_{max}. The location of this maximum temperature varies with the concentration of surface active elements (for example, sulfur or oxygen) on the melt pool surface. The latter is interesting for applications because oxygen content in the LAM build chamber atmosphere can be accurately controlled.

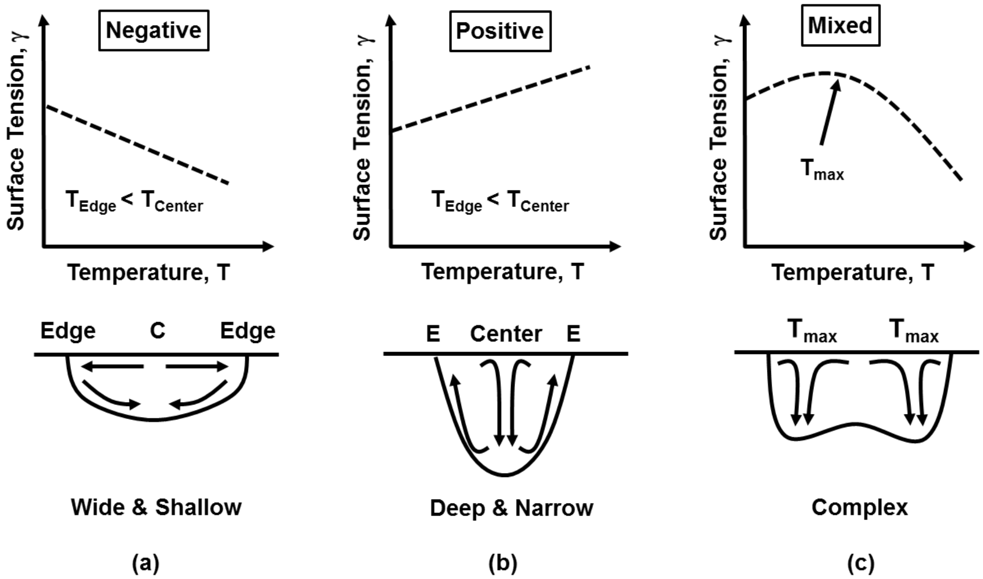

Figure 5.1 Different fluid flow pattern and melt pool shapes produced by different directions of thermocapillary gradient: (a) negative, (b) positive and (c) mixed gradient

In present research, the melt pool transport simulation is used to investigate the effect of thermocapillary-temperature gradient on melt pool fluid flow pattern. Moreover, the melt pools with mixed thermocapillary gradients having varying T_{max} are simulated to predict the resulting changes of melt pool shape and build deposit geometry. This research aids in the selection of thermocapillary-temperature gradient for the best build surface finish quality and also provides insights into underlying fundamentals of the LAM process.

5.2 Physical model

5.2.1 Governing equations

LAM process always involves complex physical phenomena associated with continuous powder injection and laser heating of the molten pool. The addition of mass, energy and momentum alter fluid temperature and flow resulting in change of weld pool size and shape. Thus, transient analysis of transport phenomena in and around the melt pool as material is deposited is essential. In this study, numerical simulation (Flow3D, FlowScience) is used to predict melt pool transport phenomena based on conservation equations of mass, energy and momentum. The transport expressions used in the simulation are given as:

$$\nabla \cdot \vec{v} = \frac{\dot{m}_s}{\rho} \tag{1}$$

$$\frac{\partial h}{\partial t} + \overrightarrow{(v} \cdot \nabla)h = \frac{1}{\rho}(\nabla \cdot \kappa \nabla T) + \frac{\dot{h}_s}{\rho} \tag{2}$$

$$\frac{D\vec{v}}{Dt} = -\frac{1}{\kappa}\nabla P + \mu \nabla^2 \vec{v} + \vec{g}[1 - \beta(T - T_m)] + \frac{\dot{\vec{p}}_s}{\kappa} \tag{3}$$

Incompressible and Newtonian fluid are assumed. Here, $\vec{v}$ is fluid velocity vector, $\dot{m}_s$ is mass addition rate, ρ is density of liquid metal, , *h* is enthalpy, *t* is time, *κ* is thermal conductivity, *T* is temperature, $\dot{h}_s$ is rate of enthalpy addition associated with the added material, *P* is hydrodynamic pressure, *μ* is viscosity, $\vec{g}$ is gravitational acceleration vector in z direction, β is thermal expansion constant, T_m is melting temperature and $\vec{P}_s$ is momentum addition rate associated with the mass addition.

The simulation uses the Volume of fluid (VOF) method to predict the transient location and shape of the void-fluid interface by simultaneously solving the above conservation equations with a fourth equation representing conservation of volume, expressed as:

$$\frac{\partial F}{\partial t} + \nabla \cdot (\vec{v}F) = \dot{F}_s \tag{4}$$

where F denotes fluid volume fraction in a simulation grid cell. F=0 indicates a void region where no fluid is present and F=1 indicates completely filled fluid region. An intermediate value of $0 < F < 1$ indicates a cell contains an interface between void and fluid regions. Metal powder and laser heat inputs to the melt pool are represented by source terms in all of above conservation equations.

5.2.2 Boundary conditions and physical properties

For a reasonably accurate simulation, several calibrations were made to process inputs. To approximate of laser heating in the LAM process, laser-powder-substrate interaction should be considered. Laser energy input to the melt pool is decreased by reflection, radiation, and absorption by powder particles and by reflection, convection and radiation from the melt pool surface. Values for these energy losses have been reported in prior experimental literature [5]. 9% loss was measured for absorption and reflection from the powder cloud and 1% for convection and radiation from the substrate. Laser reflectance varies significantly with deposit geometry, substrate material, surface oxidation, beam incident angle and laser polarization and wavelength, an approximate value of 50% reflectance (40 % absorptance) at the pool surface was assumed for this study. For comparison, the Hagen-Rubens relationship [19] for Nd-YAG laser wavelength and predicts absorptance of 35% at 1533K (solidus) and 43% at 1609K (liquidus). Thus, the absorptance of 40% used in this simulation is reasonable.

A moving laser with flat-top distribution was used as a surface heat flux boundary condition in the simulation. The heat is conducted and convected in the melt pool and build deposit. A mass flux for the powder injection was incorporated into the computation domain just above the free surface of the substrate. The position of the source was elevated as the layers were deposited. The initial temperature of powder particles injected into the melt pool was assumed to be just above the liquidus temperature.

The powder catchment efficiency can be estimated by the ratio between total powder input and amount of powder contributing to formation of the deposit layer. A value of 47% was assumed as reasonable based on the work of Weisheit *et al.* [20].

As described previously in discussion of Figure 5.1, thermocapillary gradient is well known to be a significant driving force for flow in conduction-mode laser melt pools that has significant effects on fluid circulation and resulting pool shape. Three different types of thermocapillary–temperature gradients are used in present study: negative, positive and mixed are shown in Figure 5.2 below. All three types (in four cases) have a surface tension of 1842 dyne/cm at the liquidus temperature, taken from experimental data for the surface tension of pure alloy IN718 [21].The negative type corresponds to a thermocapillary gradient coefficient of -0.11 dyne/cm K at temperatures above the liquidus. However, the presence of surface active elements such as sulfur or oxygen can cause positive thermocapillary gradients at temperatures above the liquidus temperature. In this simulation, the positive thermocapillary used a gradient coefficient +0.11, opposite to the negative gradient. The mixed gradient is the most realistic for fluids containing surface active elements [22,23]. The mixed thermocapillary gradient-temperature relationship depends on sulfur content of the material. Sulfur concentrations of 6 ppm and 10 ppm are assumed in this study. The temperatures at which the peak of thermocapillary occurs are 1818K and 1941K, respectively. More details of the mixed thermocapillary–temperature calculation have been given in a previous publication [4].

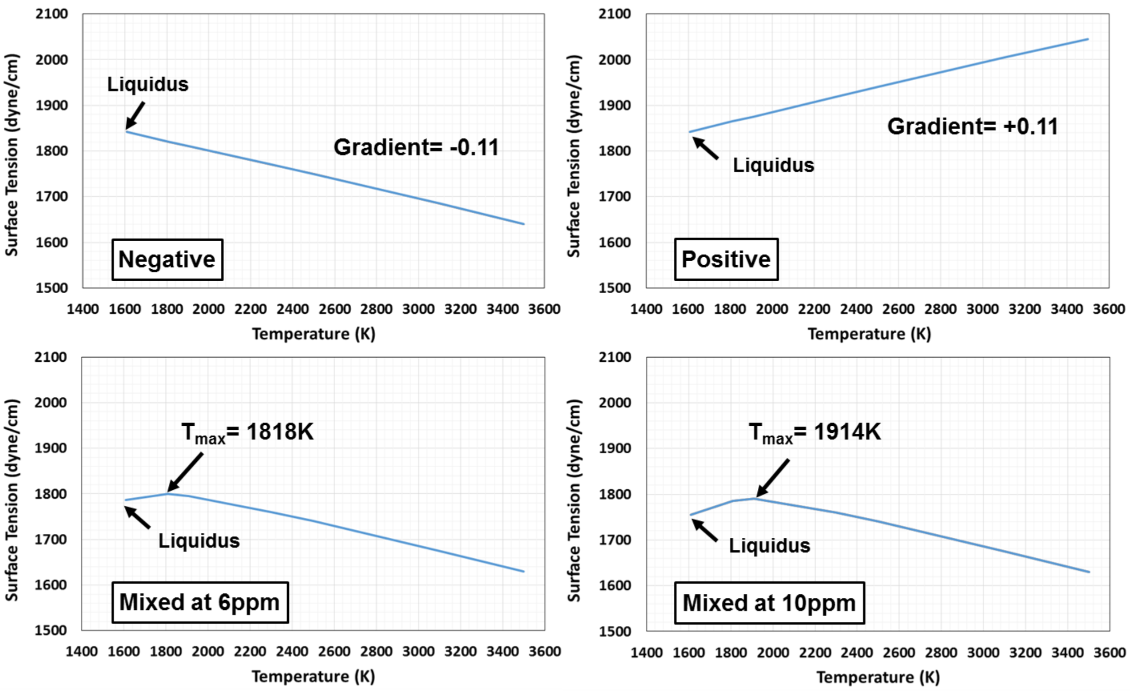

Figure 5.2 Surface tension–temperature gradients used in the simulations: negative, positive, mixed at 6 ppm and 10 ppm sulfur

The simulation was conducted in a 3-D computation domain with dimensions of 2.8 cm (X-direction), 1.5 cm (Y-direction) and 0.9 cm (Z-direction) as shown in Figure 5.3 below. The substrate occupies the region $0 < Z < 0.5$ cm and void occupies the region $0.5 < Z < 0.9$. The region $0 < Z < 0.4$ is meshed with coarse mesh blocks to reduce computational load. The upper fine mesh block has 262,500 cubic cells with edge length 200 µm and the lower block contains coarse mesh block 26,600 cubic cells with edge length 400 µm.

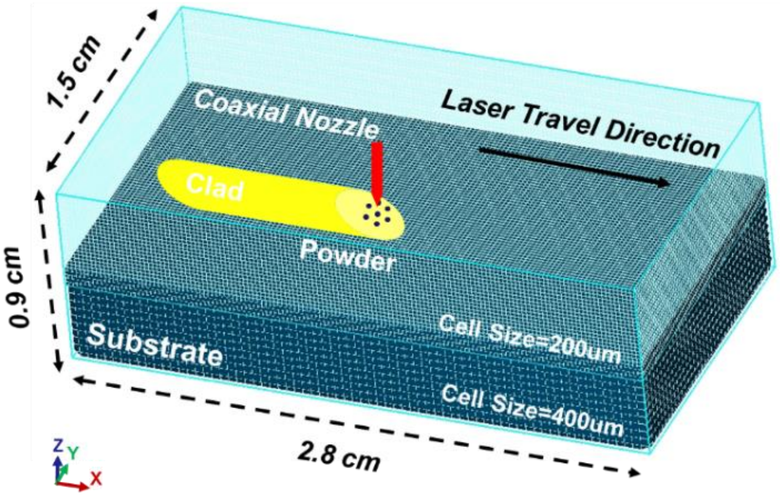

Figure 5.3 Schematic description of computation domain

Thermophysical properties and manufacturing parameters used in this simulation are given in Table 5.1. The powder particles and substrate material are both Ni-based superalloy IN718. The room temperature is assumed as 300 K for material and surroundings.

Table 5.1 Thermophysical properties and manufacturing parameters used in simulation [20,21,24,25]

Property and Parameters	Value [units]
Specific Heat of Liquid	7.25e+06 [cm^2/s^2 K]
Specific Heat of Solid	5.77e+06 [cm^2/s^2 K)
Conductivity of Liquid	2.928e+06 [g cm/s^3 K]
Conductivity of Solid	2.792e+06 [g cm/s^3 K)
Liquidus Temperature	1609 [K]
Solidus Temperature	1533 [K]
Latent Heat	2.27e+09 [cm^2/s^2]
Viscosity	0.196*exp(5848/T) [mPa]
Density of Liquid	[7400-0.88 (T-1609)]/1000 [g/cm^3]
Density of Solid	[8190 - 0.392 (T-298)]/1000 [g/cm^3]
Surface Tension	1842 [dyne/cm]
Thermocapillary Gradient Coefficient	+-0.11 [dyne/cm K]
Beam Spot Size	1.95 [mm]
Powder Feed Rate	7 [g/min]
Beam Power	700 [W]
Idle time between passes	0 [s]
Powder Catchment Efficiency	47 [%]
Velocity of Laser Beam	1.083 [cm/s]

5.3 Result and discussion

A characteristic build deposit feature referred to as a bulge can be seen in Figures 5.4 and 5.5. The cause of the bulge has been previously studied in laser and hybrid laser-arc welding. It was reported that the bulge is usually observed at the starting point of the deposit and related to fluid flow to minimize surface tension of the deposit [26,27]. Also, it was found that longer melt pools can lead to larger bulge widths because the longer pool allows more molten metal to flow to the rear of the melt pool in response to thermocapillary force. Morgan *et al.* [28] addressed the roles of surface tension force and energy minimization in producing spherical melt pool free surfaces. Asymmetric downward bulging of deposits on a vertical surface was shown during the laser rapid manufacturing process [29]. It noted that gravity is the key factor causing the downward rounded bulge. Based on prior literature, understanding of interactions between surface tension, gravity and fluid convection is essential to explain the bulging mechanisms in LAM.

The effect of thermocapillary gradient on deposit sidewall geometry can be understood by analysis of the simulation results shown in Figure 5.4. Five layer deposits created with melt pools having negative and positive thermocapillary gradient are displayed in Figures 5.4(a) and 5.4(b), respectively. In both cases, the distinctive bulge of the deposit sidewall is observed at starting position. For simulations with melt pools having mixed thermocapillary gradient with maximum temperatures T_{max} of 1818K and 1914K in Figures 5.4(c) and 5.4(d), a decrease in the width of the sidewall bulge is noted for both mixed thermocapillary gradients. The variation of bulge width with thermocapillary gradient types is illustrated by the cross sections in Figure 5.5. These results are studied in more detail to better understand the effects of thermocapillary gradient on deposit dimensions in Figures. 5.6, 5.7 and 5.8.

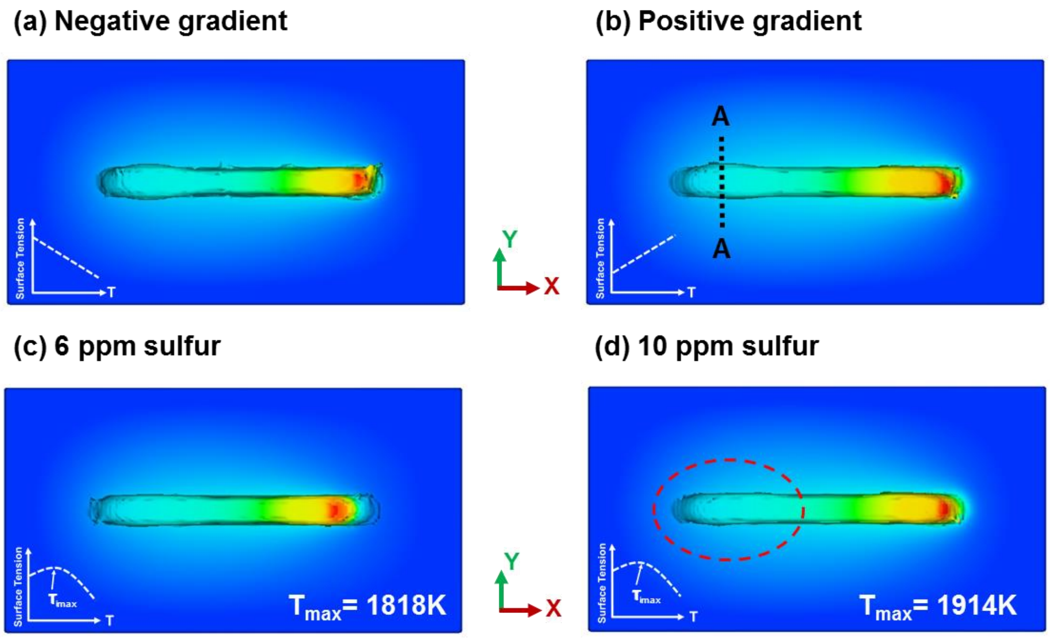

Figure 5.4 Effect of thermocapillary gradients on deposit geometry at the starting position

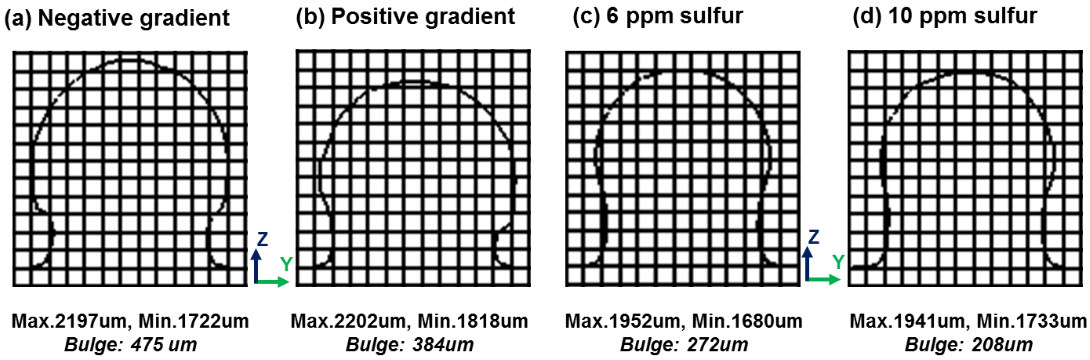

Figure 5.5 Measurement of simulated deposit widths and their variance with thermocapillary gradients. A cell size is 200 μm

The effect of the bulge on deposit sidewall dimension can be expressed in a simple subtraction of minimum width from maximum width. Image processing software (ImageJ, NIH) is used to measure the maximum and minimum values from the simulated results shown in Figure 5.5. The deposit manufactured with material having the negative gradient type, shown in Figure 5.5(a), has the largest bulge width of 475 μm. A deposit made with material having positive thermocapillary gradient is shown in Figure 5.5(b). The bulge width is decreased by approximately 100 μm compared to the negative gradient case. In Figures 5.5(c) and 5.5(d), further reduction in the bulge width is observed for the mixed thermocapillary gradients with two different levels of sulfur. The value is 272 μm for 6 ppm and 208 μm for 10 ppm. It is noted that bulge width is decreased by approximately 56% compared to that for the negative gradient. From these results, it is concluded that non-uniform and inhomogeneous surface finish can be optimized by manipulating thermocapillary gradient.

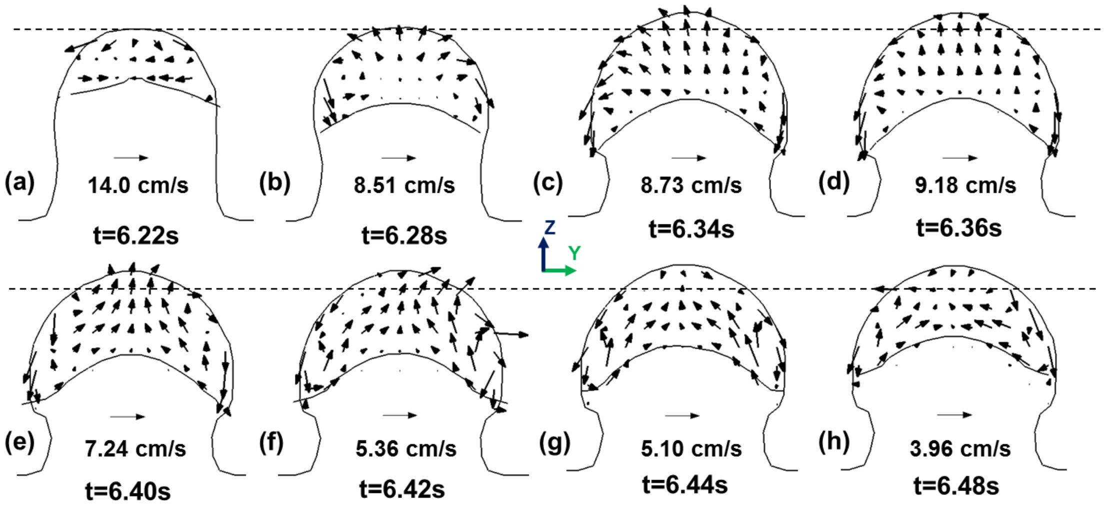

Figure 5.6 Evolution of a bulge at the edges of the deposit near the start of deposition the 5th layer of material with a negative thermocapillary gradient

Figure 5.6 displays the bulge and the fluid flow pattern in the melt pool at fifth layer deposit with a negative thermocapillary gradient. The deposit is cross-sectioned along A-A line shown in Figure 5.4(b). The bulge is not observed on the sidewall of deposit in Figure 5.6(a). Mainly outward fluid flow along the melt pool surface exists and the surface fluid velocity is the fastest in the melt pool. In Figure 5.6(b), downward flow begins to develop at the melt pool edge and the velocity decreases to 8.51 cm /s. At this step, the bulge starts to form at the edges but it is not large. In Figure 5.6(c) and 5.6(d), the bulge becomes more pronounced at the edges with the increase of the width and height of the melt pool and the fluid velocity. In Figure 5.6(e), 5.6(f), 5.6(g) and 5.6(h), the bulging action is dominant and enhances a peculiar convex melt pool bottom shape at fusion boundary. As the returning flow develops along the bottom edge of the melt pool, the flow pushes the fusion boundary of the pool inwards at the edges. Consequently, the pool has a more obtuse angle at outer edge. As the beam moves away, the pool cools and solidifies. Thus, the pool bottom moves upward and the fluid velocity becomes slower and slower.

The bulge in multiple layer additive manufacturing is much more complex phenomena than that in conventional welding or one-layer laser additive manufacturing process because it is caused by interaction of surface tension, gravity effect associated with interaction time between deposit layers, and fluid convection. First, surface tension tends to make a generally round melt pool surface shape to minimize surface energy. However, the deposit shape at the edges is not perfectly round due to gravity effect. Also, interaction time between the 4th and 5th deposition layers has important effects on melt pool size, shape and fluid flow at times near the beginning of the 5th layer. The top solid surface of the 4th layer is at a relatively high temperature at the start of the 5th deposition layer because heat input at the end of the 4th layer has not had much time to dissipate due to continuous deposition process. Therefore, the melt pool fluid volume becomes larger and deeper and the average temperature increases. As a result of the increased temperature, viscosity and density of the fluid decrease so that the melt pool has less resistance against gravity force. The melt pool size and gravity force at the bottom of the melt pool are larger and there is more tendency for the melt to slide down the edge of the deposit. Lastly, outward surface fluid flow due to the negative thermocapillary gradient pushes the liquid to the edges so that the sidewall of the deposit expands. Meanwhile, the combined force of downward flow and gravity pushes the fluid down along the surface of the sidewall. As a result, the sidewall has the bulged edges.

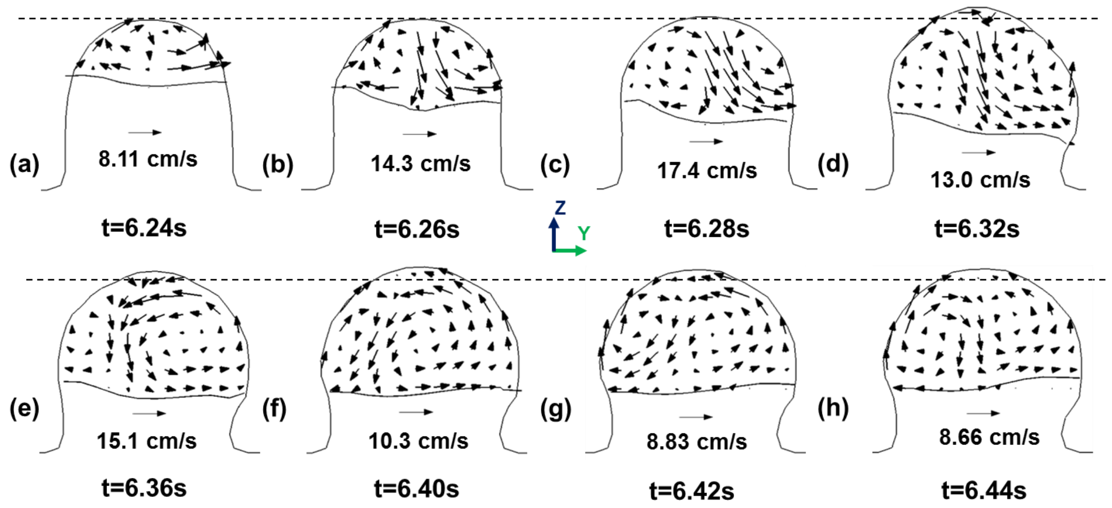

Figure 5.7 Evolution of fluid flow and bulging of weld deposit side at the start of the fifth layer of deposition of material with a positive thermocapillary gradient

Figure 5.7 illustrates the evolution of fluid flows and the sidewall of the deposit at a time near the beginning of deposition of the 5th layer with fluid having positive thermocapillary gradient. In Figure 5.7(a), there is no bulge observed at the sidewall of the deposit. In Figure 5.7(b), the inward and downward fluid flow begins to develop at the top center of the melt pool surface due to the positive thermocapillary gradient. As a result, a concave melt pool bottom is created at the fusion boundary. As the melt pool size increases due to remelting of the 4th layer and deposition of additional material, the maximum fluid circulation velocity increases to 17.4 cm/s in Figure 5.7(c). In Figure

5.7(d), a slight amount of sidewall bulging can be noted. In Figure 5.7(g), the bulge has become more pronounced and the maximum fluid velocity on the pool surface has decreased to 8.83 cm/s. In Figure 5.7(h), there is inward and downward flow at the center of the melt pool. Interestingly, although the simulation predicts similar bulge sidewall shapes in deposits made with melt pools having negative and positive gradients, the fluid flow patterns that form the bulge are significantly different.

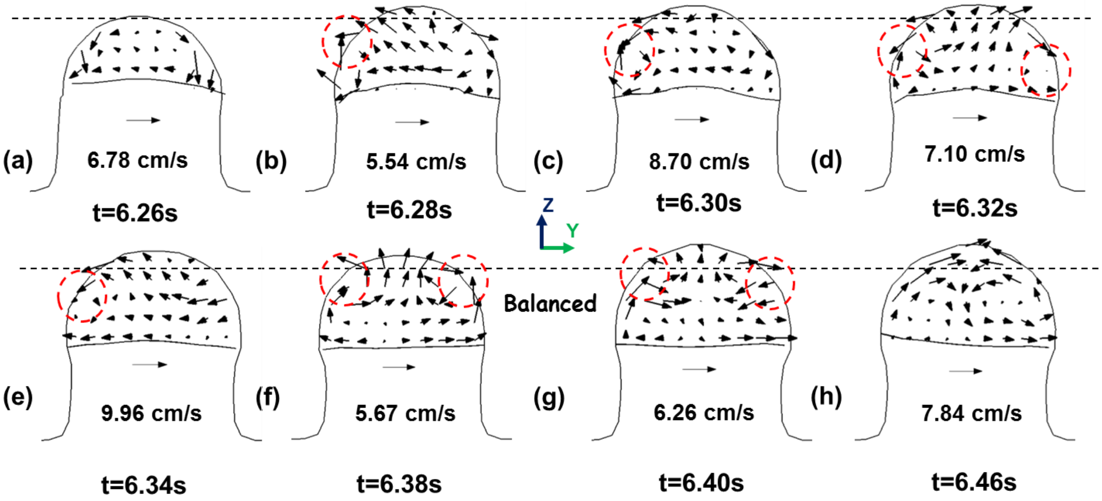

Figure 5.8 Evolution of fluid flow and bulging of weld deposit side during on fifth layer deposition in mixed thermocapillary gradient (10 ppm sulfur case)

Figure 5.8 shows the fluid flow in the melt pool and transient evolution of the deposit made with material with 10 ppm sulfur and a mixed thermocapillary gradient. At the beginning of the fifth layer deposition in Figure 5.8(a), the dominant flow pattern is outward and downward so the tendency to bulging at the sideway is strong. However, in

Figures 5.8(b)-(g), collision of two opposing flows caused by the transition of the thermocapillary gradient is observed. The region of colliding flows is highlighted by a red dashed circle. Once collision of opposing surface flows occurs, the resultant downward flow is produced at the mid area of the melt pool. Unlike the purely positive and negative thermocapillary gradient cases, this downward flow appears to reduce the bulging action in this case of mixed thermocapillary gradient with 10 ppm sulfur.

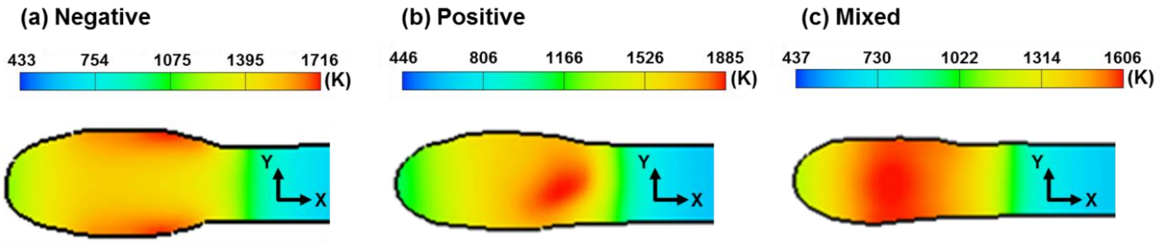

Figure 5.9 Characteristic temperature distributions near the beginning of the 5th layer in deposits made with material having melt pools with (a) negative, (b) positive and (c) mixed thermocapillary gradients

Figure 5.9 shows temperature distributions in X-Y horizontal sections of deposits made with fluids having different thermocapillary gradients. The time is 6.40s, near the beginning of deposition of the 5th layer (the cooler blue-colored material at the right of the figures is the un-melted top surface of the 4th layer). The z-axis location of the section is at the location of the maximum bulge width, which is somewhat above the bottom of the 5th layer melt pool. Those are taken from simulations with melt pools having negative, positive and mixed 10 ppm sulfur gradients. The maximum temperature is observed at the edge of deposit in Figure 5.9a) whereas the maximum temperature is located in the center region in Figure 5.9(b). Unlike the prior two cases, a relatively uniform distribution is observed in the melt pool for the mixed gradient case shown in Figure 5.9(c). The cause of the different temperature distribution can be explained by the fluid flow patterns as discussed above. With materials with negative thermocapillary gradient in Figure 5.9(a), hot molten fluid is first pushed out to the edge at the top surface of the deposit and slides downward. Thus, it undergoes additional convectional cooling by shielding gas. As a result, a lower maximum temperature 1716K is found in the negative gradient case. In contrast, for material with positive thermocapillary gradient in Figure 5.9(b), flow carries the hot molten fluid to the center first so that inward and downward flow keeps higher temperature inside at the center of the deposit. There is less convectional cooling made by the surrounding gas. Thus, the fluid can remain at a relatively high maximum temperature 1885K compared to the negative gradient case. In Figure 5.9(c), the maximum temperature is the lowest 1606K and temperature distribution is relatively uniform along Y direction because collision of opposing hot and cold fluid flows mixes the fluids leads to additional reduction of maximum temperature and temperature gradient throughout the cross-section. Because maximum temperature, temperature distribution and its gradient are different at the three thermocapillary gradient cases, it can be assumed that different scales of solidified microstructures will be produced at the sides and center of the deposit due to variation of temperature gradient and solidification rate at the melt pool solidification boundary. Efforts to predict microstructure variation in LAM deposits using the 3-D transport simulation are planned in the future.

5.4 Summary and conclusion

The numerical simulation developed by this work provided insight into distinct melt pool fluid flow patterns occurring during laser additive manufacturing with material compositions that result in three different types of thermocapillary gradients and their effect on the final build geometry. The simulation results showed that bulge at the start of the build was reduced by melt pool having a mixed thermocapillary gradient. The lateral width of the bulge was approximately 56% less than that of the bulge width of a deposit made with a material having a negative gradient. Thus, it can be said that non-uniformity and surface finish of the deposit sidewall can be optimized by the manipulation of the thermocapillary gradient of the melt pool present during layer-by-layer deposition. More accurate build geometry and reduced sidewall bulge can be expected to lead to lower cost of flexible-manufactured parts. Also, the simulation results showed effects of the particular fluid flow patterns for the various thermocapillary gradient types on deposit and build geometry. Interestingly, a similar mushroom shape bulge was produced at the lateral edge of the start of deposits made with material having both positive and negative gradients. In comparison, the collision of opposing melt pool fluid flows that occurred during deposition of material having mixed gradient minimized deposit bulging. Characteristic build temperature distributions in X-Y cross-sections were predicted for deposition with the three different thermocapillary gradients. Different thermocapillary gradients led to different maximum temperature, temperature distribution and solidification gradient and rates which would result in different solidified microstructure and properties of the build. Further research is required to define the relationships between solidification conditions and final microstructure and properties of the multi-layered deposit. Overall, this work contributes to application of melt pool simulation for LAM process as well as suggestion of a possible method for reduction of manufacturing cost based on the understanding of the relationship between thermocapillary gradient, fluid flow motion and resultant change of melt pool and deposit geometry.

5.5 Acknowledgements

The authors would like to thank Center for Integrative Materials Joining Science for Energy Applications (CIMJSEA) for supporting this project. The authors also express their thanks to Prof. W. Zhang for helpful support and interest in this project.

5.6 References

1. Zhou JH, Zhang YW, Chen JK (2009) Numerical simulation of random packing of spherical particles for powder-based additive manufacturing. Journal of Manufacturing Science and Engineering: ASME 131(3):031004.

2. Mazumder J, Schifferer A, Choi J (1999) Direct materials deposition: Designed macro and microstructure. Materials Research Innovations 3(3):118-131.

3. Gharbi M, Peyre P, Gorny C, Carin M, Morville S, Le Masson P, Carron D, Fabbro R (2013) Influence of various process conditions on surface finishes induced by the direct metal deposition laser technique on a Ti-6Al-4V alloy. Journal of Materials Processing Technology 213(5):791-800.

4. Lee YS, Nordin M, Babu SS, Farson DF (2014) Influence of fluid convection on weld pool formation in laser cladding. Welding Journal 93(8):292S-300S.

5. Gedda H, Powell J, Wahlstrom G, Li WB, Engstrom H, Magnusson C (2002) Energy redistribution during co_2 laser cladding. Journal of Laser Applications 14(2):78-82.

6. Tabernero I, Lamikiz A, Ukar E, Martinez S, Celaya A (2014) Modeling of the geometry built-up by coaxial laser material deposition process. International Journal of Advanced Manufacturing Technology 70(5-8):843-851.

7. Wen SY, Shin YC (2010) Modeling of transport phenomena during the coaxial laser direct deposition process. Journal of Applied Physics 108(4):044908.

8. Vasquez F, Ramos-Grez JA, Walczak M (2012) Multiphysics simulation of laser-material interaction during laser powder depositon. International Journal of Advanced Manufacturing Technology 59(9-12):1037-1045.

9. Choi J, Han L, Hua Y (2005) Modeling and experiments of laser cladding with droplet injection. Journal of Heat Transfer: ASME 127(9):978-986.

10. Toyserkani E, Khajepour A, Corbin S (2004) 3-d finite element modeling of laser cladding by powder injection: Effects of laser pulse shaping on the process. Optics and Lasers in Engineering 41(6):849-867.

11. Picasso M, Rappaz M (1994) Laser-powder-material interactions in the laser cladding process. Journal de Physique IV 4(C4):27-33.

12. Manvatkar V, De A, DebRoy T (2014) Heat transfer and material flow during laser assisted multi-layer additive manufacturing. Journal of Applied Physics 116(12):124905.

13. Kumar A, Paul CP, Padiyar AS, Bhargava P, Mundra G, Kukreja LM (2014) Numerical simulation of laser rapid manufacturing of multi-layer thin wall using an improved mass addition approach. Numerical Heat Transfer Part A: Applications 65(9):885-910.

14. Alimardani M, Toyserkani E, Huissoon JP (2007) Three-dimensional numerical approach for geometrical prediction of multilayer laser solid freeform fabrication process. Journal of Laser Applications 19(1):14-25.

15. Liu ZY, Qi H (2014) Numerical simulation of transport phenomena for a double-layer laser powder deposition of single-crystal superalloy. Metallurgical and Materials Transactions A 45A(4):1903-1915.

16. Kong FR, Kovacevic R (2010) Modeling of heat transfer and fluid flow in the laser multilayered cladding process. Metallurgical and Materials Transactions B 41(6):1310-1320.

17. Pinkerton AJ (2010) Laser direct metal deposition: Theory and applications in manufacturing and maintenance. In: Advances in laser materials processing: Technology, research and applications. Woodhead Publishing Ltd., Cambridge, England, pp 461-491

18. Lee PD, Quested PN, McLean M (1998) Modelling of marangoni effects in electron beam melting. Philosophical Transactions of the Royal Society A 356(1739):1027-1043.

19. Xie J, Kar A, Rothenflue JA, Latham WP (1997) Temperature-dependent absorptivity and cutting capability of CO_2, Nd:YAG and chemical oxygen-iodine lasers. Journal of Laser Applicatoins 9(2):77-85.

20. Weisheit A, Backes G, Stromeyer R, Gasser A, Wissenbach K, Poprawe R (2001) Powder injection: The key to reconditioning and generating components using laser cladding. In: Proceedings of the international congress on advanced materials and processes, materials week 2001. Munich, Germany, pp 1-8

21. Mills KC (2002) Recommended values of thermophysical properties for selected commercial alloys. Woodhead Publishing Ltd., Cambridge, England

22. McNallan MJ, Debroy T (1991) Effect of temperature and composition on surface tension in Fe-Ni-Cr alloys containing sulfur. Metallurgical and Materials Transactions B 22(4):557-560.

23. Zacharia T, David SA, Vitek JM, Debroy T (1989) Weld pool development during gta and laser beam welding of type 304 stainless steel: Part 1-theoretical analysis. Welding Journal 68:499S-509S.

24. Carcel B, Sampedro J, Perez I, Fernandez E, Ramos JA (2010) Improved laser metal deposition (lmd) of nickel base superalloys by pyrometry process control. In: Proceedings of spie-the international society for optical engineering. Sofia, Bulgaria, p 775123

25. Pottlacher G, Hosaeus H, Kaschnitz E, Seifter A (2002) Thermophysical properties of solid and liquid inconel 718 alloy. Scandinavian Journal of Metallurgy 31(3):161-168.

26. Su WN, Erasenthiran P, Dickens PM (2003) Investigation of fully dense laser sintering of tool steel powder using a pulsed Nd : YAG (neodymium-doped yttrium aluminium garnet) laser. Proceedings of the Institution of Mechanical Engineers, Part C: Journal of Mechanical Engineering Science 217(1):127-138.

27. Cho MH, Farson DF (2007) Simulation study of a hybrid process for the prevention of weld bead hump formation. Welding Journal 86(9):253S-262S.

28. Morgan R, Sutcliffe CJ, O'Neill W (2001) Experimental investigation of nanosecond pulsed Nd : YAG laser re-melted pre-placed powder beds. Rapid Prototyping Journal 7(3):159-172.

29. Paul CP, Mishra SK, Kumar A, Kukreja LM (2013) Laser rapid manufacturing on vertical surfaces: Analytical and experimental studies. Surface and Coatings Technolog 224:18-28.

Chapter 6: Random Particle Packing Simulation with Asymmetric Size Distribution for Laser Powder Bed Additive Manufacturing

6.1 Introduction

Laser and powder based additive manufacturing is rapid and efficient process since it can build near net-shape of complex parts from a 3D computer-aided design (CAD) data of the part, which is not obtainable from the conventional manufacturing processes [1, 2]. Despite the benefit in design and productivity, there are still obstacles present such as porosity, residual powder and rough surface preventing its broad commercial application [3]. In order to avoid these defects, a comprehensive understanding of the key process parameters is essentially required, which is mainly categorized into energy input, powder bed properties and build conditions [4, 5]. So far, significant progress has been made in experimental and numerical study of energy input and build conditions (e.g. laser power, scanning speed, layer thickness and scan pattern) but not in the study of powder bed properties because it is still hard to quantify via experiment [1]. Therefore, advanced means of obtaining the structural particle properties are required in the rapidly growing additive manufacturing area.

With advancement of computers and computational algorithms in recent decades, numerical simulation becomes a promising alternative to experiment for study of the particle packing properties. In broad category, present packing algorithms can be grouped into three general types: sequential addition [1], collective rearrangement [6] and dynamic simulation [7]. The first algorithm starts with an initial sphere and then drops spheres sequentially one by one into a box under gravity. The stable final position of sphere is determined by having three contacts with preexisting sphere or by hitting the floor. The second kind of algorithm starts with a dense packing of spheres, which can overlap. Then, the spheres are moved in order to remove all overlaps in the computation domain. As a result, very dense packing is achieved by this method whose result is sometimes even higher than experiment result [8]. However, since these two algorithms stems largely from geometrical consideration, they cannot accurately simulate fine particle packing which depends on not only gravitational force but also interparticle forces [7]. The last algorithm is built on Discrete Element Method (DEM) [9-11]. This method simulates each individual particle as a dynamic process where interparticle forces such as friction, rolling resistance, collision between particles, van der Waals and electromagnetic forces are readily considered in an explicit manner.

Random particle packing simulation is useful to represent powder bed system since highly complex packing structure can be fully described with simple geometric terms such as radius and position of individual particles. Numerous researchers have developed particle packing models in mono or bimodal size distribution [1, 9, 10, 12] to know quantitative particle packing density and structure. In reality, however, powder particles have a continuous probability distribution in size over a certain range due to the limitation of manufacturing process so that producing particles with uniform distribution is impossible with current technologies [8]. Hence, Gaussian with various size range has been used for non-uniform particle packing simulation but in our best knowledge, none of the numerical models has investigated packing density and other structural properties with a skewed particle size distribution (PSD) in a fixed size range. Indeed, the impact of the fractional difference in size on part failure was reported in experimental literature [13].

In this research, advanced powder packing simulation DEM is used to capture particle packing features in three different particle size types over asymmetric 2.5 µm to 35 µm particle radius range. Also, a realistic axial mechanical vibration is incorporated into the system to higher packing density. Therefore, this paper will contribute to guide an appropriate selection of PSD for better part quality as well as provide more fundamental details of L-PBF additive manufacturing process.

6.2 Nature of Discrete Element Method

6.2.1 Description of Calculation Procedure and Assumptions

All powder particles are assumed as elastic body with different radii and the powder container is treated as rigid walls. DEM uses a Hertz based soft contact approach that allows local overlap at the contact point between particles where contact force is created. The normal contact force is calculated at each time step using the Hertz solution of force versus overclosure. The tangential shear forces are calculated by Coulomb friction law. The contact forces are summed with external force (e.g. gravity) to obtain the total forces and moments exerting on a particle which leads to three translational and three rotational velocity components in Cartesian coordinate system. The total forces and moments for individual particles are calculated at each time step based on force-displacement law. These motions are resolved by Newton's second law to obtain the velocities of individual particles. Finally, the position of particle are updated by a production of velocities and time step size and the computation moves on next time step. The detailed algorithms used in this simulation are given in following section.

For metals unlike ceramic materials, Van der Waals force and electrostatic forces are ignored since Van der Waals is small in comparison with electrical interaction forces as well as the electrostatic force is only true for the particles size smaller than 1 µm [14, 15]. The process conditions and material properties used in this simulation is given in Table 6.1 below.

6.2.2 Algorithms of DEM simulation

The forces and momentum involved in the motion of particles are contact force, rolling resistant, friction force between the particles and particles/processing parts and gravity force. All those are considered in present DEM simulation. Newton's second law applied to calculate the particles' translation and rotational motion is expressed as below

$$\boldsymbol{F}_i = m\ddot{x}_i \qquad \textit{(Translational motion)} \qquad (1)$$

$$\boldsymbol{M}_i = I\ddot{\omega}_i \qquad \textit{(Rotational motion)} \qquad (2)$$

where $\boldsymbol{F}_\mathrm{i}$ and $\boldsymbol{M}_\mathrm{i}$ are the force and momentum acting on random particle A and B calculated from force-displacement law. m is mass of the particle and I is the momentum of inertia of particle. $\ddot{x}_\mathrm{i}$ and $\ddot{\omega}_\mathrm{i}$ are acceleration and angular acceleration, respectively. If the $\ddot{x}_\mathrm{i}$ and $\ddot{\omega}_\mathrm{i}$ are assumed to be constant [16] over time step $t + \Delta t/2$, the velocity are calculated as

$$\dot{x}_i^{t+\Delta t/2} = \dot{x}_i^{t-\Delta t/2} + [\frac{\boldsymbol{F}_i}{m}]\Delta t \qquad (3)$$

$$\dot{\omega}_i^{t+\Delta t/2} = \dot{\omega}_i^{t-\Delta t/2} + [\frac{\boldsymbol{M}_i}{I}]\Delta t \qquad (4)$$

Therefore, the position of particles can be expressed as below:

$$x_i^{t+\Delta t} = x_i^t + \dot{x}_i^{t+\Delta t/2}\Delta t \qquad (5)$$

$$\omega_i^{t+\Delta t} = \omega_i^t + \dot{\omega}_i^{t+\Delta t/2}\Delta t \qquad (6)$$

For the two random particles in contact, particle A and B, when the center to center distance is less than the sum of the two radii, the contact force occurs between two sphere particles.

$$\|\boldsymbol{O_1} + \boldsymbol{O_2}\| < r_1 + r_2 \tag{7}$$

The contact force vector $\boldsymbol{F^c}$ could be decomposed into normal $\boldsymbol{F^{cn}}$ and shear $\boldsymbol{F^{cs}}$ components with respect to contact plane. Those are expressed by equations as below

$$\boldsymbol{F^c} = \boldsymbol{F^{cn}} + \Sigma d\boldsymbol{F^{cs}} \tag{8}$$

$$\boldsymbol{F^{cn}} = k_n u_n \boldsymbol{n} \tag{9}$$

$$d\boldsymbol{F^{cs}} = -k_s \dot{\boldsymbol{u}}_{\boldsymbol{s}} dt \tag{10}$$

where k_n and k_s are elastic normal and shear stiffness at contact. The overlap distance u_n exists only when the equation 7 is satisfied. $\boldsymbol{n}$ is unit normal vector. Relative shear velocity $\dot{\boldsymbol{u}}_{\boldsymbol{s}}$ between two contact particles is used instead of relative shear displacement $\boldsymbol{u_s}$ for better convenience in calculation. To avoid particle size dependency of the material elasticity, macro-scale elastic stiffness E_m is used to define k_n. ν is Poisson's ratio.

$$k_n = 2E_m \frac{r_1 r_2}{r_1 + r_2} \tag{11}$$

$$k_s = \nu k_n \tag{12}$$

Rolling $\boldsymbol{M^r}$ and twisting $\boldsymbol{M^t}$ moments between particles are introduced in order to reproduce rolling resistance $\boldsymbol{M^{res}}$ by the relative particle rotation. The equations associated with the moments are given by following

$$\boldsymbol{M^{res}} = \boldsymbol{M^r} + \boldsymbol{M^t} \tag{13}$$

$$\boldsymbol{M^r} = k_r \boldsymbol{\pi^r} \tag{14}$$

$$\boldsymbol{M^t} = k_t \boldsymbol{\pi^t} \tag{15}$$

where k_r and k_t are rolling and twisting stiffness. Relative rotational vector of sphere particles $\boldsymbol{\pi}$ are decomposed into rolling $\boldsymbol{\pi^r}$ and twisting $\boldsymbol{\pi^t}$ components. The each component of $\boldsymbol{\pi}$ is used to calculate $\boldsymbol{M^r}$ and $\boldsymbol{M^t}$, respectively. Dimensionless coefficient α is adapted to define k_r and k_t.

$$k_{r,t} = \alpha_{r,t} k_s \frac{r_1 r_2}{2} \tag{16}$$

The maximum contact shear force $\boldsymbol{F^{cs}_{max}}$ should be defined because the contact shear force $\boldsymbol{F^{cs}}$ is limited by magnitude of Coulomb friction with inter-particle friction coefficient ϕ. Coulomb friction between particles and particles/processing parts starts working when t $\boldsymbol{F^{cs}}$ is greater than $\boldsymbol{F^{cs}_{max}}$.

$$\boldsymbol{F^{cs}} > \boldsymbol{F^{cs}_{max}} = \boldsymbol{F^{cn}} \tan \phi \tag{17}$$

Gravity along Z-direction is also a force causing motion of particles. Thus, it is summed to contact and friction force to calculate the translation and rotational motion.

$$\boldsymbol{F^{g}} = -mg \tag{18}$$

where $\boldsymbol{F^{g}}$ is gravity force and g is gravitational acceleration. Therefore, the force and momentum resulting in the motion of particles are summed and given by below

$$\boldsymbol{F}_i = \boldsymbol{F^{cn}} + \Sigma d\boldsymbol{F^{cs}} + \boldsymbol{F^{g}} \tag{19}$$

$$\boldsymbol{M}_i = \boldsymbol{M^{res}} + \Sigma(r_i) \times \boldsymbol{F^{cs}} \tag{20}$$

In DEM simulation, the kinetic energy of particles needs to be dissipated since the energy dissipation through friction damping during sliding may not be enough to obtain numerical stability within a reasonable convergence time to quasi-steady state [17, 18]. Hence, a local non-viscous damping [19] is added as a force term to equation 1 so that the equation is rewritten as below

$$\boldsymbol{F}_i + \boldsymbol{F}_i^{\boldsymbol{d}} = m\ddot{x}_i \tag{21}$$

$$\boldsymbol{F}_i^{\boldsymbol{d}} = -\Omega sgn(\dot{x}_i^{t})|\boldsymbol{F}_i| \tag{22}$$

where $\boldsymbol{F}_{\mathrm{i}}^{\boldsymbol{d}}$ and Ω are damping force and coefficient of damping, respectively. The sgn$(\cdot)$ is positive for $(\cdot) > 0$ and vice versa.

Table 6.1 Process conditions for particle packing simulation

Parameter	Symbol	Value
Particle size	r	5 μm -35 μm
Particle density	ρ	8.19×10^{-9} ton/mm^3
Elastic stiffness	E_m	2.0×10^5 N/mm^2
Poisson’s ratio	ν	0.3
Friction coefficient of particle	ϕ_p	0.577
Friction coefficient of system part	ϕ_s	0.176
Rolling coefficient	α_r	0.2
Twisting coefficient	α_t	0.2
Damping coefficient	Ω	0.75
Gravity	g	-9810 mm/s^2

6.3. Result and Discussion

This study utilizes DEM to simulate the movement of particles and interactions between particles-particles and particles-walls. In Figure 6.1(a), individual particles are initially generated within a prescribed imaginary box by random number generator. The particle radius is in the range of 2.5 μm to 35 μm. The initial position of particles is designated by X, Y, and Z coordinate of their centers and radii without overlapping with one another. Then, they fall down onto the ground due to gravity and bounce back from it. Meanwhile, the collision also occurs between particles. Once the particles are settled down in Figure 6.1(b), the gravity in – Z direction is flipped to + Z direction Figure 6.1(c) and flipped back to –Z direction Figure 6.1(d). The flipping of gravity is repeated three times to reproduce a shaking event of particles. In Figure 6.1(e), the ceiling plate falls downward and compresses the particles. This compression leads to an additional increase of packing density through particle rearrangement. After the compaction, the ceiling is released and the particles recovers the shape of packing due to elasticity.

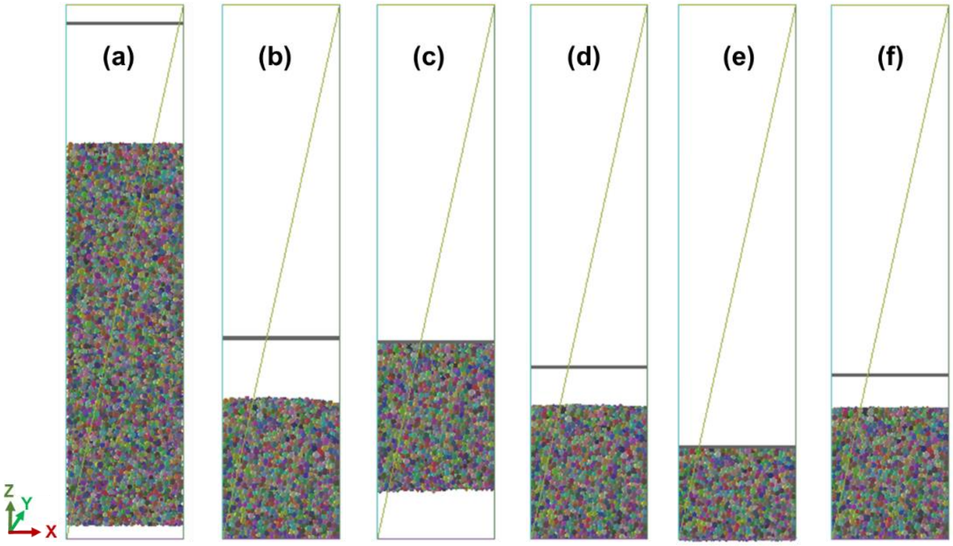

Figure 6.1 Sequence of particle packing: (a) an Initial state of particles (b) settled state after particle falling (c) gravity flipping to +Z direction (d) gravity back to –Z direction (e) compaction of particles (f) resilience of particles

Density scaling method is a frequently used in DEM simulations to reduce computation time [20, 21]. Since DEM is explicit dynamic simulation and thus the maximum time step proportionally increases with the square root of particle density, significantly long convergence time is required for the system to reach the equilibrium status. It is reported that the long time issue is attribute to the small particle density comparing to the relatively large stiffness of the particle [20]. Therefore, the detailed analysis of the sensitivity of simulation is performed to input parameters: particle density, damping, rolling and twisting coefficient listed in Table 6.1. The packing density here is obtained by calculating the ratio of total sphere volume and the box volume filled with spheres. Additionally, a special type of packing density called voxel packing is used to remove the wall effect on packing density. It calculates only the volume of spheres in a specified imaginary box. Thus, it properly excludes a part of spheres which is not in the imaginary box volume. The result in Figure 6.2(a) shows that mass density begins to converge from the density order of 1.0E-2 ton/mm^3 and remains constant at the order of 1.0E-3 ton/mm^3. It concludes that any values less than 1.0E-3 ton/mm^3 can provides the constant values of packing density for both normal packing and voxel packing in this DEM simulation. Also, the coefficient analysis of damping, rolling and twisting in Figure 6.2(b) shows that the packing density is almost independent with the +- 20 % parameter variations.

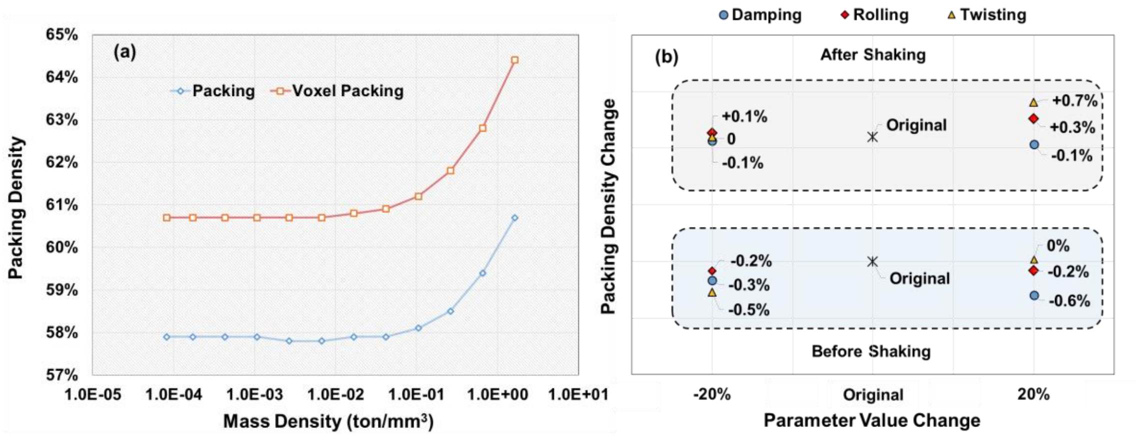

Figure 6.2 Sensitivity analysis of (a) packing density and mass density and (b) damping, rolling and twisting coefficient (-20% vs. original vs. +20%)

Powder particles for L-PBF should be present in a certain range of distribution. Typically, the mean radius of metal particles is in-between 10 µm and 40 µm [13]. However, the distribution is not only non-uniform but also asymmetric [4, 13, 22]. Figure 6.3 presents cumulative size frequency and PSD histograms for positively skewed (type1) and Gaussian like distribution (type2). The plots are simulated from the actual experimental powder distributions [23]. By comparison of the histograms, the asymmetric particle distribution is explicitly shown at the identical radius range of 2.5 µm to 35 µm. Type 1 exhibits higher fraction of fine particles than type 2. Mean radius is approximately 8 µm and 15 µm for type 1 and type 2, respectively. The fraction of fine particles is important in packing density since fine particles particularly play important role in space filling. The details of the role will be discussed later.

DEM generated particles are presented in Figure 6.4 to show the influence of different PSDs on deposit layer thickness. As expected, type 1 produces approximately half thickness of type 2's since it contains significantly more fine particles. As a result, twice more particles is required to make a same deposit thickness.

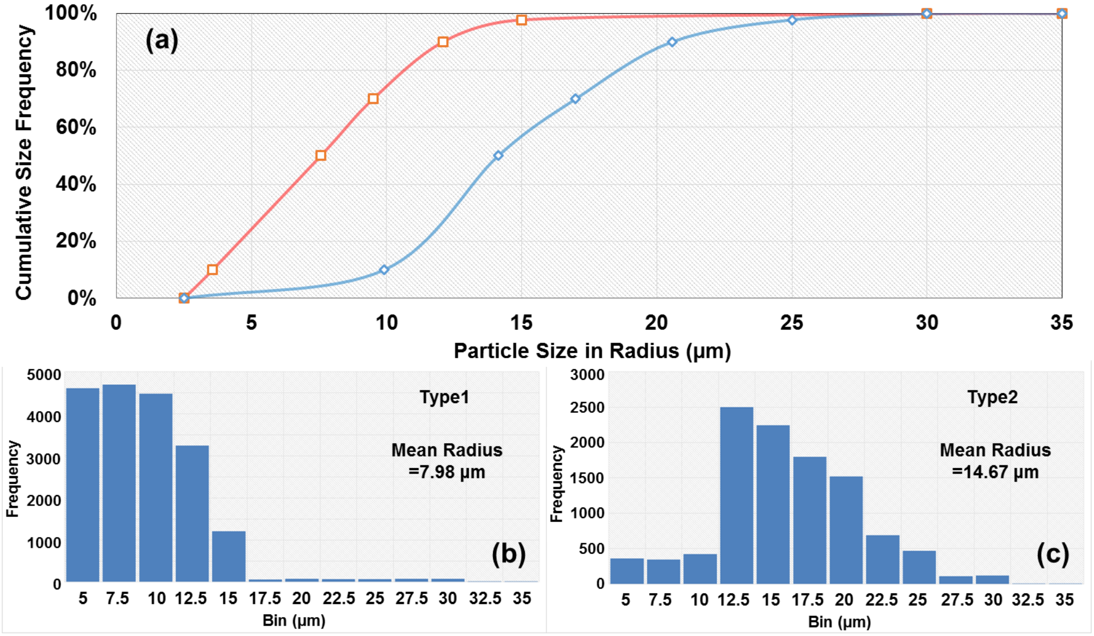

Figure 6.3 Cumulative size frequency (a) and simulated histograms for (b) positively skewed distribution and (c) Gaussian like distribution, Mean radius is approximately 8 μm for type 1 and 15 μm for type 2.

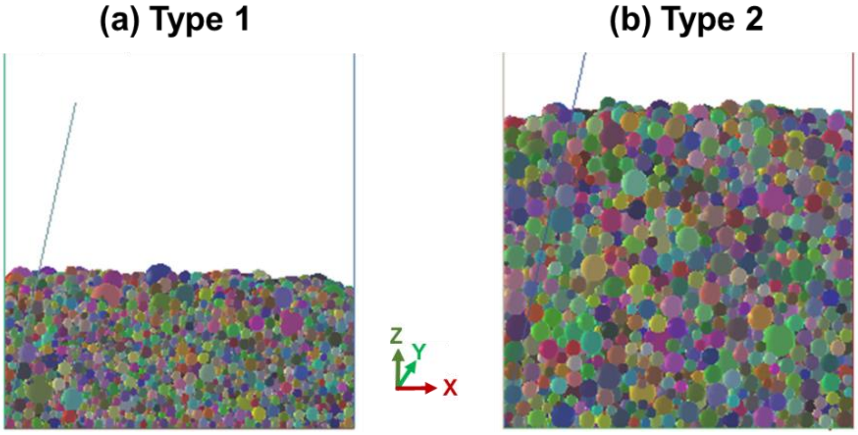

Figure 6.4 (a) Layer thickness: 0.330 mm, 21218 particles (b) Layer thickness: 0.662 mm, 9816 particles

The results of packing simulations from type 1 and type 2 distribution are shown in Figure 6.5 to validate the accuracy of the simulation. The simulated density of normal packing (denoted as blue colored symbols) is 60.94% for type 1 and 58.68% for type 2. The density values are in the experimental error range [23] and therefore the model accuracy is well confirmed. Notice that experimental PSDs for type 1 and 2 are used as an input for present DEM simulations. Higher packing density is observed in type 1 for both the normal packing and voxel packing than type 2. The reason seems that more amount of fine particles come into the void space and fill it more in type 1. Voxel packing shows about 3.5% higher density than that in normal packing. Previous literature addressed that the platform wall can cause an additional amount of porosity in the powder bed [15].Thus, the removal of platform effect from the powder bed leads to increase of the density for voxel packing.

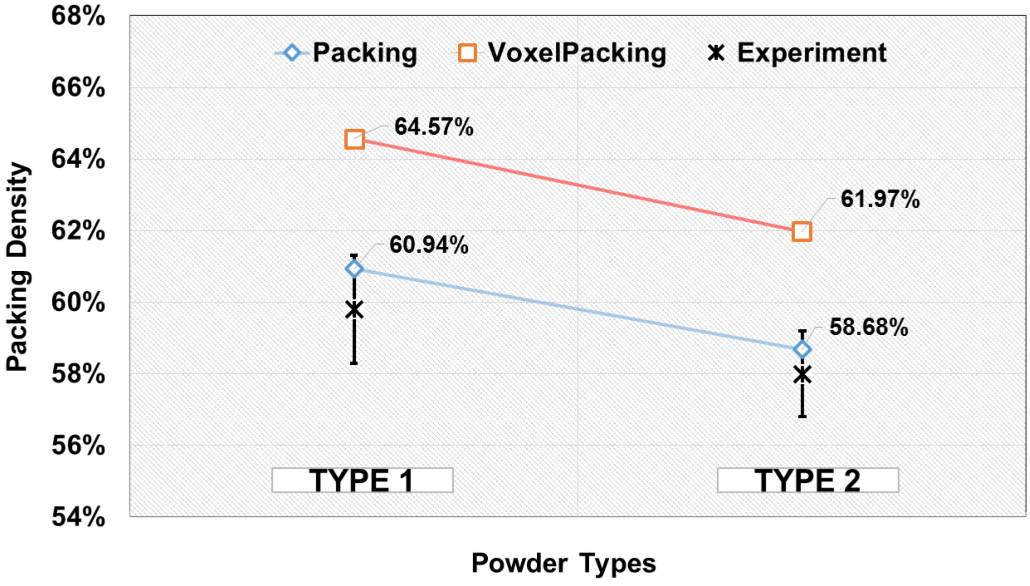

Figure 6.5 Validation of simulation in packing density

Particle packing with equal size is often useful because of its simplicity of creation and the size difference may not be significant in certain cases. Three different particle radius 8 µm, 15 µm and 22.5 µm are simulated and the results are displayed in Figure 6.6. For both normal packing and voxel packing, the packing density decreases with increase of the particle size. However, the change at normal packing is a little which is about 0.8%. Therefore, it reveals that size decrease without distribution is not effective to increase the packing density.

Two different Gaussian distributions are shown in Figure 6.7. Gaussian with 10 µm to 20 µm range displays narrower distribution range than Gaussian with 5 µm to 25 µm range. Both distributions have same 15 µm mean radius. It is observed that the broader range distribution results in increase of density but the increase is less than approximately 0.6%. Thus, the size of deviation range has a little effect on density increase.

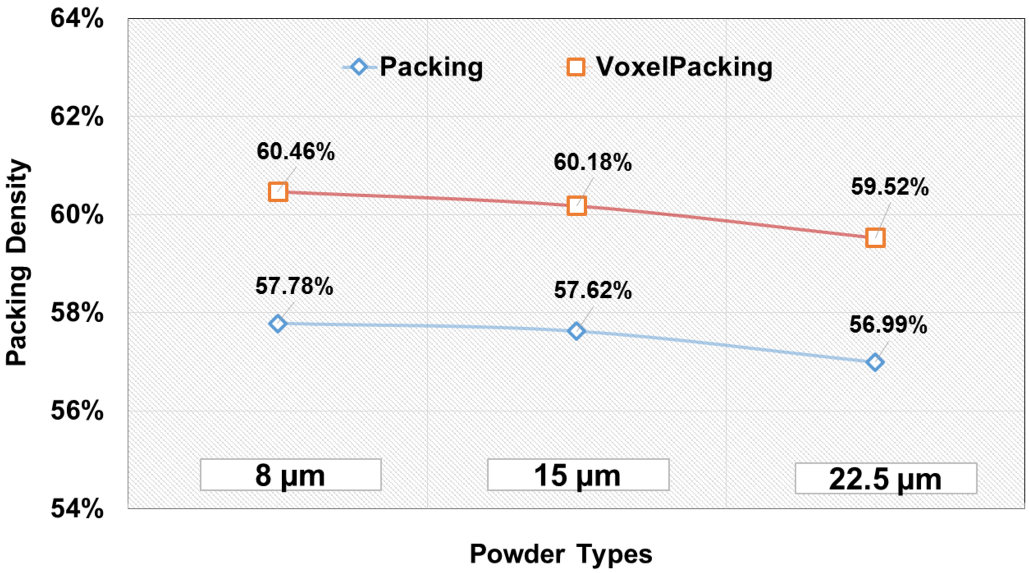

Figure 6.6 Equal size distribution

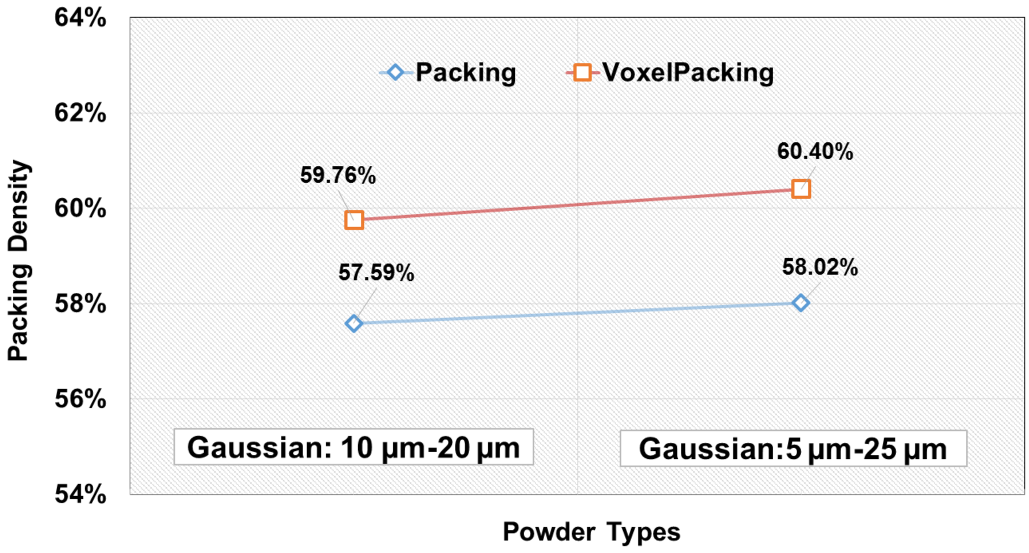

Figure 6.7 Two different Gaussian distributions with narrower (10 µm to 20 µm) and broader (5 µm to 25 µm) deviation, mean 15 µm

Figure 6.8 presents three different asymmetric particle distributions: negatively skewed (Nskewed), positively skewed (type 1) and Gaussian like distribution (type 2). The Nskewed distribution is artificially created (but it's feasible) to make comparison to real cases of type 1 and type 2. Unlike equal size and Gaussian distribution cases, the density significantly varies with the particles distribution change. For normal packing, the highest density 60.94% is obtained at type 1 while the lowest density 56.78% is obtained at Nskewed distribution. It seems more fraction of fine particles primality contributes to increasing the packing density.

The role of fine particles is investigated by comparison of equal size and asymmetric distributions that have same 8 µm, 15 µm and 22.5 µm in mean radius. At overall trend, the asymmetric distributions show higher packing density than equal size distributions even though the three types of distribution have same mean radius size 8 µm, 15 µm and 22.5 µm as equal size distribution. For instance, type 1 shows 3.2% higher density than equal size 8 µm in normal packing. The density difference becomes larger at voxel packing. As the mean radius increases to 22.5 µm, interestingly, the density difference between equal size and asymmetric distributions is gradually reduced and vanished. It reduces from 3.2% at 8 µm to 0.21% at 22.5 µm. The result shows that higher fraction of fine particles is more effectively leading to higher packing density.

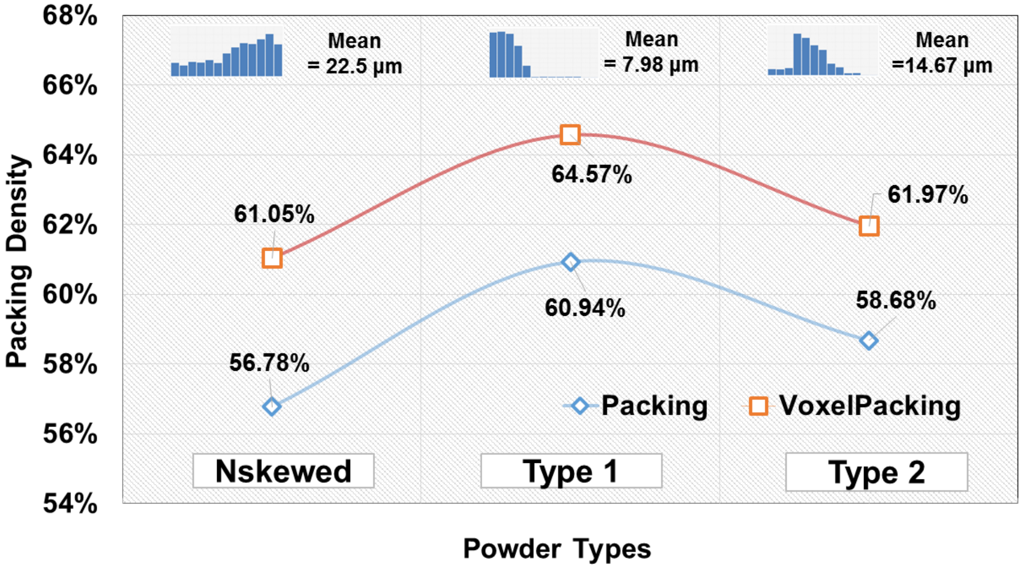

Figure 6.8 Packing density variation with three asymmetric distributions: negatively skewed distribution, type 1 and type 2

A criteria of D_{90}/D_{10} ratio is adopted to quantitatively examine the effect of fine and coarse particles on the packing density [15, 22]. D_{10} and D_{90} represent the value of particle diameter at 10% and 90% in the cumulative distribution. Thus, D_{90}/D_{10} indicates the ratio of coarse and fine particles in the different particle distributions. The correlation of packing density with D_{90}/D_{10} ratio is shown in Table 6.2. D_{90}/D_{10} reflects the variation trend of density well. The density is the lowest at minimum ratio D_{90}/D_{10}= 1.39 in Nskewed distribution and the highest at the maximum ratio D_{90}/D_{10}= 3.39 in type 1. From the result, it is said that a sufficient amount of fine particles primarily leads to higher packing density since it effectively fills the space between coarse particles.

Table 6.2 Correlation of packing density with D_{90}/D_{10} ratio

Powder Types	**Negatively Skewed**	**Type 1**	**Type 2**
Packing Density (%)	56.78	60.94	58.68
D_{90}/D_{10}	1.39	3.39	2.07

6.4 Summary and conclusions

In DEM simulation, the contact force and momentums for individual particles are resolved by Newton's second law to obtain the velocities and positions of them. The simulation used PSD as an input parameter and predicted the comparable packing density with experimental value. More simulations were conducted with different PSDs of equal size, Gaussian and asymmetric distributions to investigate the effect of PSD on packing density. From the investigation of a variety PSD cases, the following conclusions are drawn:

- For equal size distributions with 8 μm, 15 μm and 22.5 μm radius particle. The packing density increase seems not to be effective since the density variation is less than 0.8% in the equal size distributions.
- In comparison of Gaussian size distributions with narrow (10 μm to 20 μm) and broad (5 μm to 25 μm) deviation, the density increase is less than approximately 0.6%. Thus, the size range deviation has little effect on density increase.
- For asymmetric distribution with negatively skewed (Nskewed), positively skewed (type 1) and Gaussian like distribution (type 2), unlike equal size and Gaussian distributions, the packing density considerably varied with the asymmetric PSDs. The highest density 60.94% is obtained in type 1 whereas the lowest 56.78 is obtained in Nskewed. It seems higher fraction of fine particles is a key factor increasing the packing density.
- The role of fine particles is quantitatively examined with the ratio of D_{90}/D_{10}. The density is the highest (=60.94%) at the maximum ratio of D_{90}/D_{10} (=3.39) while it is the lowest (=56.78%) at the minimum ration of D_{90}/D_{10} (=1.39).
- Therefore, fine and asymmetric PSD is recommended to obtain higher packing density.

Also, DEM enables complete description of the random packing structure that is important information for 3-D heat transfer and fluid flow simulation because the packing structure is the starting point of the geometry setting. Therefore, the DEM simulation provides not only insight into the motion of powder particles and process parameters related to particle packing density but also a possible application of this simulation to the further 3-D heat transfer and fluid flow simulation in L-PBF.

6.5 Acknowledgement

The authors would like to acknowledge the grant from Office of Naval Research (ONR), Award No. N00014-14-1-0688, in support of the research.

6.6 References

1. Zhou JH, Zhang YW, Chen JK (2009) Numerical simulation of random packing of spherical particles for powder-based additive manufacturing. Journal of Manufacturing Science and Engineering 131(3):031004.

2. Sugavaneswaran M, Arumaikkannu G (2014) Modelling for randomly oriented multi material additive manufacturing component and its fabrication. Materials & Design 54(0):779-785.

3. Körner C, Attar E, Heinl P (2011) Mesoscopic simulation of selective beam melting processes. Journal of Materials Processing Technology 211(6):978-987.

4. Liu B, Wildman R, Tuck C, Ashcroft I, Hague R (2011) Investigation the effect of particle size distribution on processing parameters optimisation in selective laser melting process. In Proceedings of Solid Freeform Fabrication Symposium, Austin:227-238.

5. Li Y, Gu D (2014) Parametric analysis of thermal behavior during selective laser melting additive manufacturing of aluminum alloy powder. Materials & Design 63:856-867.

6. He D, Ekere NN, Cai L (1999) Computer simulation of random packing of unequal particles. Physical Review E 60(6):7098-7104.

7. Yang RY, Zou RP, Yu AB (2000) Computer simulation of the packing of fine particles. Physical Review E 62(3):3900-3908.

8. Shi Y, Zhang YW (2008) Simulation of random packing of spherical particles with different size distributions. Applied Physics A: Materials Science & Processing 92(3):621-626.

9. Jia T, Zhang YW, Chen JK (2011) Dynamic simulation of particle packing with different size distributions. Journal of Manufacturing Science and Engineering 133(2):4.

10. Jia T, Zhang YW, Chen JK (2012) Simulation of granular packing of particles with different size distributions. Computational Materials Science 51(1):172-180.

11. Dou X, Mao YJ, Zhang YW (2014) Effects of contact force model and size distribution on microsized granular packing. Journal of Manufacturing Science and Engineering: ASME 136(2):9.

12. Cheng YF, Guo SJ, Lai HY (2000) Dynamic simulation of random packing of spherical particles. Powder Technology 107(1-2):123-130.

13. Schmid M, Amado A, Wegener K (2014) Materials perspective of polymers for additive manufacturing with selective laser sintering. Journal of Materials Research 29:1824-1832.

14. Uskoković D, Exner HE (1990) The kinetics of contact formation during sintering by diffusion mechanisms. In: Sōmiya S, Moriyoshi Y (eds) Sintering key papers. Springer Netherlands, pp 111-146. doi:10.1007/978-94-009-0741-6_8

15. Karapatis NP, Egger G, Gygax PE, Glardon R (1999) Optimization of powder layer density in selective laser sintering. In Proceedings of Solid Freeform Fabrication Symposium, Austin:255-263.

16. Chareyre B, Villard P (2005) Dynamic spar elements and discrete element methods in two dimensions for the modeling of soil-inclusion problems. Journal of Engineering Mechanics 131(7):689-698.

17. Cundall PA, Strack OD (1979) A discrete numerical model for granular assemblies. Geotechnique 29(1):47-65.

18. Cheng Y, Guo S, Lai H (2000) Dynamic simulation of random packing of spherical particles. Powder Technology 107(1):123-130.
19. Shiu WJ, Donze FV, Daudeville L (2008) Compaction process in concrete during missile impact: A dem analysis. Computers and Concrete 5(4):329-342.

20. O'Sullivan C, Cui L, Bray JD (2004) Three-dimensional discrete element simulations of direct shear tests. In Proceedings of the 2nd International PFC Symposium, Kyoto:373-382.

21. Morgan JK, Boettcher MS (1999) Numerical simulations of granular shear zones using the distinct element method: 1. Shear zone kinematics and the micromechanics of localization. Journal of Geophysical Research: Solid Earth (1978–2012) 104(B2):2703-2719.

22. Spierings A, Levy G (2009) Comparison of density of stainless steel 316l parts produced with selective laser melting using different powder grades. In Proceedings of Solid Freeform Fabrication Symposium, Austin:342-353.

23. Spierings A, Herres N, Levy G (2011) Influence of the particle size distribution on surface quality and mechanical properties in am steel parts. Rapid Prototyping Journal 17(3):195-202.

Chapter 7: Mesoscopic Simulation of Heat Transfer and Fluid Flow in Laser Powder Bed Additive Manufacturing

7.1 Introduction

Laser-powder bed fusion (L-PBF) additive manufacturing involves complex physical processes such as beam absorptance, heat transfer and molten metal flow, phase transformation, and thermal stress and distortion; all these factors influence the final build quality and properties [1,2]. Absorbed beam energy in the powder bed melts the particles and causes strong fluid flow in the molten pool which is driven by surface tension gradient (or Marangoni shear stress). Because of the highly dynamic fluid flow, the shape of the molten pool surface, which is a free surface, is constantly evolving. The above physics is similar to that in laser beam welding. However, the powder particles in L-PBF (as opposed to a solid metal in laser welding) add significant complexity to the process. In particular, the absorptance of laser beam depends on particle size distribution and particle arrangement (or stack-up). The weld pool shape as well as the heat transfer and fluid flow are also significantly affected by local arrangement of powder particles in the powder bed which can vary from location to location due to randomness of the particles size and distribution. In other words, the heat dissipation can become anisotropic, which in turn, can alter local temperature gradient and fluid flow field.

Give the extremely wide length scale of L-PBF physics, numerical models of L-PBF process can be approximately divided into two groups. The first group deals with phenomena at the engineering scale (e.g., mesh size on the order of 1 mm). For instance, finite element method (FEM) based models are employed to describe the evolution of temperature, stress and displacement fields during L-PBF [3, 4]. Obviously, given the coarse mesh resolution, melting of powder particles in individual tracks are not simulated in the FEM based models, although those models can easily study the global variation of temperature, residual stress and distortion in the entire part. The second group comprises meso-scale models capable of resolving individual powder particles (e.g., mesh size on the order of 1 µm). An example of such meso-scale models is the two dimensional (2D) heat transfer and fluid flow model based on lattice Boltzmann method (LBM) developed by Korner et al. for single layer [5] and multiple layers [1]. The free surface was tracked using the volume of fluid method (VOF). The 2-D model was used to create a process map which showed that the molten pool characteristics were considerably affected by laser scanning speed, beam power and powder packing density. Three dimensional (3D) model based on LBM was developed by Khairallah and Anderson [6] and by Gurtler et al. [7]. Consideration of particle size distribution and stack-up varied from model to model from simple mono-size [7] to random size distribution [5]. It is noted that LBM is a newer method than the conventional finite difference/volume method to solve the governing transport equations. Even at a mesh (cell) size of 3 µm, the LBM is computationally demanding, which can easily consume on the order of 10,000 CPU hours. Moreover, it can be difficult to consider some important temperature dependent material properties such as surface tension gradient and viscosity which can influence heat transfer and fluid flow behavior.

The present paper uses two models in sequence. The first model is a powder particle packing model based on discrete element method (DEM). It provides the particle stack-up information (e.g., locations and radii of individual particles). Such information is then input into the second model, which is a high resolution but computationally less demanding, heat transfer and fluid flow model based on the finite difference method and VOF. This 3D transient model is applied to understand the correlation of powder packing characteristics, process parameters, and molten pool dynamics to the resultant surface quality (e.g., balling defect).

7.2 Numerical modeling approach

7.2.1. Discrete element method simulation of powder packing

DEM is a well-established numerical method that is capable of simulating the motion of a large number of individual particles including contact interactions between particles/particles and particles/walls. In the present study, a powder packing model is developed based on Yade, an open source software package for DEM. For brevity, only salient features of the DEM model are described below and the details are available in Yade documentation [8].

The powder particles are simplified as elastic spheres with different radii and the powder container is treated as rigid walls. Each particle has six velocity components: three translational and three rotational in the x, y and z axis of a Cartesian coordinate system. To efficiently track the large number of contact interactions, a Hertz based soft-contact formula is used which permits a finite overclosure locally at the contact point between particles. The normal contact force is then calculated using the Hertz solution of force versus overclosure. The tangential forces are calculated using the Coulomb friction law. These contact forces are summed together with the gravitational force to obtain the total forces and moments exerting on a particle. The solution process in DEM is the following. At each time step, the total forces and moments for individual particles are calculated based on the procedure above. Next, the velocities are calculated by solving Newton’s second law of motion. Finally, the particle positions are updated with distances traveled (i.e., multiplication of velocities and time step size) and the calculation continues to the next time step.

To study the effect of particle size on the molten pool dynamics, two particle size distributions (PSDs) are considered, as shown in Figure 7.1. Both PSDs have the same range of particle radii from 10 μm (minimum) to 20 μm (maximum). Figure 7.1(a) and 7.1(b) show a positively skewed PSD (abbreviated as PSD+) with a mean radius of 12.7 μm and a negatively skewed PSD (abbreviated as PSD-) with a mean radius of 17.3 μm, respectively. As shown in Figure 7.1(c), PSD+ contains a higher fraction of small particles. For example, 90% of the particles in PSD+ have a radius less than 14 μm, while that fraction is only 8% in PSD-.

The spherical particles considered in the present DEM simulation are made of INCONEL® Alloy 718 (IN718), a nickel alloy with good high-temperature strength. The key material properties for DEM include Young’s modulus = 195 GPa, and friction coefficient between particles = 0.3. In the DEM simulation, a cloud of particles with the given PSD is first generated inside a rectangular box without any overclosure among particles. The particles then fall down onto the floor of the containing box by gravity and eventually settled down. In the DEM, the packed particles are then subject to a roller with a clearance of 50 µm to create a nominally 50-µm-thick layer. The positions (i.e., x, y and z coordinates) and radii of the stabilized particle are then exported and used to define the initial geometry in the subsequent heat transfer and fluid flow model described in the following section.

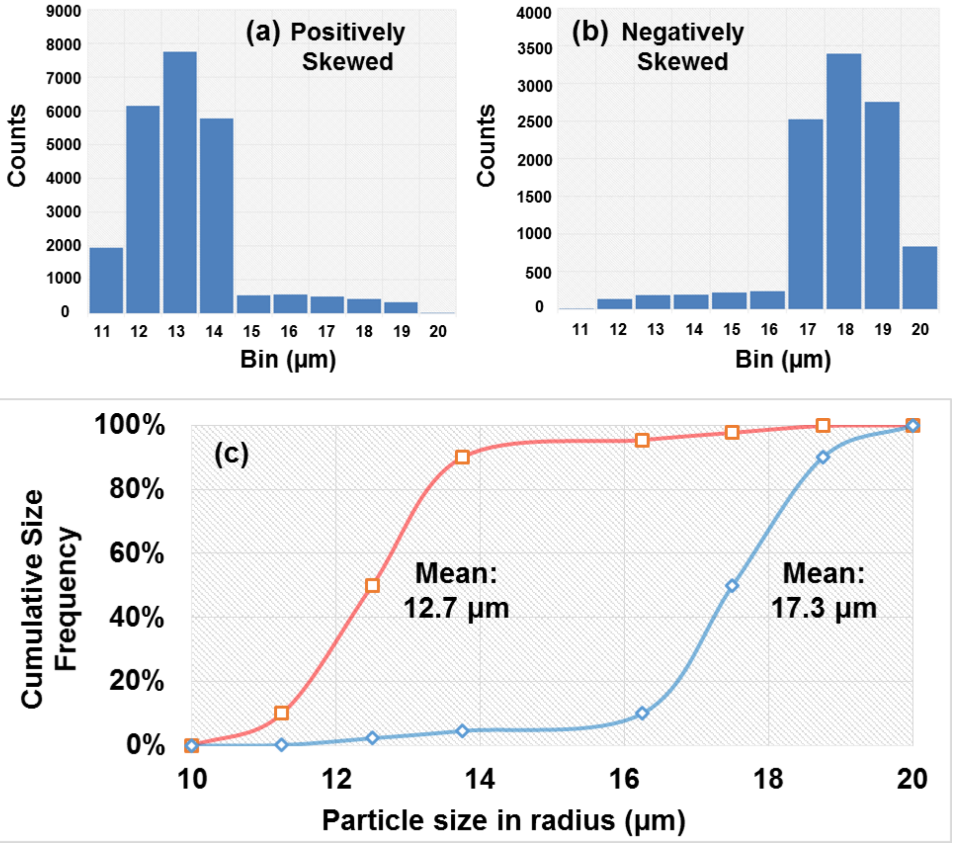

Figure 7.1 Histograms of (a) positively skewed PSD, (b) negatively skewed PSD, and (c) cumulative size frequency for the two PSDs in (a) and (b).

7.2.2 Governing equations for heat transfer and fluid flow

The L-PBF process simulation is preformed based on numerical solution of mass, energy and momentum conservation equations, which are given in equations (1) through (3), respectively.

Mass: $$\nabla \cdot \vec{v} = 0. \tag{1}$$

Energy: $$\frac{\partial h}{\partial t} + (\vec{v} \cdot \nabla)h = \frac{1}{\rho}(\nabla \cdot \lambda \nabla T). \tag{2}$$

Momentum: $$\frac{\partial \vec{v}}{\partial t} + (\vec{v} \cdot \nabla)\vec{v} = -\frac{1}{\rho}\nabla P + \mu \nabla^2 \vec{v} + \vec{g}[1 - \beta(T - T_m)]. \tag{3}$$

where $\vec{v}$ is molten metal velocity, h is enthalpy, t is time, ρ is fluid density, T is temperature, λ is thermal conductivity, P is hydrodynamic pressure, μ is viscosity, g is gravitational acceleration in z direction, β is coefficient of thermal expansion, and T_m is melting temperature of material. In equations (1) and (3), the fluid is assumed to be incompressible and Newtonian with laminar flow.

The position of molten pool surface is not known *a priori*. The VOF method is used to track the position and shape of the molten pool surface (free surface). It solves a scalar transportation equation for the volume fraction of fluid in a cell (F) as:

VOF: $$\frac{\partial F}{\partial t} + \nabla \cdot (\vec{v}F) = 0. \tag{4}$$

A cell is void when $F = 0$, and completely occupied by the fluid when $F = 1$. When the value of F is between 0 and 1, an interface between the fluid and void exists in the cell. The conversation equations (1) through (4) are discretized and then solved using the finite difference method in Flow-3D, a commercial computational fluid dynamics (CFD) code. Details of the discretization and solution steps are available in the literature [9, 10].

7.2.3 Computational domain, boundary conditions and materials properties

The transient simulation is performed in a 3D computation domain with 1000 μm (length), 270 μm (width) and 190 μm (height), as shown in Figure 7.2. The domain comprises a 50-μm-thick layer of powder particles laying on a 90-μm-thick substrate. The reminder of the domain is initially filled with void. The powder layer geometry is initialized using the results from the previous DEM simulation. To maximize spatial resolution while reducing the total number of cells, biased meshing is utilized where the mesh size reduces continuously from 9 μm to 3 μm in the substrate toward the substrate/powder layer interface. The mesh size is kept constant 3 μm in the powder layer and the void above it. The total number of cells is 1.43 million.

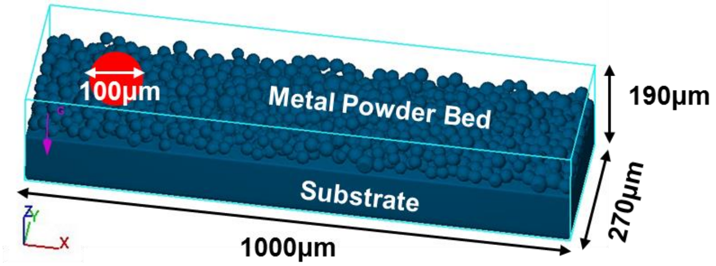

Figure 7.2 Schematic description of computational domain.

The primary boundary condition for solving the energy conservation equation is the heat input from the scanning laser beam. The absorption of laser energy by the powder particles is complex. To make the simulation tractable, a prescribed heat flux boundary condition based on Gaussian distribution is imposed on the top surface of the powder layer [11]. For the molten metal fluid flow, the temperature dependent surface tension and the resultant Marangoni shear stress are important driving forces for both the molten metal convection and the evolution of free surface shape. In the present study, the temperature dependency of surface tension is included with an improved surface tension model available in Flow-3D [9].

The temperature dependent thermos-physical properties of IN718 including density, thermal conductivity, specific heat and liquid metal viscosity are plotted in Figure 7.3 [9]. Additional thermos-physical properties and L-PBF processing parameters are summarized in Table 7.1 [9].

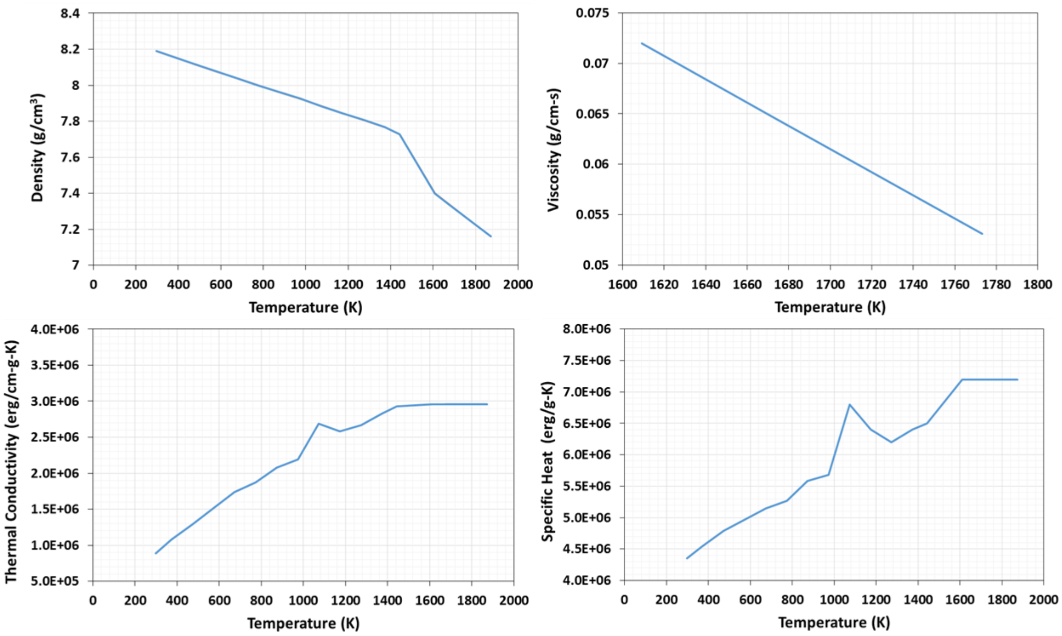

Figure 7.3 Thermos-physical properties of IN718. Note 1 erg = 10^{-7} joules.

Table 7.1 Additional thermos-physical properties of IN718 and L-PBF processing parameters.

Property and Parameters	**Value [units]**
Liquidus	1608.15 [K]
Solidus	1523.15 [K]
Surface Tension	1882 [g/s^2]
Temperature Coefficient of Surface Tension	-0.1 [g/s^2 K]
Laser Beam Spot Size	100 [μm]
Laser Power	150 and 200 [W]
Scanning Speed	1.1 and 2.3 [m/s]
Powder Packing Density	38 and 45 [%]

As described previously, even for the fairly small computational domain shown in Figure 7.2, there are more than 1 million cells in order to accurately resolve the individual particles. At this level of resolution, the transient simulation of about 600-microseconds-long L-PBF takes approximately 40 hours clock time to finish in a moderately powerful workstation with Intel® Xeon® Processor E5335 and 4 GB RAM. Compared with thousands of CPU hours needed by LBM, the present model based on finite difference method and VOF, incorporating temperature-dependent surface tension, is more computationally efficient. Obviously, the current domain is limited to simulating a single linear track of laser melting. To consider more complex laser scanning patterns and multilayers, the present model will need to be scaled up by utilizing distributed memory parallel computing in the future. Nevertheless, the present model allows the study of the correlation of powder packing characteristics, process parameters, and molten pool dynamics to the resultant surface quality, as discussed in the following.

7.3 Result and discussion

7.3.1 Stack-up of powder particles with different PSDs

Figure 7.4 plots a 3D view of the stack-up of powder particles calculated using the DEM model for those two different PSDs in Figure 7.1. The spherical particles are colored based on their respective radii. As shown in Figure 7.4(a), the 50-µm-thick region filled with particles of PSD+ is made up with two layers of small particles at the majority of locations. This is due to the large fraction of smaller particles in PSD+. On the other hand, the region filled with particles of PSD- is mostly made up with a single layer of larger particles, as shown in Figure 7.4(b). The packing density, defined as the ratio of the occupied volume by the particles to the total volume enclosing all the particles, is about 38% for both PSDs.

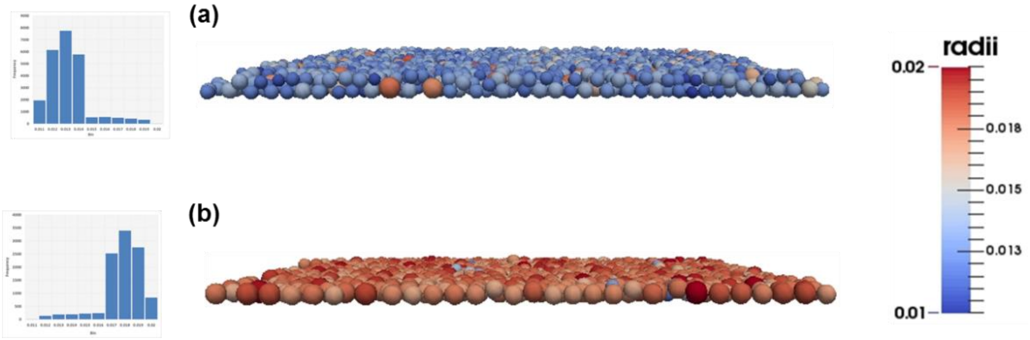

Figure 7.4 Stack-up of spherical particles with different particle size distributions calculated using DEM: (a) PSD+ containing a high fraction of smaller particles, and (b) PSD- containing larger particles. The radii are given in mm.

7.3.2 Fluid flow and molten pool shape

Figure 7.5 plots the longitudinal section view (i.e., a section parallel to the laser travel direction) of temperature and velocity fields in the molten pool at time=55μs. The temperatures are plotted as color contours and the velocities as arrows. The magnitude of the velocity is represented by the length of an arrow. The molten pool boundary is represented by the isotherm at 1608.15 K, which is the liquidus temperature of IN718. As shown to the right side of Figure 7.5, a particle is partially melted into the molten pool. Near the molten pool surface, the molten metal is pulled from the center location directly underneath the laser beam to the rear end of the pool. Such flow pattern is driven by the temperature-dependent surface tension. In other words, the center directly underneath the laser is heated to a higher temperature than the rear end. As a result, the surface tension is lower in the center than the rear end, which drives the molten metal flowing backward near the surface. Such backward flow is strong, resulting in an anticlockwise pattern as the molten metal returns from the rear end to the center inside the pool. Moreover, some of the molten metal pushed to the back flows radially and returns back to the front.

The backward flow of molten metal near the pool surface produces a surface profile that is depressed underneath the laser beam while it forms a hump toward the rear end of the pool. As discussed in the following section, the humped shape can lead to the formation of balling.

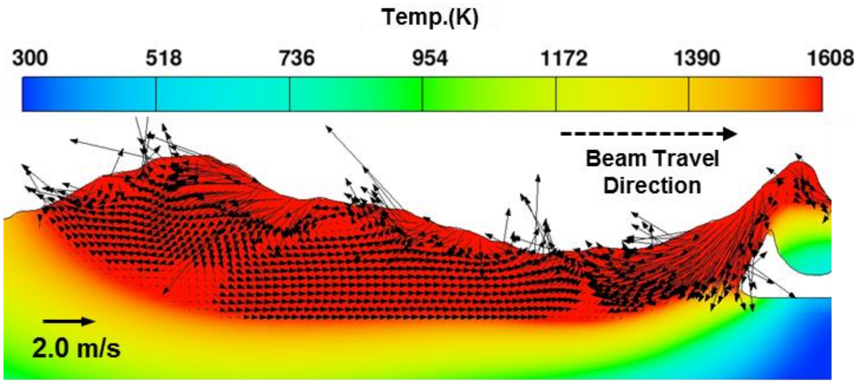

Figure 7.5 Longitudinal section view of heat transfer and fluid flow in the molten pool. The parameters are scanning speed = 1.1m/s, laser power = 150W, packing density = 45%, and PSD+.

7.3.3 Formation of balling defect

Balling is a defect that can occur when the molten pool becomes discontinuous and breaks into separated islands. Using the heat transfer and fluid flow model, it is quantitatively studied the effect of various parameters, which include PSD, scanning speed, laser beam power and powder packing density, on the formation of balling defect in L-PBF. The results are described as follows.

7.3.3.1. Effect of particle size distribution

A 3D view of the molten pool temperature field for the two different PSDs is shown in Figure 7.6. For clarify, the fluid velocities are not plotted. For either PSD, the molten pool is continuous and the balling defect does not occur. On the other hand, the molten pool shape appears smoother for the case with PSD+ in Figure 7.6(a) than that with PSD- in Figure 7.6(b). As discussed previously, PSD+ contains a large fraction of smaller particles. For the same laser energy, smaller particles are more likely to be melted completely due to their smaller volume/mass, whereas larger particles are more likely to be partially melted. As a result, the molten pool formed by partially melted, large particles creates a more corrugated edge. This observed effect of PSD from the simulation results is consistent with the literature data that smaller particles can help reduce the surface roughness [12,13].

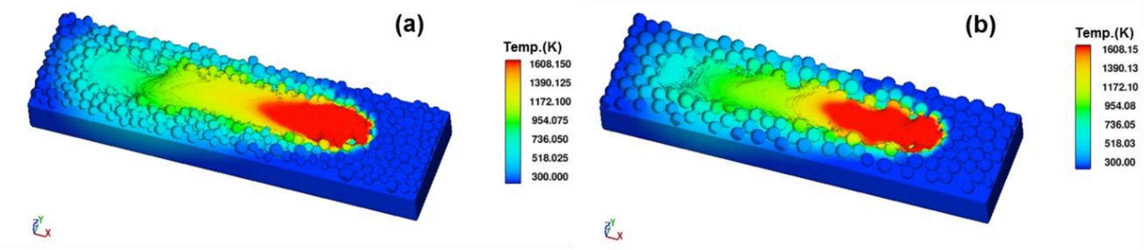

Figure 7.6 Calculated temperature fields showing the molten pool profile for (a) PSD+ and (b) PSD-. The parameters are scanning speed = 1.1 m/s, laser power = 200W, and powder packing density = 38%.

7.3.3.2. Effect of scanning speed

A faster scanning speed without defects is always desirable for higher productivity. However, if the scanning speed is too high, the molten pool may become so elongated that it can break into separate islands. Such formation of balling defect is illustrated in Figure 7.7, for which the processing conditions are the same as those for Figure 7.6(a) except that the scanning speed is increased to 2.3 m/s from 1.1 m/s. As shown in this figure, there is a very shallow melting of the substrate due to the high scanning speed and the resultant low heat input per unit length. Small disconnected islands (or balls) are formed in the trailing end of the molten pool. Such separate islands at the fast scanning speed are in contrast to the continuous, smooth molten pool at the slow scanning speed shown in Figure 7.6(a).

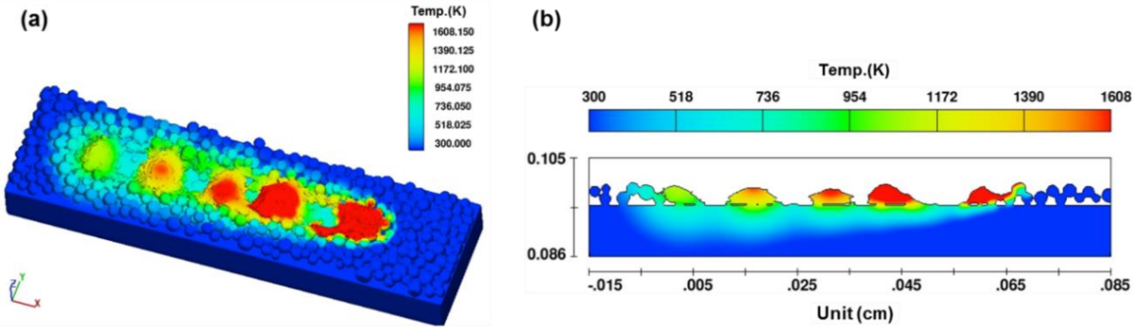

Figure 7.7 (a) 3D view and (b) 2D longitudinal section view of molten pool for the fast scanning speed at 2.3 m/s. All other conditions, i.e., laser power = 200W, powder packing density = 38%, and PSD+, are the same as those in Figure 7.6(a).

A mechanism for forming the disconnected balls in high speed laser melting is attributed to the Rayleigh instability [14]. In particular, it states that the instability is initiated when the length to width ratio of the molten pool is greater than π. As the laser scanning speed increases, the molten pool length increases while the pool width would decrease slightly. Hence, the length to width ratio increases with faster scanning speed, which leads to a larger instability. Other factors for formation of balling defect in L-PBF include the local powder particle arrangement, wetting, Marangoni flow and gravity [5]. To further understand the formation of balling defect in L-PBF, the transient evolution of molten pool profile is illustrated in Figure 7.8. As shown in this series of images, the primary molten pool directly underneath the laser beam is not stable and the rear end quickly breaks apart from the front to form a separate island. It is interesting to observe that the separation initiates from a void in the middle of the molten pool, as shown in Figure 7.8(c). This void expands as the laser continues to travel forward, eventually breaking the molten pool into two parts, as shown in Figures 7.8(e) and 7.8(f). The formation of void and its expansion are likely caused by the strong backward flow driven by the surface tension described previously. The length to width ratio for the molten pool shown in Figure 7.8 is approximately 2.3, which is lower than the threshold ratio for Rayleigh instability. This indicates that the relatively low packing density (when compared to a solid) could increase the likeliness of forming the balling defect.

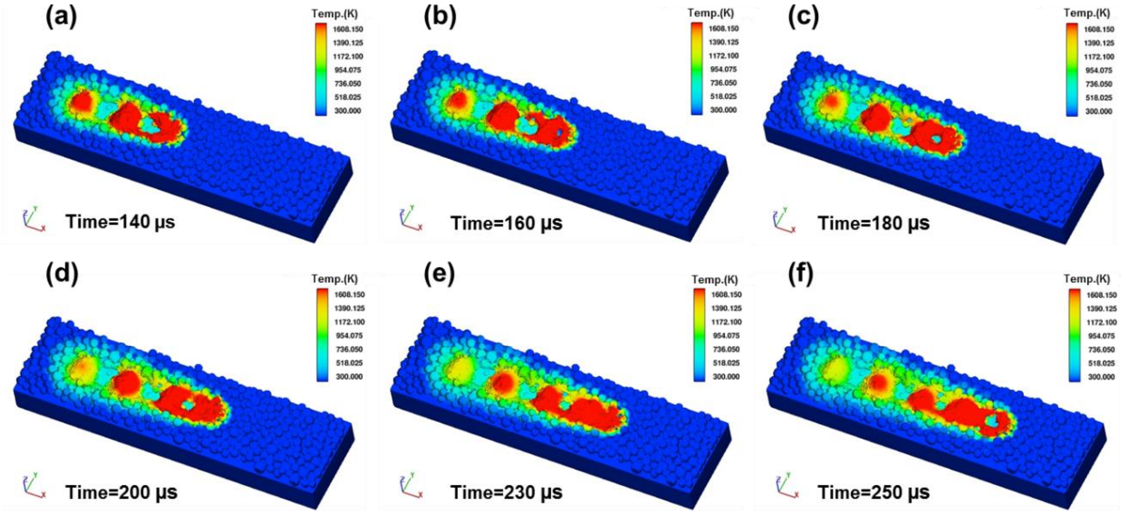

Figure 7.8 Evolution of molten pool profile illustrating the formation of balling defect.

7.3.3.3 Effect of laser power

From the perspective of heat input per unit length, a faster travel speed is equivalent to a lower laser power. To examine the effect of lowering the laser power on the formation of balling defect, a laser power of 150W is considered while all other conditions are kept the same as those in Figure 7.6(a). As shown in Figure 7.9, a reduction in the laser power indeed results in a discontinuous molten pool and the formation of balling defect. On the contrary, a higher laser power is desirable to minimize the balling defect when faster travel speed is used. However, the literature data has shown an overly high laser power can worsen the surface finish [13]. The effect of high laser power on surface roughness will be the subject of a future study.

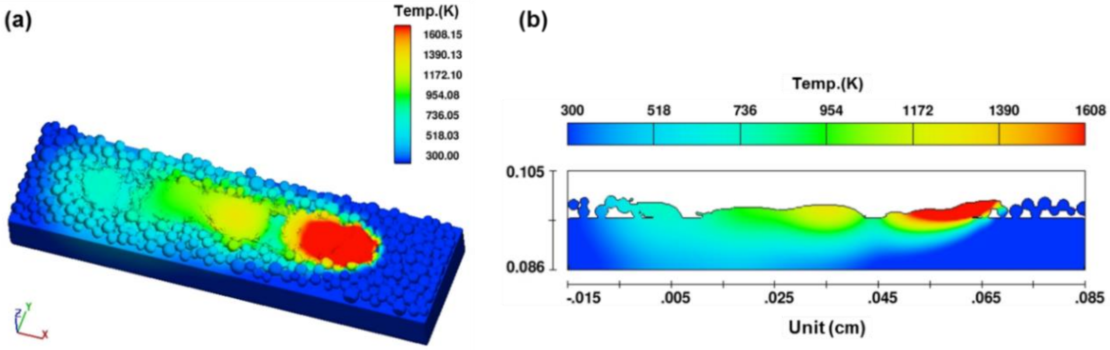

Figure 7.9 (a) 3D view and (b) 2D longitudinal section view of molten pool for the low laser power of 150 W. All other conditions, i.e., scanning speed = 1.1 m/s, powder packing density = 38%, and PSD+, are the same as those in Figure 7.6(a).

7.3.3.4 Effect of packing density

The last factor to be examined is the powder packing density. Literature data has shown that a higher powder packing density is desirable to produce dense parts with better surface finish [1,15]. Figure 7.10 shows the molten pool profile for a packing density of 45%. All other parameters are the same as those in Figure 7.9. As shown in Figure 7.10, an increase in packing density from 38% to 45% eliminates the discontinuous molten pool and produces a smoother surface contour. As discussed previously, the balling defect initiates from a void at the center of the molten pool (see Figure 7.8). Higher packing density is expected to reduce the formation of such void due to a larger mass to fill any new void. In addition, it is reported that a relatively lower packing density enhances fluid convection especially in the downward direction driven by gravity due to higher porosity [16]. Such strong downward fluid convection can further increase the instability of the molten pool, resulting in formation of balling defect.

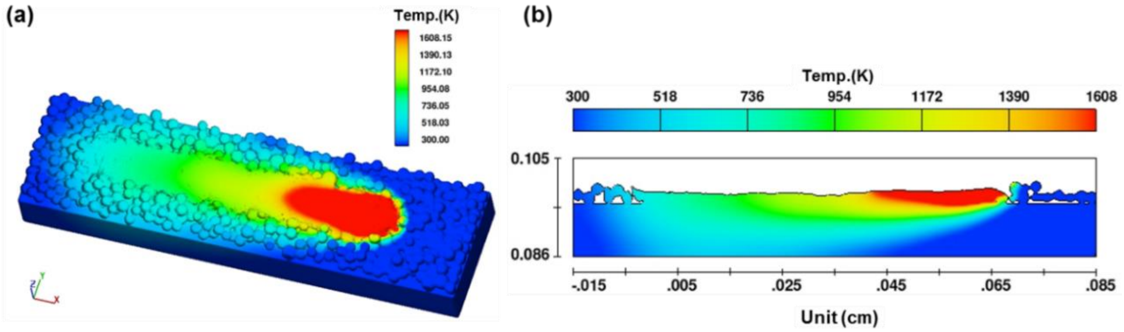

Figure 7.10 (a) 3D view and (b) 2D longitudinal section view of molten pool for the high powder packing density of 45%. All other conditions, i.e., laser power = 150 W, scanning speed = 1.1 m/s, and PSD+, are the same as those in Figure 7.9.

7.4 Summary and conclusion

In summary, the 3D transient simulation of heat transfer and fluid flow in L-PBF is conducted to provide a quantitative understanding of the effect of key processing parameters on bead geometry and formation of balling defect. The 3D model solves the continuum conservation equations at the meso-scale level with a mesh size of 3 μm to accurately resolve individual powder particles. The initial powder stack-up is calculated using a DEM based model and inputted into the 3D model. Through the numerical investigation of a variety of processing variables, the following conclusions can be drawn:

- A positively skewed particle size distribution containing a high fraction of smaller particles results in a smoother contour of the melt pool than the negatively skewed one containing a high fraction of larger particles.
- The formation of balling defect initiates from a void at the center of the molten pool. As the void expands, the molten pool breaks apart into separate islands.
- A faster travel speed and lower laser power can increase the likeliness of forming the balling defect.
- In addition to Rayleigh instability designated by the length to width ratio of the molten pool, the powder particle arrangement (i.e., the powder packing density) has a significant effect on the formation of balling defect. A higher packing density is found to reduce the likeliness of forming such defect.

Although only a simple linear track is simulated, the present model shows the importance of powder level simulation in studying the meso-scale phenomena including molten pool surface profile and formation of baling defect, which are important attributes of the final build quality.

7.5 Acknowledgements

The authors would like to acknowledge the grant from Office of Naval Research (ONR), Award No. N00014-14-1-0688, in support of the research.

7.6 References

1. Korner C, Bauereiss A, Attar E (2013) Fundamental consolidation mechanisms during selective beam melting of powders. Modelling and Simulation in Materials Science and Engineering 21(8):085011.

2. Klassen A, Bauereiss A, Korner C (2014) Modelling of electron beam absorption in complex geometries. Journal of Physics D: Applied Physics 47(6):065307.

3. King W, Anderson AT, Ferencz RM, Hodge NE, Kamath C, Khairallah SA (2015) Overview of modelling and simulation of metal powder bed fusion process at lawrence livermore national laboratory. Materials Science and Technology 31(8):957-968.

4. Matsumoto M, Shiomi M, Osakada K, Abe F (2002) Finite element analysis of single layer forming on metallic powder bed in rapid prototyping by selective laser processing. International Journal of Machine Tools and Manufacture 42(1):61-67.

5. Korner C, Attar E, Heinl P (2011) Mesoscopic simulation of selective beam melting processes. Journal of Materials Processing Technology 211(6):978-987.

6. Khairallah SA, Anderson A (2014) Mesoscopic simulation model of selective laser melting of stainless steel powder. Journal of Materials Processing Technology 214(11):2627-2636.

7. Gurtler FJ, Karg M, Leitz KH, Schmidt M (2013) Simulation of laser beam melting of steel powders using the three-dimensional volume of fluid method. Physics Procedia 41:874-879.

8. Šmilauer V, Catalano E, Chareyre B, Dorofeenko S, Duriez J, Gladky A, Kozicki J, Modenese C, Scholtès L, Sibille L, Stránský J, and Thoeni K (2010) Yade documentation (šmilauer v, ed.), The Yade project, 1st ed., http://yade-dem.Org/doc/

9. Flow3d: Version 11.0.1.2 (2014): User manual, Flowscience, Santa Fe, NM, USA.

10. Cho MH, Lim YC, Farson DF (2006) Simulation of weld pool dynamics in the stationary pulsed gas metal arc welding process and final weld shape. Welding Journal 85(12):271S-283S.

11. Boley CD, Khairallah SA, Rubenchik AM (2015) Calculation of laser absorption by metal powders in additive manufacturing. Applied Optics 54(9):2477-2482.

12. Spierings A, Levy G (2009) Comparison of density of stainless steel 316L parts produced with selective laser melting using different powder grades. In Proceedings of Solid Freeform Fabrication Symposium. University of Texas at Austin, Austin, pp 342-353

13. Liu B, Wildman R, Tuck C, Ashcroft I, Hague R (2011) Investigation the effect of particle size distribution on processing parameters optimisation in selective laser melting process. In Proceedings of Solid Freeform Fabrication Symposium, University of Texas at Austin, Austin. pp 227-238

14. Kruth JP, Levy G, Klocke F, Childs THC (2007) Consolidation phenomena in laser and powder-bed based layered manufacturing. CIRP Annals - Manufacturing Technology 56(2):730-759.

15. Spierings A, Herres N, Levy G (2011) Influence of the particle size distribution on surface quality and mechanical properties in am steel parts. Rapid Prototyping Journal 17(3):195-202.

16. Attar E (2011) Simulation of selective electron beam melting processes. PhD thesis, University of Erlangen-Nuremberg, Erlangen, Germany

Chapter 8: Conclusion and future work

The numerical simulations of laser and metal powder based additive manufacturing were conducted in both powder injection and powder bed systems. On the basis of the results in this dissertation, the following conclusions are made.

In chapter 2, 3D transport simulation of AM was used to understand the effect of convection flow on melt pool formation and solidification conditions in IN718 deposits. The most deeply penetrated region was formed toward the back of the weld pool, behind the laser focus spot but ahead of the rear solidification boundary. The increased penetration occurs in this region of the melt pool by impingement of opposing fluid flows caused by transition of surface tension gradient from positive to negative. Also, temperature gradient G was calculated along the weld pool centerline and, in combination with solidification rate R at the back edge of the weld pool, was used to predict the solidification morphology of columnar dendrites.

In chapter 3, the numerical and theoretical calculations were used to provide insight into the effect of weld pool convection and shape on the predicted size of PDAS. The G and R along the solidification fusion boundary were obtained from a transport simulation of IN718 deposit. The results showed that R near to the weld centerline was approximately equal to the beam travel speed at locations near the top weld pool surface.

However, relatively sharp decreases of R were observed near the bottom of the weld pool due to a larger angle between the boundary normal and the weld travel vector. Furthermore, the obtained G and R were used to investigate the relationships between PDAS and solidification conditions (G and R) using theoretical models of Kurz-Fisher and Trivedi. The result showed that mixing of the two opposing flows in an intermediate region produced a solidification boundary cooling rate that decreased from top to bottom and from the rear center to the outermost lateral edge of the weld pool, inverse to the variation of predicted dendrite arm spacing. From the results, it can be concluded that the convective mixing in the weld pool alters solidification conditions so as to retarded cooling. Correspondingly, PDAS also increases near the weld edge. It noted that the PDAS values predicted by Trivedi model are closer to the measured values of 9.9 µm.

In chapter 4, 3D transport simulation was extended to the multiple layer, single track LAM process. The analysis of melt pool bottom shape showed that convex melt pool bottom shape is partly due to the fact that the top surface of the prior layer upon which the melt is being deposited is convex. The investigation of the dimensionless numbers (Pe, *Pr* and Ma) and fluid flow patterns showed that the hemispherical melt pool free surface in LAM causes the mechanisms that determine melt pool fusion boundary shape to be different from melt pools formed on a flat surface. Also, it showed that the Marangoni driven fluid penetration into the solid substrate at the outward edges becomes deeper and consequently the more pronounced convex shape is promoted at the pool bottom.

In chapter 5, three distinct melt pool fluid flow patterns driven by three different types of thermocapillary gradients (positive, negative and mixed) were investigated to show their effect on final build geometry during LAM. The results showed that a similar mushroom shape bulge was produced at the lateral edge of the start of deposits made with material having positive and negative gradients in spite of significantly different fluid flow patterns that form the bulge. The fluid flow pattern analysis suggests that the particular colliding of opposing flows driven by material having mixed gradient can be used to minimize the deposit bulging. The results also showed that the bulge at the start of the build was reduced by a melt pool having a mixed thermocapillary gradient. The lateral width of the bulge was approximately 56% less than that of the bulge width of a deposit having the negative gradient. Thus, it can be concluded that non-uniformity and surface finish of the deposit sidewall can be optimized by manipulation of the thermocapillary gradient.

In chapter 6, the advanced DEM simulation was utilized to examine the effect of powder particle distribution and size on the particle packing density in laser powder bed fusion (L-PBF) process. The results showed that equal size and Gaussian size distribution have little effect on particle packing density increase. However, asymmetric distribution with negatively skewed, positively skewed and Gaussian like distribution contribute to increase the packing density. The highest density is obtained in positively skewed distribution as opposed to negatively skewed distribution. The role of fine particles was examined with quantitative method using the ratio of D_{90}/D_{10}. The density is the highest with the maximum ratio of D_{90}/D_{10}. From those result, it revealed that the higher fraction of fine particles is a key factor for increasing the packing density. Therefore, it concluded that fine and asymmetric particle size distribution is recommended to obtain higher packing density.

In chapter 7, 3D transient simulation of heat transfer and fluid flow was conducted for L-PBF to provide a quantitative understanding of the effect of particle size distribution and key processing parameters on bead geometry and formation of balling effect. The results showed that the positively skewed particle distribution containing a higher fraction of smaller particles produced smoother contour of the melt pool. The simulation results also showed that a faster scanning speed and lower laser power increased likeness of forming the balling effect. The simulation noticed that Rayleigh instability not only has a significant effect on the formation of balling effect but also the higher packing density has a considerable effect on reducing the likeness of ball forming.

Future work will be directed at refining the powder injection simulation to include variation of powder catchment efficiency and laser beam Fresnel reflection with melt pool shape and size. Also, the future work is planned to refine powder bed simulation to include recoil force, evaporation cooling and laser beam absorption for multiple layers of particles. Then the simulation is extended to multiple layer and multiple track deposits for more general insight into L-PBF solidification microstructure. Experimental effort will be made to validate current L-PBF simulation in chapter 7. For the simulation in both systems, it is anticipated that detailed physical insights provided by integrated process, materials and solid mechanics simulations will eventually facilitate spatial programming of process parameters used during building of 3D LAM parts to attenuate or accentuate localized microstructure and property variations that can be controlled by melt pool shape and associated solidification structure.

Bibliography

Chapter 1

1. Zhou JH, Zhang YW, Chen JK (2009) Numerical simulation of random packing of spherical particles for powder-based additive manufacturing. Journal of Manufacturing Science and Engineering: ASME 131(3):031004.

2. Harris ID, Director A (2011) Development and implementation of metals additive manufacturing. In DOT International, New Orleans.

3. Frazier WE (2014) Metal additive manufacturing: A review. Journal of Materials Engineering and Performance 23(6):1917-1928.

4. Weisheit A, Gasser A, Backes G, Jambor T, Pirch N, Wissenbach K (2013) Direct laser cladding , current status and future scope of application. In: Majumdar JD, Manna I (eds) Laser-assisted fabrication of materials, vol 161. Springer series in materials science. Springer Berlin Heidelberg, pp 221-240

5. Wong KV, Hernandez A (2012) A review of additive manufacturing. ISRN Mechanical Engineering 2012:208760.

6. Mazumder J, Schifferer A, Choi J (1999) Direct materials deposition: Designed macro and microstructure. Materials Research Innovations 3(3):118-131.

Chapter 2

1. Zhong M, Liu W (2010) Laser surface cladding: The state of the art and challenges. Journal of Mechanical Engineering Science 224(C5):1041-1060.

2. A.Weisheit, Gasser A, Backes G, Jambor T, Pirch N, Wissenbach K (2013) Laser-assisted fabrication of materials - direct laser cladding , current status and future scope of application, vol 161. Springer New York

3. Hoadley AFA, Rappaz M (1992) A thermal model of laser cladding by powder injection. Metallurgical Transactions B 23(5):631-642.

4. Picasso M, Rappaz M (1994) Laser-powder-material interactions in the laser cladding process Journal De Physique IV 4(C4):27-33.

5. Toyserkani E, Khajepour A, Corbin S (2004) 3-d finite element modeling of laser cladding by powder injection: Effects of laser pulse shaping on the process. Optics and lasers in engineering 41(6):849-867.

6. Choi J, Han L, Hua Y (2005) Modeling and experiments of laser cladding with droplet injection. Journal of Heat Transfer 127(9):978-986.

7. Wen S, Shin YC (2010) Modeling of transport phenomena during the coaxial laser direct deposition process. Journal of Applied Physics 108(4):044908

8. Sahoo P, Debroy T, Mcnallan MJ (1988) Surface tension of binary metal-surface active solute systems under conditions relevant to welding metallurgy. Metallurgical Transactions B 19B(3):483-491.

9. Lee PD, Quested PN, McLean M (1998) Modelling of marangoni effects in electron beam melting. Philosophical Transactions of the Royal Society of London 356(1739):1027-1043.

10. Su Y, Mills KC (2005) A model to calculate surface tension of commercial alloys. Journal of Materials Science 40(9-10):2185-2190.

11. Zhao CX, Kwakernaak C, Pan Y, Richardson IM, Saldi Z, Kenjeres S, Kleijn CR (2010) The effect of oxygen on transitional marangoni flow in laser spot welding. Acta Materialia 58(19):6345-6357.

12. Cho MH, Lim YC, Farson DF (2006) Simulation of weld pool dynamics in the stationary pulsed gas metal arc welding process and final weld shape. Welding Journal 85(12):271-s to 283-s.

13. Cho JH, Farson DF, Milewski JO, Hollis KJ (2009) Weld pool flows during initial stages of keyhole formation in laser welding. Journal of Physics D: Applied Physics 42(17):175502.

14. Mills KC (2002) Recommended values of thermophysical properties for selected commercial alloys. Woodhead, Cambridge, England

15. Pottlacher G, Hosaeus H, Kaschnitz E, Seifter A (2002) Thermophysical properties of solid and liquid inconel 718 alloy. Scandinavian Journal of Metallurgy 31(3):161-168.

16. Lewandowski MS, Overfelt RA (1999) High temperature deformation behavior of solid and semi-solid alloy 718. Acta Materialia 47(18):4695-4710.

17. Gedda H, Powell J, Wahlstrom G, Li WB, Engstrom H, Magnusson C (2002) Energy redistribution during co_2 laser cladding. Journal of Laser Applications 14(2):78-82.

18. Xie J, Kart A, Rothenflue JA, Latham WP (1997) Temperature-dependent absorptivity and cutting capability of CO_2 , Nd:YAG and chemical oxygen-iodine lasers. Journal of Laser Applications 9 (2):77-85.

19. Shelton JA, Shin YC (2010) Comparative evaluation of laser-assisted micro-milling for aisi 316, aisi 422, Ti-6Al-4V and inconel 718 in a side-cutting configuration. Journal of Micromechanics and Microengineering 20(7):075012.

20. Kim KR, Farson DF (2001) CO_2 laser-plume interaction in materials processing. Journal of Applied Physics 89(1):681-688.

21. Picasso M, Marsden CF, Wagniere JD, Frenk A, Rappaz M (1994) A simple but realistic model for laser cladding. Metallurgical and Materials Transactions B 25B(2):281-291.

22. Kou S (2012) Fluid flow and solidification in welding: Three decades of fundamental research at the university of wisconsin. Welding Journal 91(11):287S-302S.

23. Zacharia T, David SA, Vitek JM, Debroy T (1989) Weld pool development during gta and laser beam welding of type 304 stainless steel--part I: Theoretical analysis. Welding Journal 68(12):499-s to 509-s.

24. Mcnallan MJ, Debroy T (1991) Effect of temperature and composition on surface tension in fe-ni-cr alloys containing sulfur. Metallurgical Transactions B 22B(4):557-560.

25. Anderson TD, DuPont JN, DebRoy T (2010) Origin of stray grain formation in single-crystal superalloy weld pools from heat transfer and fluid flow modeling. Acta Materialia 58(4):1441-1454.

26. Kou S (2003) Welding metallurgy. 2nd edn. John Wiley & Sons, New Jersey

27. Weisheit A, Backes G, Stromeyer R, Gasser A, Wissenbach K, Poprawe R Powder injection: The key to reconditioning and generating components using laser cladding. In Proceedings of International Congress on Advanced Materials and Processes, Materials Week 2001, Munich, Germany. pp pp. 1-7

28. Lim YC, Yu X, Cho JH, Sosa J, Farson DF, Babu SS, McCracken S, Flesner B (2010) Effect of magnetic stirring on grain structure refinement--part i: Autogenous nickel alloy welds. Science and Technology of Welding and Joining 15(7):583-589.

29. Zhao YZ, Lei YP, Shi YW (2005) Effects of surface-active elements sulfur on flow patterns of welding pool. Journal of Materials Science & Technology 21(03):408-414.

Chapter 3

1. Gregory OJ, Amani M, Tougas IM, Drehman AJ (2012) Stability and microstructure of indium tin oxynitride thin films. Journal of the American Ceramic Society 95(2):705-710.

2. Borel MO, Nicoll AR, Schlapfer HW, Schmid RK (1989) The wear mechanisms occurring in abradable seals of gas turbines. Surface and Coatings Technology 39–40(0):117-126.

3. Anderson TD, DuPont JN, DebRoy T (2010) Stray grain formation in welds of single-crystal ni-base superalloy cmsx-4. Metallurgical and Materials Transactions A 41(1):181-193.

4. Zhong M, Liu W (2010) Laser surface cladding: The state of the art and challenges. Journal of Mechanical Engineering Science 224(C5):1041-1060.

5. Majumdar JD, Manna I (2013) Laser-assisted fabrication of materials, vol 161. Direct laser cladding , current status and future scope of application. Springer, New York

6. Lee YS, Nordin M, Babu SS, Farson DF (2014) Influence of fluid convection on weld pool formation in laser cladding. Welding Journal 93(8):292S-300S.

7. DuPont J, Babu S, Liu S (2013) Welding of materials for energy applications. Metallurgical and Materials Transactions A 44(7):3385-3410.

8. Heiple CR, Roper JR (1982) Mechanism for minor element effect on gta fusion zone geometry. Welding Journal 61(4):S97-S102.

9. Heiple CR, Roper JR, Stagner RT, Aden RJ (1983) Surface-active element effects on the shape of gta, laser, and electron-beam welds. Welding Journal 62(3):S72-S77.

10. Chan C, Mazumder J, Chen MM (1983) A two-dimensional transient model for convection in laser melted pool. Journal of Metals 35(12):49.

11. Kou S, Wang YH (1986) Three-dimensional convection in laser melted pools. Metallurgical and Materials Transactions A 17(12):2265-2270.

12. Kou S (2012) Fluid flow and solidification in welding: Three decades of fundamental research at the university of wisconsin. Welding Journal 91(11):287S-302S.

13. Mills KC, Keene BJ, Brooks RF, Shirali A (1998) Marangoni effects in welding. Philosophical Transactions of the Royal Society, A:911-926.

14. Sahoo P, Debroy T, Mcnallan MJ (1988) Surface tension of binary metal-surface active solute systems under conditions relevant to welding metallurgy. Metallurgical and Materials Transactions B 19B(3):483-491.

15. Lee PD, Quested PN, McLean M (1998) Modelling of marangoni effects in electron beam melting. Philosophical transactions of the Royal Society 356(1739):1027-1043.

16. Su Y, Mills KC (2005) A model to calculate surface tension of commercial alloys. Journal of Materials Science 40(9-10):2185-2190.

17. Zhao Y, Shi Y, Lei Y (2006) The study of surface-active element oxygen on flow patterns and penetration in a-tig welding. Metallurgical and Materials Transactions B 37(3):485-493.

18. Zhao CX, Kwakernaak C, Pan Y, Richardson IM, Saldi Z, Kenjeres S, Kleijn CR (2010) The effect of oxygen on transitional marangoni flow in laser spot welding. Acta Materialia 58(19):6345-6357.

19. David SA, Babu SS, Vitek JM (2003) Welding: Solidification and microstructure. JOM 55(6):14-20.

20. Kou S (2003) Welding metallurgy. 2nd edn. John Wiley & Sons, New Jersey

21. DebRoy T, David SA (1995) Physical processes in fusion welding. Reviews of Modern Physics 67(1):85-112.

22. Hunt JD (1984) Steady state columnar and equiaxed growth of dendrites and eutectic. Materials Science and Engineering 65(1):75-83.

23. Anderson TD, DuPont JN, DebRoy T (2010) Origin of stray grain formation in single-crystal superalloy weld pools from heat transfer and fluid flow modeling. Acta Materialia 58(4):1441-1454.

24. Gaumann M, Bezencon C, Canalis P, Kurz W (2001) Single-crystal laser deposition of superalloys: Processing-microstructure maps. Acta Materialia 49(6):1051-1062.

25. Gao Z, Ojo OA (2012) Modeling analysis of hybrid laser-arc welding of single-crystal nickel-base superalloys. Acta Materialia 60(6–7):3153-3167.

26. Picasso M, Marsden CF, Wagniere JD, Frenk A, Rappaz M (1994) A simple but realistic model for laser cladding. Metallurgical and Materials Transactions B 25(2):281-291.

27. J. Xie, A. Kart, Rothenflue JA, Latham WP (1997) Temperature-dependent absorptivity and cutting capability of CO_2 , Nd:YAG and chemical oxygen iodine lasers. Journal of Laser Applications 9:77-85.

28. David S, Vitek J (1989) Correlation between solidification parameters and weld microstructures. International Materials Reviews 34(1):213-245.

29. Rappaz M, David SA, Vitek JM, Boatner LA (1989) Development of microstructures in Fe-15Ni-15Cr single crystal electron beam welds. Metallurgical and Materials Transactions A 20(6):1125-1138.

30. Vitek JM (2005) The effect of welding conditions on stray grain formation in single crystal welds - theoretical analysis. Acta Materialia 53(1):53-67.

31. Kurz W, Fisher DJ (1981) Dendrite growth at the limit of stability: Tip radius and spacing. Acta Metallurgica 29(1):11-20.

32. Trivedi R (1984) Interdendritic spacing: Part ii. A comparison of theory and experiment. Metallurgical and Materials Transactions A 15(6):977-982.

33. Spinellia JE, Rochab OFL, Garciaa A (2006) The influence of melt convection on dendritic spacing of downward unsteady-state directionally solidified Sn-Pb alloys. Materials Research Bulletin 9(1):51-57.

34. Gao S, Liu L, Xu Y, Yang C, Zhang J, Fu H (2012) Influences of processing parameters on microstructure during investment casting of nickel-base single crystal superalloy DD3. China Foundry 9(2):159-164.

35. Lewandowski MS, Overfelt RA (1999) High temperature deformation behavior of solid and semi-solid alloy 718. Acta Materialia 47(18):4695-4710.

36. Wang W, Lee PD, McLean M (2003) A model of solidification microstructures in nickel-based superalloys: Predicting primary dendrite spacing selection. Acta Materialia 51(10):2971-2987.

37. Overfelt RA, Taylor RE (1996) Thermophysical property measurements for casting process simulation. Thermal Conduct 23:538-552.

38. Kovacevic R (2012) Welding processes. InTech, Rijeka, Croatia

39. Zacharia T, David SA, Vitek JM, Debroy T (1989) Weld pool development during gta and laser beam welding of type 304 stainless steel, part I. Welding Journal 68:S499-S509.

Chapter 4

1. Frazier WE (2014) Metal additive manufacturing: A review. J Mater Eng Perform 23(6):1917-1928.

2. Raghavan A, Wei HL, Palmer TA, DebRoy T (2013) Heat transfer and fluid flow in additive manufacturing. J Laser Appl 25(5):052006.

3. Cho MH, Farson DF, Lim YC, Choi HW (2007) Hybrid laser/arc welding process for controlling bead profile. Sci Technol Weld Join 12(8):677-688.

4. Hu J, Tsai HL (2008) Modelling of transport phenomena in 3d gmaw of thick metals with v groove. J Phys D-Appl Phys 41(6):065202.

5. Cho J, Farson DF, Hollis KJ, Milewski JO (2015) Numerical analysis of weld pool oscillation in laser welding. J Mech Sci Technol 29(4):1715-1722.

6. Manvatkar V, De A, DebRoy T (2014) Heat transfer and material flow during laser assisted multi-layer additive manufacturing. J Appl Phys 116(12):124905.

7. Kumar A, Paul CP, Padiyar AS, Bhargava P, Mundra G, Kukreja LM (2014) Numerical simulation of laser rapid manufacturing of multi-layer thin wall using an improved mass addition approach. Numer Heat Tranf A-Appl 65(9):885-910.

8. Duitsch U, Schreck S, Rohde M (2003) Experimental and numerical investigations of heat and mass transport in laser-induced modification of ceramic surfaces. Int J Thermophys 24(3):731-740.

9. Alimardani M, Toyserkani E, Huissoon JP (2007) Three-dimensional numerical approach for geometrical prediction of multilayer laser solid freeform fabrication process. J Laser Appl 19(1):14-25.

10. Wen S, Shin YC (2010) Modeling of transport phenomena during the coaxial laser direct deposition process. J Appl Phys 108(4):044908

11. Liu ZY, Qi H (2014) Numerical simulation of transport phenomena for a double-layer laser powder deposition of single-crystal superalloy. Metall Mater Trans A 45A(4):1903-1915.

12. Morville S, Carin M, Peyre P, Gharbi M, Carron D, Le Masson P, Fabbro R (2012) 2d longitudinal modeling of heat transfer and fluid flow during multilayered direct laser metal deposition process. J Laser Appl 24(3):9.

13. Kong F, Kovacevic R (2010) Modeling of heat transfer and fluid flow in the laser multilayered cladding process. Metall Mater Trans B 41(6):1310-1320.

14. Manvatkar V, De A, DebRoy T (2015) Spatial variation of melt pool geometry, peak temperature and solidification parameters during laser assisted additive manufacturing process. Mater Sci Technol 31(8):924-930.

15. Lee Y, Nordin M, Babu SS, Farson DF (2014) Effect of fluid convection on dendrite arm spacing in laser deposition. Metall Mater Trans B 45(4):1520-1529.

16. Limmaneevichitr C, Kou S (2000) Experiments to simulate effect of marangoni convection on weld pool shape. Weld J 79(8):231s-237s.

17. Arora A, Roy GG, DebRoy T (2009) Unusual wavy weld pool boundary from dimensional analysis. Scr Mater 60(2):68-71.

18. Wei PS, Yeh JS, Ting CN, DebRoy T, Chung FK, Lin CL (2009) The effects of prandtl number on wavy weld boundary. Int J Heat Mass Transf 52(15-16):3790-3798.

19. Lee YS, Nordin M, Babu SS, Farson DF (2014) Influence of fluid convection on weld pool formation in laser cladding. Weld J 93(8):292S-300S.

20. Carcel B, Sampedro J, Perez I, Fernandez E, Ramos JA Improved laser metal deposition (lmd) of nickel base superalloys by pyrometry process control. In *Proceedings of 18th International Symposium on Gas Flow & Chemical Lasers & High Power Lasers*, Sofia, Bulgaria. International Society for Optics and Photonics, p 775123

21. Pottlacher G, Hosaeus H, Kaschnitz E, Seifter A (2002) Thermophysical properties of solid and liquid inconel 718 alloy. Scand J Metall 31(3):161-168.

22. Mills KC (2002) Recommended values of thermophysical properties for selected commercial alloys. Woodhead, Cambridge

23. Unocic RR, DuPont JN (2004) Process efficiency measurements in the laser engineered net shaping process. Metall Mater Trans B 35(1):143-152.

24. Xie J, Kar A, Rothenflue JA, Latham WP (1997) Temperature-dependent absorptivity and cutting capability of co2, nd:Yag and chemical oxygen-iodine lasers. J Laser Appl 9(2):77-85.

25. Shelton JA, Shin YC (2010) Comparative evaluation of laser-assisted micro-milling for aisi 316, aisi 422, ti-6al-4v and inconel 718 in a side-cutting configuration. J Micromech Microeng 20(7):12.

26. Picasso M, Marsden CF, Wagniere JD, Frenk A, Rappaz M (1994) A simple but realistic model for laser cladding. Metall Mater Trans B 25(2):281-291.

27. Kelly SM (2004) Thermal and microstructure modeling of metal deposition processes with application to ti-6al-4v. PhD Dissertation, Pennsylvania State University, University Park, PA

28. Vasinonta A, Beuth J, Griffith M Process maps for laser deposition of thin-walled structures. In *Proceedings of Solid Freeform Fabrication*, Austin, Solid Freeform Fabrication Proceedings (Series). University of Texas at Austin, pp 383-391

29. Pinkerton AJ, Li L (2004) Modelling the geometry of a moving laser melt pool and deposition track via energy and mass balances. J Phys D-Appl Phys 37(14):1885-1895.

30. Gharbi M, Peyre P, Gorny C, Carin M, Morville S, Le Masson P, Carron D, Fabbro R (2013) Influence of various process conditions on surface finishes induced by the direct metal deposition laser technique on a ti-6al-4v alloy. J Mater Process Technol 213(5):791-800.

Chapter 5

1. Zhou JH, Zhang YW, Chen JK (2009) Numerical simulation of random packing of spherical particles for powder-based additive manufacturing. Journal of Manufacturing Science and Engineering: ASME 131(3):031004.

2. Mazumder J, Schifferer A, Choi J (1999) Direct materials deposition: Designed macro and microstructure. Materials Research Innovations 3(3):118-131.

3. Gharbi M, Peyre P, Gorny C, Carin M, Morville S, Le Masson P, Carron D, Fabbro R (2013) Influence of various process conditions on surface finishes induced by the direct metal deposition laser technique on a Ti-6Al-4V alloy. Journal of Materials Processing Technology 213(5):791-800.

4. Lee YS, Nordin M, Babu SS, Farson DF (2014) Influence of fluid convection on weld pool formation in laser cladding. Welding Journal 93(8):292S-300S.

5. Gedda H, Powell J, Wahlstrom G, Li WB, Engstrom H, Magnusson C (2002) Energy redistribution during co_2 laser cladding. Journal of Laser Applications 14(2):78-82.

6. Tabernero I, Lamikiz A, Ukar E, Martinez S, Celaya A (2014) Modeling of the geometry built-up by coaxial laser material deposition process. International Journal of Advanced Manufacturing Technology 70(5-8):843-851.

7. Wen SY, Shin YC (2010) Modeling of transport phenomena during the coaxial laser direct deposition process. Journal of Applied Physics 108(4):044908.

8. Vasquez F, Ramos-Grez JA, Walczak M (2012) Multiphysics simulation of laser-material interaction during laser powder depositon. International Journal of Advanced Manufacturing Technology 59(9-12):1037-1045.

9. Choi J, Han L, Hua Y (2005) Modeling and experiments of laser cladding with droplet injection. Journal of Heat Transfer: ASME 127(9):978-986.

10. Toyserkani E, Khajepour A, Corbin S (2004) 3-d finite element modeling of laser cladding by powder injection: Effects of laser pulse shaping on the process. Optics and Lasers in Engineering 41(6):849-867.

11. Picasso M, Rappaz M (1994) Laser-powder-material interactions in the laser cladding process. Journal de Physique IV 4(C4):27-33.

12. Manvatkar V, De A, DebRoy T (2014) Heat transfer and material flow during laser assisted multi-layer additive manufacturing. Journal of Applied Physics 116(12):124905.

13. Kumar A, Paul CP, Padiyar AS, Bhargava P, Mundra G, Kukreja LM (2014) Numerical simulation of laser rapid manufacturing of multi-layer thin wall using an improved mass addition approach. Numerical Heat Transfer Part A: Applications 65(9):885-910.

14. Alimardani M, Toyserkani E, Huissoon JP (2007) Three-dimensional numerical approach for geometrical prediction of multilayer laser solid freeform fabrication process. Journal of Laser Applications 19(1):14-25.

15. Liu ZY, Qi H (2014) Numerical simulation of transport phenomena for a double-layer laser powder deposition of single-crystal superalloy. Metallurgical and Materials Transactions A 45A(4):1903-1915.

16. Kong FR, Kovacevic R (2010) Modeling of heat transfer and fluid flow in the laser multilayered cladding process. Metallurgical and Materials Transactions B 41(6):1310-1320.

17. Pinkerton AJ (2010) Laser direct metal deposition: Theory and applications in manufacturing and maintenance. In: Advances in laser materials processing: Technology, research and applications. Woodhead Publishing Ltd., Cambridge, England, pp 461-491

18. Lee PD, Quested PN, McLean M (1998) Modelling of marangoni effects in electron beam melting. Philosophical Transactions of the Royal Society A 356(1739):1027-1043.

19. Xie J, Kar A, Rothenflue JA, Latham WP (1997) Temperature-dependent absorptivity and cutting capability of CO_2, Nd:YAG and chemical oxygen-iodine lasers. Journal of Laser Applicatoins 9(2):77-85.

20. Weisheit A, Backes G, Stromeyer R, Gasser A, Wissenbach K, Poprawe R (2001) Powder injection: The key to reconditioning and generating components using laser

cladding. In: Proceedings of the international congress on advanced materials and processes, materials week 2001. Munich, Germany, pp 1-8

21. Mills KC (2002) Recommended values of thermophysical properties for selected commercial alloys. Woodhead Publishing Ltd., Cambridge, England

22. McNallan MJ, Debroy T (1991) Effect of temperature and composition on surface tension in Fe-Ni-Cr alloys containing sulfur. Metallurgical and Materials Transactions B 22(4):557-560.

23. Zacharia T, David SA, Vitek JM, Debroy T (1989) Weld pool development during gta and laser beam welding of type 304 stainless steel: Part 1-theoretical analysis. Welding Journal 68:499S-509S.

24. Carcel B, Sampedro J, Perez I, Fernandez E, Ramos JA (2010) Improved laser metal deposition (lmd) of nickel base superalloys by pyrometry process control. In: Proceedings of spie-the international society for optical engineering. Sofia, Bulgaria, p 775123

25. Pottlacher G, Hosaeus H, Kaschnitz E, Seifter A (2002) Thermophysical properties of solid and liquid inconel 718 alloy. Scandinavian Journal of Metallurgy 31(3):161-168.

26. Su WN, Erasenthiran P, Dickens PM (2003) Investigation of fully dense laser sintering of tool steel powder using a pulsed Nd : YAG (neodymium-doped yttrium aluminium garnet) laser. Proceedings of the Institution of Mechanical Engineers, Part C: Journal of Mechanical Engineering Science 217(1):127-138.

27. Cho MH, Farson DF (2007) Simulation study of a hybrid process for the prevention of weld bead hump formation. Welding Journal 86(9):253S-262S.

28. Morgan R, Sutcliffe CJ, O'Neill W (2001) Experimental investigation of nanosecond pulsed Nd : YAG laser re-melted pre-placed powder beds. Rapid Prototyping Journal 7(3):159-172.

29. Paul CP, Mishra SK, Kumar A, Kukreja LM (2013) Laser rapid manufacturing on vertical surfaces: Analytical and experimental studies. Surface and Coatings Technolog 224:18-28.

Chapter 6

1. Zhou JH, Zhang YW, Chen JK (2009) Numerical simulation of random packing of spherical particles for powder-based additive manufacturing. Journal of Manufacturing Science and Engineering 131(3):031004.

2. Sugavaneswaran M, Arumaikkannu G (2014) Modelling for randomly oriented multi material additive manufacturing component and its fabrication. Materials & Design 54(0):779-785.

3. Körner C, Attar E, Heinl P (2011) Mesoscopic simulation of selective beam melting processes. Journal of Materials Processing Technology 211(6):978-987.

4. Liu B, Wildman R, Tuck C, Ashcroft I, Hague R (2011) Investigation the effect of particle size distribution on processing parameters optimisation in selective laser melting process. In Proceedings of Solid Freeform Fabrication Symposium, Austin:227-238.

5. Li Y, Gu D (2014) Parametric analysis of thermal behavior during selective laser melting additive manufacturing of aluminum alloy powder. Materials & Design 63:856-867.

6. He D, Ekere NN, Cai L (1999) Computer simulation of random packing of unequal particles. Physical Review E 60(6):7098-7104.

7. Yang RY, Zou RP, Yu AB (2000) Computer simulation of the packing of fine particles. Physical Review E 62(3):3900-3908.

8. Shi Y, Zhang YW (2008) Simulation of random packing of spherical particles with different size distributions. Applied Physics A: Materials Science & Processing 92(3):621-626.

9. Jia T, Zhang YW, Chen JK (2011) Dynamic simulation of particle packing with different size distributions. Journal of Manufacturing Science and Engineering 133(2):4.
10. Jia T, Zhang YW, Chen JK (2012) Simulation of granular packing of particles with different size distributions. Computational Materials Science 51(1):172-180.

11. Dou X, Mao YJ, Zhang YW (2014) Effects of contact force model and size distribution on microsized granular packing. Journal of Manufacturing Science and Engineering: ASME 136(2):9.

12. Cheng YF, Guo SJ, Lai HY (2000) Dynamic simulation of random packing of spherical particles. Powder Technology 107(1-2):123-130.

13. Schmid M, Amado A, Wegener K (2014) Materials perspective of polymers for additive manufacturing with selective laser sintering. Journal of Materials Research 29:1824-1832.

14. Uskoković D, Exner HE (1990) The kinetics of contact formation during sintering by diffusion mechanisms. In: Sōmiya S, Moriyoshi Y (eds) Sintering key papers. Springer Netherlands, pp 111-146. doi:10.1007/978-94-009-0741-6_8

15. Karapatis NP, Egger G, Gygax PE, Glardon R (1999) Optimization of powder layer density in selective laser sintering. In Proceedings of Solid Freeform Fabrication Symposium, Austin:255-263.

16. Chareyre B, Villard P (2005) Dynamic spar elements and discrete element methods in two dimensions for the modeling of soil-inclusion problems. Journal of Engineering Mechanics 131(7):689-698.

17. Cundall PA, Strack OD (1979) A discrete numerical model for granular assemblies. Geotechnique 29(1):47-65.

18. Cheng Y, Guo S, Lai H (2000) Dynamic simulation of random packing of spherical particles. Powder Technology 107(1):123-130.

19. Shiu WJ, Donze FV, Daudeville L (2008) Compaction process in concrete during missile impact: A dem analysis. Computers and Concrete 5(4):329-342.

20. O'Sullivan C, Cui L, Bray JD (2004) Three-dimensional discrete element simulations of direct shear tests. In Proceedings of the 2nd International PFC Symposium, Kyoto:373-382.

21. Morgan JK, Boettcher MS (1999) Numerical simulations of granular shear zones using the distinct element method: 1. Shear zone kinematics and the micromechanics of localization. Journal of Geophysical Research: Solid Earth (1978–2012) 104(B2):2703-2719.

22. Spierings A, Levy G (2009) Comparison of density of stainless steel 316l parts produced with selective laser melting using different powder grades. In Proceedings of Solid Freeform Fabrication Symposium, Austin:342-353.

23. Spierings A, Herres N, Levy G (2011) Influence of the particle size distribution on surface quality and mechanical properties in am steel parts. Rapid Prototyping Journal 17(3):195-202.

Chapter 7

1. Korner C, Bauereiss A, Attar E (2013) Fundamental consolidation mechanisms during selective beam melting of powders. Modelling and Simulation in Materials Science and Engineering 21(8):085011.

2. Klassen A, Bauereiss A, Korner C (2014) Modelling of electron beam absorption in complex geometries. Journal of Physics D: Applied Physics 47(6):065307.

3. King W, Anderson AT, Ferencz RM, Hodge NE, Kamath C, Khairallah SA (2015) Overview of modelling and simulation of metal powder bed fusion process at lawrence livermore national laboratory. Materials Science and Technology 31(8):957-968.

4. Matsumoto M, Shiomi M, Osakada K, Abe F (2002) Finite element analysis of single layer forming on metallic powder bed in rapid prototyping by selective laser processing. International Journal of Machine Tools and Manufacture 42(1):61-67.

5. Korner C, Attar E, Heinl P (2011) Mesoscopic simulation of selective beam melting processes. Journal of Materials Processing Technology 211(6):978-987.

6. Khairallah SA, Anderson A (2014) Mesoscopic simulation model of selective laser melting of stainless steel powder. Journal of Materials Processing Technology 214(11):2627-2636.

7. Gurtler FJ, Karg M, Leitz KH, Schmidt M (2013) Simulation of laser beam melting of steel powders using the three-dimensional volume of fluid method. Physics Procedia 41:874-879.

8. Šmilauer V, Catalano E, Chareyre B, Dorofeenko S, Duriez J, Gladky A, Kozicki J, Modenese C, Scholtès L, Sibille L, Stránský J, and Thoeni K (2010) Yade documentation (šmilauer v, ed.), The Yade project, 1st ed., http://yade-dem.Org/doc/

9. Flow3d: Version 11.0.1.2 (2014): User manual, Flowscience, Santa Fe, NM, USA.

10. Cho MH, Lim YC, Farson DF (2006) Simulation of weld pool dynamics in the stationary pulsed gas metal arc welding process and final weld shape. Welding Journal 85(12):271S-283S.

11. Boley CD, Khairallah SA, Rubenchik AM (2015) Calculation of laser absorption by metal powders in additive manufacturing. Applied Optics 54(9):2477-2482.

12. Spierings A, Levy G (2009) Comparison of density of stainless steel 316L parts produced with selective laser melting using different powder grades. In Proceedings of Solid Freeform Fabrication Symposium. University of Texas at Austin, Austin, pp 342-353

13. Liu B, Wildman R, Tuck C, Ashcroft I, Hague R (2011) Investigation the effect of particle size distribution on processing parameters optimisation in selective laser melting process. In Proceedings of Solid Freeform Fabrication Symposium, University of Texas at Austin, Austin. pp 227-238

14. Kruth JP, Levy G, Klocke F, Childs THC (2007) Consolidation phenomena in laser and powder-bed based layered manufacturing. CIRP Annals - Manufacturing Technology 56(2):730-759.

15. Spierings A, Herres N, Levy G (2011) Influence of the particle size distribution on surface quality and mechanical properties in am steel parts. Rapid Prototyping Journal 17(3):195-202.

16. Attar E (2011) Simulation of selective electron beam melting processes. PhD thesis, University of Erlangen-Nuremberg, Erlangen, Germany